



AKARI mid-infrared slitless spectroscopic survey of star-forming galaxies at $z \sim 0.5$

Y. Ohyama, T. Wada, H. Matsuhara, T. Takagi, M. Malkan, T. Goto, E. Egami, H. -M. Lee, M. Im, J. H. Kim, et al.

► To cite this version:

Y. Ohyama, T. Wada, H. Matsuhara, T. Takagi, M. Malkan, et al.. AKARI mid-infrared slitless spectroscopic survey of star-forming galaxies at $z \sim 0.5$. *Astronomy and Astrophysics - A&A*, 2018, 618, 10.1051/0004-6361/201731470 . insu-03666250

HAL Id: insu-03666250

<https://insu.hal.science/insu-03666250>

Submitted on 12 May 2022

HAL is a multi-disciplinary open access archive for the deposit and dissemination of scientific research documents, whether they are published or not. The documents may come from teaching and research institutions in France or abroad, or from public or private research centers.

L'archive ouverte pluridisciplinaire **HAL**, est destinée au dépôt et à la diffusion de documents scientifiques de niveau recherche, publiés ou non, émanant des établissements d'enseignement et de recherche français ou étrangers, des laboratoires publics ou privés.

AKARI mid-infrared slitless spectroscopic survey of star-forming galaxies at $z \lesssim 0.5$

Y. Ohyama¹, T. Wada², H. Matsuhara², T. Takagi^{2,3}, M. Malkan⁴, T. Goto^{5,6}, E. Egami⁷, H.-M. Lee⁸, M. Im⁸, J. H. Kim^{8,9}, C. Pearson^{10,11,12}, H. Inami^{13,14}, S. Oyabu¹⁵, F. Usui^{16,17}, D. Burgarella¹⁸, F. Mazyed¹⁸, M. Imanishi¹⁹, W.-S. Jeong²⁰, T. Miyaji²¹, J. Díaz Tello²¹, T. Nakagawa², S. Serjeant¹¹, T. T. Takeuchi¹⁵, Y. Toba^{1,23}, G. J. White^{10,11}, H. Hanami²², and T. Ishigaki²²

(Affiliations can be found after the references)

Received 29 June 2017 / Accepted 9 August 2018

ABSTRACT

Context. Deep mid-infrared (MIR) surveys have revealed numerous strongly star-forming galaxies at redshift $z \lesssim 2$. Their MIR fluxes are produced by a combination of continuum and polycyclic aromatic hydrocarbon (PAH) emission features. The PAH features can dominate the total MIR flux, but are difficult to measure without spectroscopy.

Aims. We aim to study star-forming galaxies by using a blind spectroscopic survey at MIR wavelengths to understand evolution of their star formation rate (SFR) and specific SFR (SFR per stellar mass) up to $z \approx 0.5$, by paying particular attention to their PAH properties.

Methods. We conducted a low-resolution ($R \approx 50$) slitless spectroscopic survey at 5–13 μm of 9 μm flux-selected sources (>0.3 mJy) around the north ecliptic pole with the infrared camera (IRC) onboard AKARI. After removing 11 AGN candidates by using the IRC photometry, we identify 48 PAH galaxies with PAH 6.2, 7.7, and 8.6 μm features at $z < 0.5$. The rest-frame optical–MIR spectral energy distributions (SEDs) based on CFHT and IRC imaging covering 0.37–18 μm were produced, and analysed in conjunction with the PAH spectroscopy. We defined the PAH enhancement by using the luminosity ratio of the 7.7 μm PAH feature over the 3.5 μm stellar component of the SEDs.

Results. The rest-frame SEDs of all PAH galaxies have a universal shape with stellar and 7.7 μm bumps, except that the PAH enhancement significantly varies as a function of the PAH luminosities. We identify a PAH-enhanced population at $z \gtrsim 0.35$, whose SEDs and luminosities are typical of luminous infrared galaxies. They show particularly larger PAH enhancement at high luminosity, implying that they are vigorous star-forming galaxies with elevated specific SFR. Our composite starburst model that combines a very young and optically very thick starburst with a very old population can successfully reproduce most of their SED characteristics, although we cannot confirm this optically thick component from our spectral analysis.

Key words. galaxies: starburst – infrared: galaxies – galaxies: active – galaxies: evolution

1. Introduction

Mid-infrared (MIR) extragalactic studies have been providing new insights about galaxies in the distant universe, for three main reasons: first, about half of the total energy throughout cosmic history is emitted between the MIR and far-infrared (FIR) wavelengths (e.g. Elbaz et al. 2002; Le Floc’h et al. 2005; Dole et al. 2006; Caputi et al. 2007; Goto et al. 2011a). Second, the effect of dust extinction is much less prominent at MIR wavelengths when compared to optical (OPT) and near-infrared (NIR) wavelengths, and is a good spectral region for measuring activity from star formation as well as active galaxy nuclei (AGNs), even in the presence of copious amounts of dust. Third, under limited technology at the time of AKARI (Murakami et al. 2007) and before, in particular about the large cryogenic space telescope for sharper diffraction-limited resolution and the sensitive detector system, the MIR spectral region has been more sensitive to flux from distant astronomical sources than the FIR one. The importance of deep MIR extragalactic surveys was first recognised by the discovery of strong evolution from 15 μm source counts by using ISOCAM (Cesarsky et al. 1996) onboard the Infrared Space Observatory (ISO; Kessler et al. 1996). The rapidly evolving population was found as an excess of 15 μm sources at a flux of 0.1–0.5 mJy (e.g. Elbaz et al. 1999; Serjeant et al. 2000; see also Lagache et al.

2004; Wada et al. 2008; Pearson et al. 2010). Later, extensive studies at MIR and other wavelengths helped to define the global spectral energy distribution (SED) shapes across the OPT–NIR–MIR–FIR for various types of luminous galaxies (such as AGNs, starburst galaxies, luminous infrared galaxies (LIRGs), and ultra-luminous infrared galaxies (ULIRGs); e.g. (Spinoglio et al. 1995; Pearson 2001; Lagache et al. 2004; Rowan-Robinson et al. 2004; Le Floc’h et al. 2005). Such studies clearly indicate that most of these galaxies, excluding AGNs, show prominent emission features in their MIR spectra, which are believed to originate in polycyclic aromatic hydrocarbons (PAHs; e.g. Lutz et al. 1998; Xu et al. 1998). The luminosity of the PAH features, as well as that of the underlying hot dust continuum, has been used as a measure of star formation rate (SFR), using conversions from MIR luminosity to the FIR one, where the bulk of the energy from star-forming regions is emitted (e.g. Genzel et al. 1998; Rigopoulou et al. 1999; Farrah et al. 2007; Shipley et al. 2016).

The unprecedented sensitivity of *Spitzer* at MIR wavelengths has greatly improved our understanding of cosmic galaxy evolution, with help of various diagnostics of galaxies for their activities up to $z \sim 2$ –4 provided by both MIPS imager (Rieke et al. 2004) at 24 μm and IRS spectrometer (Houck et al. 2004; e.g. Sajina et al. 2007; Yan et al. 2007; Pope et al. 2008; Wu et al. 2010; see also Spoon et al. 2007). Cosmic star formation history,

or star formation rate density (SFRD), in galaxies and AGNs has been particularly examined (e.g. Menéndez-Delmestre et al. 2007; Farrah et al. 2008; Pope et al. 2008; Nordon et al. 2012). See also Goto et al. 2010, 2011a,b). In many studies, the analysis has relied on SED templates or models for scaling from the MIR wavelengths to the bulk of the dust emission in the FIR wavelengths. The scaling is based mostly on studies of nearby galaxies and AGNs; there is no guarantee that it is appropriate at higher redshifts. In some rare cases, extremely deep *Spitzer* FIR photometry was used to directly find global SEDs even at higher redshifts ($z \sim 2-3$; e.g. Le Floc'h et al. 2005; Bavouzet et al. 2008; Murphy et al. 2011). Recent *Herschel* (Pilbratt et al. 2010) FIR photometry has improved the situation (e.g. Berta et al. 2011; Elbaz et al. 2011; Gruppioni et al. 2013; Magnelli et al. 2013). It turned out that their NIR–MIR–FIR SEDs are systematically different from scaled-up versions of local SED templates of presumably the same activity type (e.g. Menéndez-Delmestre et al. 2007; Farrah et al. 2008; Pope et al. 2008; Elbaz et al. 2011; Murphy et al. 2011; Magdis et al. 2012; Nordon et al. 2012). Nordon et al. (2012) argue that this introduces significant offsets in measuring SFRD. They claim that the MIR spectral features are not simple tracers of SFR, but that their power is modulated by changing physical conditions in the interstellar medium (ISM) or in photo-dissociation regions (PDRs; see also Elbaz et al. 2011). This appears reasonable because such an effect has been indeed observed in spatially resolved SINGS studies of local galaxies (Kennicutt et al. 2003), as well as GOALS studies of luminous infrared galaxies (Armus et al. 2009), where a range of MIR spectral features is seen within individual objects (Dale et al. 2006). We note, however, that their integrated properties over the galaxy scale greatly smear out these local variations (Bavouzet et al. 2008).

Another serious problem in analysing galaxy evolution has been the uncertainty in the assumed K -correction used to derive rest-frame quantities (e.g. rest-frame MIR luminosity function and SFRD; Le Floc'h et al. 2005; Caputi et al. 2007; Bavouzet et al. 2008; Nordon et al. 2012). The K -correction to rest-frame monochromatic MIR luminosity is particularly large for redshifted ($z \gtrsim 1$) galaxies because of the contribution of the PAH features. *Spitzer* observed mainly in its IRAC (Fazio et al. 2004) $8\mu\text{m}$ and MIPS $24\mu\text{m}$ bands, which miss the most prominent PAH features around $7.7\mu\text{m}$ at $0.3 < z < 1.8$. Without completely reliable redshift information, interpreting the observed in-band fluxes is not straightforward at MIR. This also introduces a complicated selection function for *Spitzer* colour selection for higher- z sources. For example, sensitive MIPS $24\mu\text{m}$ surveys favour both $z \sim 2$ star-forming galaxies with the redshifted prominent PAH $7.7\mu\text{m}$ feature and AGNs with very red continuum emission. Distinguishing these possibilities has called for IRS spectroscopy (e.g. Yan et al. 2004, 2007; Pope et al. 2008). Although the SED templates have been empirically calibrated to reproduce various observed correlations among broad-band photometric data (e.g. Chary & Elbaz 2001; Lagache et al. 2004), the uncertainties in K -corrections are still large. In particular, to make the MIR part of the templates realistic showing complex MIR spectral features, observed MIR spectra of small number of representative galaxies are often implanted on empirical low-resolution SED templates that are based on a simple synthetic model of dust emission (Dale et al. 2001) or a galaxy stellar evolutionary model in combination with radiative transfer calculation through dusty circum-stellar regions (Polletta et al. 2007).

AKARI was a cryogenic space infrared telescope that observed in the NIR, MIR, and FIR spectral regions

(Murakami et al. 2007). In addition to its primary mission to perform an all-sky survey (Murakami et al. 2007; Ishihara et al. 2010), some time was spent on the deeper pointing-mode observations of some specified targets during an intermittence of the scanning. Multi-band deep extragalactic imaging surveys at NIR and MIR ($2-24\mu\text{m}$) were performed towards the north ecliptic pole (NEP) region by using the pointing mode (the AKARI NEP surveys; Matsuhara et al. 2006 for the summary) with the wide-field infrared camera (IRC; Onaka et al. 2007). The AKARI NEP surveys include as many contiguous bands as possible, with the data covering the entire wavelength range continuously with nine filters at a spectral resolution of $R \simeq 5$. With this filter set, one can discriminate range of SED types, including AGNs with red continuum-dominated SED, normal and star-forming galaxies with hot dust continuum and PAH features, luminous infrared galaxies with strong silicate absorption (peaking at $9.7\mu\text{m}$), up to $z \sim 2$ (see, e.g. Takagi & Pearson 2005; Wada et al. 2008; Takagi et al. 2010; Hanami et al. 2012). As Takagi et al. (2010) demonstrate (see also Hanami et al. 2012; Kim et al. 2012), the MIR colours of redshifted sources show extreme diversity, due to combination of the MIR features from a range of the SED types and redshift, and such rich multi-colour information can be used to extract various information about the nature of the sources. Takagi et al. (2007, 2010) and Hanami et al. (2012) have utilised SED fitting techniques to extract the activity type, redshift, extinction, MIR and FIR luminosities, and so on, from the complex SEDs with much less ambiguity than before. During the course, they also show that some observed SEDs cannot be well reproduced by simple models. Even if the fit seems successful, we need to be cautious, because it relies on local SEDs or very simple physical models to fit observations of redshifted galaxies in which physical conditions may be different from the local ones. Because of the rapid evolution of galaxies peaking at $z \sim 2$ (e.g. Elbaz et al. 1999; Serjeant et al. 2000; Lagache et al. 2004), evolution of the SEDs should be examined and taken into account to interpret various observables, such as source counts and monochromatic MIR luminosities. Spectroscopy of the MIR photometric sample of galaxies in the similar wavelength range would provide a recipe to properly interpret the photometric properties.

The IRC had not only multi-band imaging capability, but also a wide-band low-resolution spectroscopy capability (Ohya et al. 2007). This was possible because the IRC includes transmissive direct-view dispersers (a prism and grisms) in the filter wheel, as well as the broad-band imaging filters. In the spectroscopy mode, by using the short slits at an edge of the field of view (FOV) of the IRC, spectroscopic studies of active galaxies have been extensively done. Especially, the $3.3\mu\text{m}$ PAH feature has been utilised to trace the star formation activities and to diagnose the AGN activity (Imanishi et al. 2008, 2010; Woo et al. 2012; Castro et al. 2014; Ichikawa et al. 2014; Yano et al. 2016). In addition to the regular slit spectroscopy, the IRC could perform slitless spectroscopy: all sources that can be imaged within its $\approx 10' \times 10'$ FOV are dispersed by either a prism or grism. This slitless mode is particularly well-suited to blind spectroscopic surveys of point-like sources: The survey can be unbiased because there is no pre-selection of sources from, such as colour or flux at other wavelengths. Instead, the sources are simply selected after the spectroscopy observations on the basis of their fluxes at the same wavelengths as for the spectroscopy. This is particularly important for studying the MIR evolution of galaxies, because, as noted earlier, it is quite difficult to define a fair sample that is independent of types (including AGN) and strengths of the activities, and redshift for statistical studies.

Sensitive observations with this mode at MIR wavelengths are available only from space to avoid high atmospheric background, and the IRC was the first instrument that provided us with this unique observing opportunity.

In this paper, we first describe the design and observation of our survey programme in Sect. 2.1, and data reduction procedure in Sect. 2.2. Our spectral PAH fit is described in Sect. 2.3, and the results are analysed in Sect. 3.1. The OPT–NIR–MIR broadband photometry is also compiled for the spectroscopic sample in Sect. 2.4, and its basic characteristics are analysed in Sect. 3.2. In particular, we photometrically classify activity types, normal and star-forming galaxies and AGNs, in Sect. 3.2.1. For galaxies with the PAH features detected in their spectra, we analyse their colour-redshift relations in Sect. 3.2.2, and construct their rest-frame SEDs in Sect. 3.2.3. We then compare their spectroscopic and photometric properties in Sect. 3.3. In particular, we compare PAH luminosities measured in both photometric and spectroscopic ways in Sect. 3.3.1, and characterise the variation of the rest-frame SED shape by the spectroscopic properties in Sect. 3.3.2. We here identify the PAH-enhanced population at $z \approx 0.35$ – 0.5 as a distinctive sub-group of the PAH galaxies. Next we compare the observed rest-frame SEDs with various SED templates and models in Sect. 3.4. We discuss implications of the SED variation of the PAH galaxies, in particular the PAH-enhanced population, for the star-formation properties in Sect. 4.1.1. We finally summarise advantages and limits of our slitless spectroscopic and photometric data analysis in Sect. 4.2. Conclusions are given in Sect. 5. We use $H_0 = 70 \text{ km s}^{-1} \text{ Mpc}^{-1}$, $\Omega_m = 0.3$, and $\Omega_\Lambda = 0.7$ throughout this paper.

2. Observations and data

2.1. The SPICY survey: basic design and observations

We conducted our IRC slitless spectroscopic survey, “slitless Spectroscopic survey of galaxies” (SPICY), to study strongly evolving population discovered with ISO that shows an excess in source count at a flux range of 0.1 – 0.5 mJy at $15 \mu\text{m}$ (e.g. Elbaz et al. 1999; Serjeant et al. 2000; Lagache et al. 2004; Wada et al. 2008; Pearson et al. 2010; Sect. 1). Given the typical observed flux ratio between $15 \mu\text{m}$ and $9 \mu\text{m}$ (Sect. 3.2.1 below), this flux range corresponds to 0.5 mJy or smaller at $9 \mu\text{m}$, where the IRC provides the best MIR sensitivity. We targeted the NEP with IRC spectroscopy, where deep extragalactic photometric studies with IRC, NEP-Deep (coverage: 0.57 deg^2 ; 5σ sensitivity at 7 – $12 \mu\text{m}$: $33.6 \mu\text{Jy}$; Wada et al. 2008; Takagi et al. 2012; Murata et al. 2013) and NEP-Wide (coverage: 5.4 deg^2 ; 5σ sensitivity at 7 – $12 \mu\text{m}$: $67.3 \mu\text{Jy}$; Lee et al. 2009; Kim et al. 2012) surveys, were conducted. This SPICY survey thus provides NIR–MIR spectra of sources that have also been detected with the IRC photometric surveys, enabling direct comparisons of the observed characteristics, redshift and PAH luminosity in particular, measured in both photometric and spectroscopic ways. Another advantage of targeting the NEP is that we can utilise many associated surveys at different wavelengths, ranging from X-ray (Krumpe et al. 2015), ground-based OPT–NIR (Jeon et al. 2010, 2014; Ko et al. 2012; Oi et al. 2014), to sub-millimetre (Geach et al. 2017).

We designed the SPICY survey to utilise the IRC spectroscopy capability for optimum survey outputs (see Appendix A for the details). In this paper, we focus only on the short MIR camera within the IRC, “MIR-S” (Onaka et al. 2007), to cover 5 – $13 \mu\text{m}$, although the survey was designed to utilise all three cameras of the IRC for its full wavelength coverage (2.5 – $24 \mu\text{m}$).

This MIR-S camera is suited for studying galaxies at $z \lesssim 0.5$ by using prominent PAH features at 6 – $10 \mu\text{m}$ in the rest frame. We visited the same pointing coordinates nine or ten times to achieve the sensitivity goal of 0.5 mJy at $9 \mu\text{m}$ for a tile of $\approx 10' \times 10'$ corresponding to one FOV of this camera. The actual tile shape, after stacking all individual pointing data, is slightly elongated and distorted because of a slight field rotation among the observations, which is unavoidable due to constraints posed by the satellite’s orbit and the NEP coordinates. We aimed to overlap tiles of all three different cameras of the IRC to increase the overall wavelength coverage. As a result, 14 tiles are distributed in a non-contiguous way around the NEP, in a form of a complicated shape of folded chains (Fig. 1). We tried to concentrate on the NEP-Deep field where more observations at other wavelengths are available, but some tiles are made within the surrounding Wide survey field, which encompasses the Deep field.

We used a standard AOT (Astronomical Observing Template) for IRC spectroscopy, AOT04a (Onaka et al. 2007), for the SPICY observations. Within one pointing observation lasting about $\approx 10 \text{ min}$, several spectroscopic images through dispersers, as well as a few direct images through a broad-band filter, are taken in this AOT. In the MIR-S camera, both lower-resolution ($R \approx 50$) dispersers (SG1 and SG2 grisms covering 4.6 – $9.2 \mu\text{m}$ and 7.2 – $13.4 \mu\text{m}$, respectively) and a broad-band filter (S9W, covering 6.7 – $11.6 \mu\text{m}$ with an effective wavelength of $9.0 \mu\text{m}$) are used. The direct image, also called a reference image, is used to provide wavelength reference points for all sources on the spectroscopic images. No telescope dithering is made within the AOT, to ensure that the reference image provides accurate wavelengths. Within one AOT operation, as many as 12 SG1 images, 12 or 16 SG2 images, and three S9W images, are taken, and the effective exposure time is 6.36 sec for each image independently of the filters or grisms used. In total, exposure times are 4796 sec (for 12 images per pointing and nine pointings)– 7106 sec (for 16 images per pointing and ten pointings) for both SG1 and SG2 spectra per tile.

2.2. Data reduction

We reduced the SPICY data by using the IRC spectroscopy toolkit (collection of software and calibration database) modified for our multi-pointing observations. The original toolkit was developed by the instrument team¹ to reduce single AOT observation dataset (Ohshima et al. 2007). This toolkit is composed of the two parts: an image processing and calibration pipeline, and a spectrum plotting tool. The former is to reduce raw images to generate calibrated and stacked spectral images, and the latter is to extract and plot one-dimensional spectra. Both parts are based on calibration database provided with the toolkit. The pipeline performs standard array image processing such as dark subtraction, flat-fielding, and background subtraction, and also extracts two-dimensional spectral images for individual sources detected on a reference image, and stacks them. To work on the multiple AOT observation datasets, we modified the pipeline while keeping all original calibration routines and database. Specifically, we split the original pipeline into two pieces, one for image processing, calibration, and source extraction, and another for stacking the pre-calibrated and extracted spectral images. We then added a simple file organising mechanism between them, in order to collect all individually calibrated images taken at different AOT observations for the same tile before stacking all of them at the same time.

¹ The spectroscopy toolkit is available at <http://www.ir.isas.jaxa.jp/AKARI/Observation/support/IRC/>

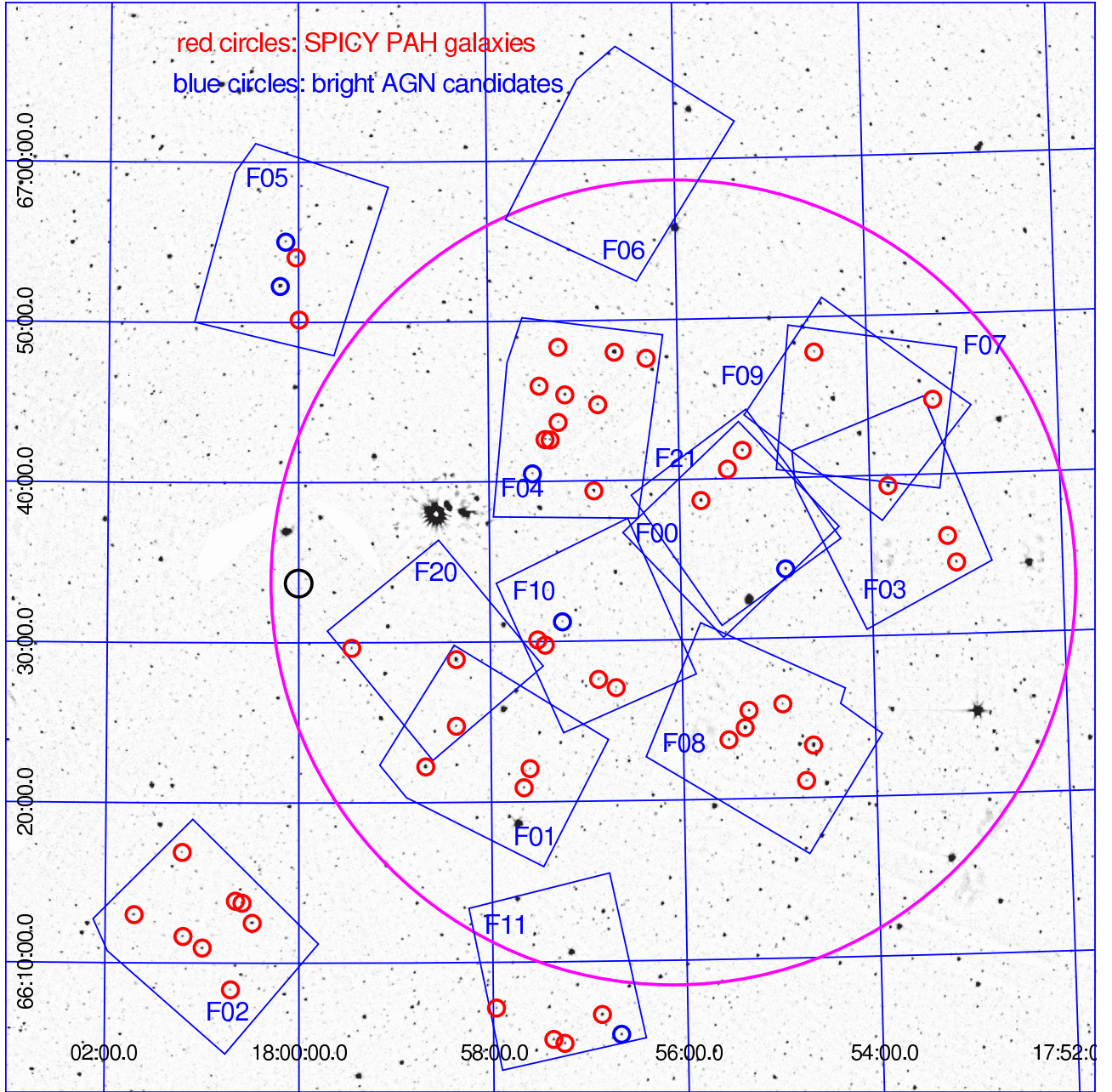


Fig. 1. SPICY survey tiles marked on the IRC NEP-Wide S9W image (Lee et al. 2009; Kim et al. 2012). North is up and east is to the left. The NEP is marked with a small black circle, and the NEP-Deep survey field is indicated with a big magenta circle. Blue rectangles show approximate locations of individual tiles. The galaxies with detectable PAH features (the PAH galaxies; Sect. 2.3) and bright AGN candidates (Sect. 3.2.1) are marked with small red and blue circles, respectively.

In order to run the spectroscopy pipeline for sources that are too faint to be clearly detected on a reference image of a single AOT observation, one needs to find their positions by using multiple AOT observations beforehand. This is because the pipeline cannot apply the wavelength-dependent calibration without knowing the wavelength reference point. Therefore, we first generated a master reference image by stacking all reference images of multiple AOT observations for a tile. We used the IRC imaging toolkit (Ita et al. 2008)² to stack the reference images. In this imaging toolkit, the flux scale and sky coordinates (RA and

Dec) are calibrated after standard array image processing such as dark subtraction, flat-fielding, and background subtraction. We detected sources in the master reference image, and created a master source catalogue that includes their fluxes and sky coordinates. To meet our sensitivity goal, sources that are brighter than 0.3 mJy at S9W (9.0 μ m) were selected for processing with the spectroscopy pipeline. We also reduced the individual reference images for each AOT observation in the same way as reducing the master reference image. We then transformed the sky coordinates of the master reference catalogue to the pixel coordinates of individual single-AOT reference images to generate source tables. We next ran the first part of the spectroscopy pipeline (image processing, calibration, and source extraction) for individual AOT observations with their corresponding source tables. We here used our

² The imaging toolkit is the data reduction software for the IRC imaging datasets developed by the instrument team. It is also available at <http://www.ir.isas.jaxa.jp/AKARI/Observation/support/IRC/>

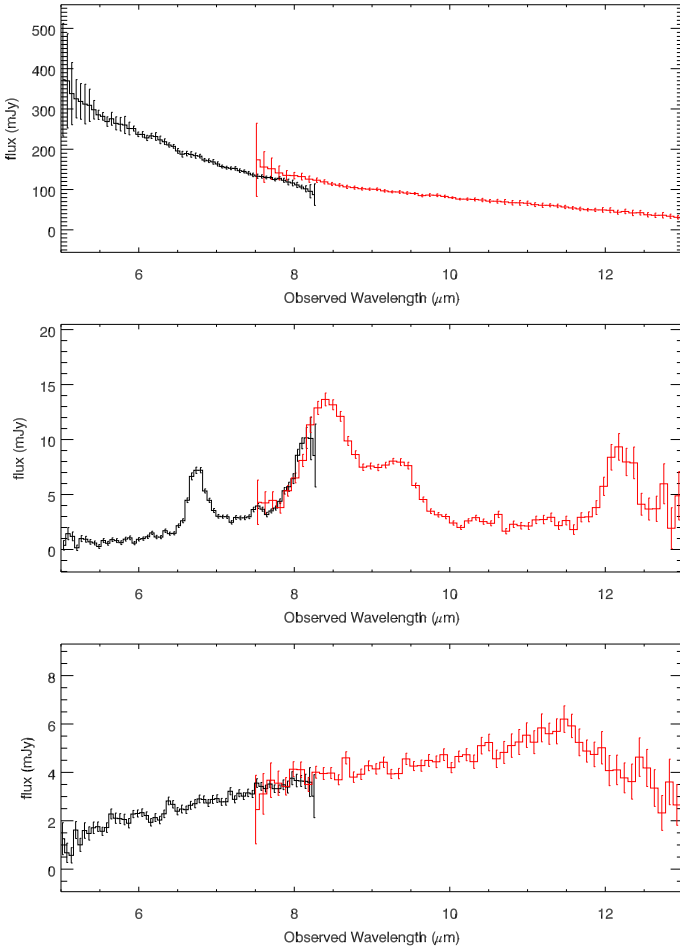


Fig. 2. Examples of the SPICY spectra of three representative types of bright sources. The SG1 (black) and SG2 (red) spectra are shown separately. The error bars are for one sigma. *Top:* field star. *Middle:* galaxy with prominent PAH 6.2, 7.7, 8.6, and 11.3 μm features (F04-0 at $z_{\text{PAH}} = 0.087 \pm 0.001$; see also Fig. B.1). *Bottom:* AGN candidate with a red featureless continuum and possibly a deep silicate 9.7 μm absorption redshifted to $\approx 14 \mu\text{m}$ (F05-1 at $z_{\text{opt,spec}} = 0.4508$; see Sect. 3.2.1). Slight flux offset of the star spectrum within the overlapping wavelength range of the SG1 and SG2 spectra (7.5–8.2 μm) is due to slight systematic flux calibration error caused by errors in aligning the SG1 and SG2 spectral images. Increased noise level at $\geq 12.0 \mu\text{m}$ in the *middle panel* is caused by partial truncation of the SG2 spectrum.

additional file organising software tool to organise lists of images to be stacked for the same sources taken at different AOT observations, and stacked the pre-calibrated and extracted spectral images for each of the sources by using the second part of the spectroscopy pipeline. By using the original plotting tool, we finally extracted fully calibrated one-dimensional spectra, and saved the results for further analysis. Examples of the final processed spectra of bright sources showing very different spectral shapes are shown in Fig. 2.

Due to slitless nature of the observing mode, we obtained spectra of all kinds of compact sources within a FOV. We removed field stars based on their (very bright and point-like) appearance on the CFHT optical images (Hwang et al. 2007), and find 171 extragalactic sources (galaxies and AGNs). We find that all PAH galaxies (sources with detectable PAH features; Sect. 3.1) are extended at the resolution of $FWHM \approx 1''0$. Their stellarity indices, which quantify morphological similarity of objects to point-like sources and are often used for shape-based star–galaxy classification (Bertin & Arnouts 1996), are

< 0.1 (0 for galaxies and 1 for stars) on the CFHT optical images (Hwang et al. 2007). Among all 171 spectra, some fraction of the spectra is not useful in our analysis. Some of them are heavily contaminated by nearby sources on the slitless spectral images, and some others near the edge of the FOV have only truncated spectra at the edge of the detector array³. We note that these problems randomly damage the spectra depending on distributions of the sources and their neighbours. Among the sources with useful spectra, eight sources are observed twice within the overlapping tiles (Sect. 2.1), duplicating the spectra for such sources. For the brightest four such sources, we adopted ones that are less affected by the contamination. For the remaining four such sources, we coadded the spectra to improve the signal-to-noise.

2.3. Spectral PAH fit

2.3.1. Method

Many SPICY spectra show 6.2, 7.7, 8.6, and 11.3 μm PAH features (hereafter, PAH 6.2 μm , PAH 7.7 μm , PAH 8.6 μm , and PAH 11.3 μm , respectively), and they are examined by using spectral PAH fitting. We first examine some bright sources showing prominent PAH features with PAHFIT software (Smith et al. 2007). This software relies on a priori information on shapes of individual PAH features (a set of central wavelengths and widths, assuming a Drude profile) and central wavelengths of narrow lines of ionised, atomic, and molecular gases. With external information on redshift, the software finds strengths of these spectral features, as well as the underlying continuum and amount of extinction, by means of a chi-square minimisation. Figure 3 shows the results of two nearby bright galaxies as examples. Here, we assumed a fully mixed extinction geometry and the extinction curve towards the Galactic centre developed by Smith et al. (2007). We adopted redshifts measured with our own PAH fit software (see below). Although we find reasonably good fits on them, the spectral model of PAHFIT is too detailed for analysing the SPICY spectra. This is understandable because PAHFIT is designed for the IRS low-resolution spectra ($R = 60\text{--}130$; $\approx 5\text{--}35 \mu\text{m}$), which provide higher spectral resolution and wider wavelength coverage than those of the SPICY spectra ($R \approx 50$; $\approx 5\text{--}13 \mu\text{m}$).

We develop our own spectral PAH fit (hereafter, simply “the PAH fit”) to apply to the SPICY spectra. Most of the sources in the slitless surveys are faint and serendipitously detected. We aim to establish a way to robustly extract fundamental properties of star-forming galaxies from the slitless survey data. To identify sources on the spectral images, it seems more efficient to use (only) the PAH features that are prominent in terms of both line width and flux. Therefore, we designed this software to detect (even very faint) PAH features on low-resolution IRC spectra, and robustly measure their redshifts and PAH strengths, without any a priori information about the sources. For this purpose, we adopted a simple spectral model with only four major PAH features (at 6.2, 7.7, 8.6, and 11.3 μm) at the same redshift on a power-law continuum, to minimise number of the free parameters. Each PAH feature is known to show an extended wing in its profile that contains much more power than in a Gaussian profile (e.g. Smith et al. 2007). We compared the Lorentzian and

³ The FOV of the IRC imaging mode occupies almost the entire detector footprint. By inserting a direct-view disperser (grism) in place of a broad-band filter, the dispersed spectral images of sources near the edge of the imaging FOV extend beyond the detector footprint, resulting in the truncation.

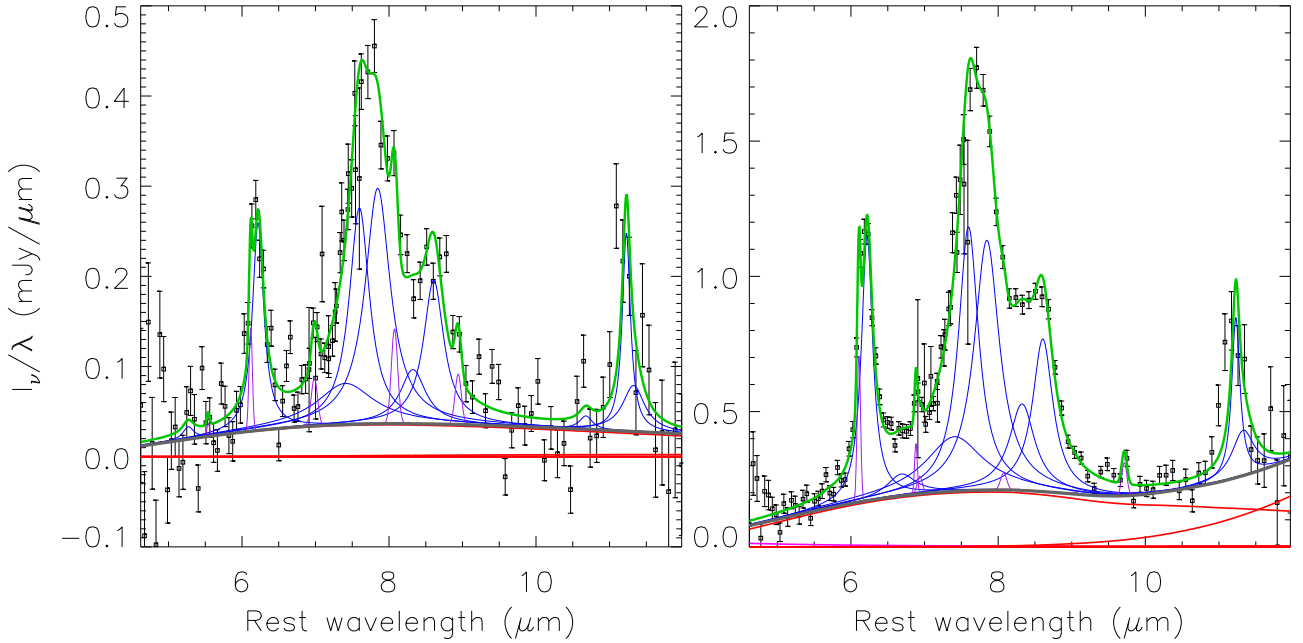


Fig. 3. Results of the PAHFIT for two nearby SPICY PAH galaxies. Individual PAH features (blue), narrow emission lines (magenta), dust continua (multiple components for different temperatures; red), stellar continua (magenta), sum of the continua (dust and stellar; grey), and sum of all components (continua and spectral features; green) are shown for each galaxy.

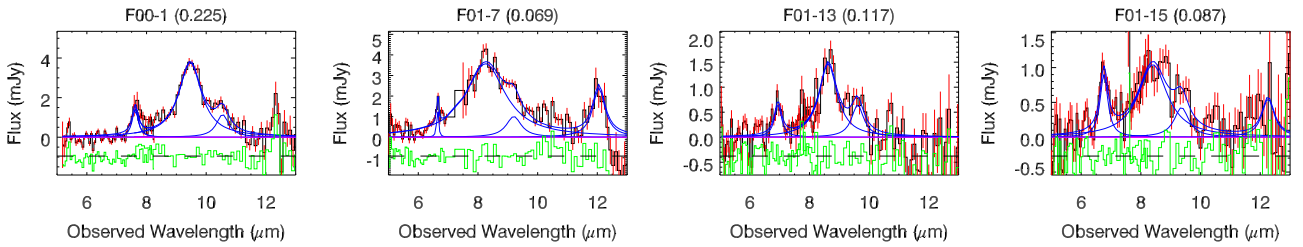


Fig. 4. Example SG1 and SG2 spectra of the SPICY PAH galaxies with the PAH fit results overlaid. All 48 spectra can be found in Fig. B.1. The observed spectrum is shown in red line with one-sigma error bars, with the fitted individual PAH components (blue), the power-law continuum (magenta), and their sum (blue) in each panel. The residual of the fit (observed–fitted) is shown in green at offset baseline (horizontal broken line) for clarity. The redshift from the PAH fit is indicated next to the source name in the plot title. The Y axis is scaled to have the same PAH 7.7 μm peak height for all galaxies.

Drude (Smith et al. 2007) profiles by using the PAH fit on the SPICY spectra, and find only negligible differences, and adopted the Lorentzian profile simply because of its simpler functional form. Narrow (unresolved) emission lines are not included in the fit, because no such lines are clearly detected in our spectra due to low spectral resolution (Fig. 4). Free parameters in our fit are the shape parameters (Lorentzian amplitudes and width (half width at half maximum; HWHM)) of the four PAH features, slope and amplitude of the power-law continuum, and redshift. We required the width of all PAH features to be larger than the instrumental spectral resolution. The fit was made by means of a chi-square minimisation.

2.3.2. Tests

We test the PAH fit on “noise-free galaxy spectral templates” of Smith et al. (2007) and an averaged spectrum of nearby starburst galaxies of Brandl et al. (2006; Fig. 5), both of which are obtained with the IRS low-resolution mode. We note that Smith et al. (2007) constructed the four templates to cover ranges of PAH inter-band flux ratios in their sample. We find the following problems in the fit, and revised the fitting procedure to apply to the SPICY spectra. One problem is the systematic

residual (observed–fitted) features, in particular around the peaks of the PAH 7.7 μm and 11.3 μm , as well as at narrow emission lines of, for example, [Ar II] at 7.0 μm and H₂ 0–0 $S(3)$ at 9.7 μm . Such residuals are naturally expected because the PAH 7.7 μm complex is actually composed of multiple PAH components (Smith et al. 2007), and these narrow lines are not included in the spectral model. Therefore, we decided to ignore this problem. Another problem is that a pseudo plateau at red side of the PAH 11.3 μm up to $\sim 13 \mu\text{m}$, which is made by a collection of weak PAH features (see, e.g. Fig. 4 of Smith et al. 2007), cannot be well reproduced with our simple spectral model. To mitigate this problem, we decided to fit the spectra only below 11.5 μm in the rest frame just to include the peak of the PAH 11.3 μm and a bit of its red side. To work on the actual redshifted spectra, we need to tailor the fitting wavelength according to the source redshift by following the two steps: first, we fitted the entire spectral region to find approximate redshift (z_0). This redshift is almost accurate because its measurement relies mostly on more prominent PAH 6.2 μm and 7.7 μm . Second, we restricted the fitting wavelength up to $11.5 \times (1 + z_0) \mu\text{m}$ to find the final fit results.

We also test the PAH fit on the SPICY spectra, and find that the fit sometimes returns unusually wide PAH 11.3 μm

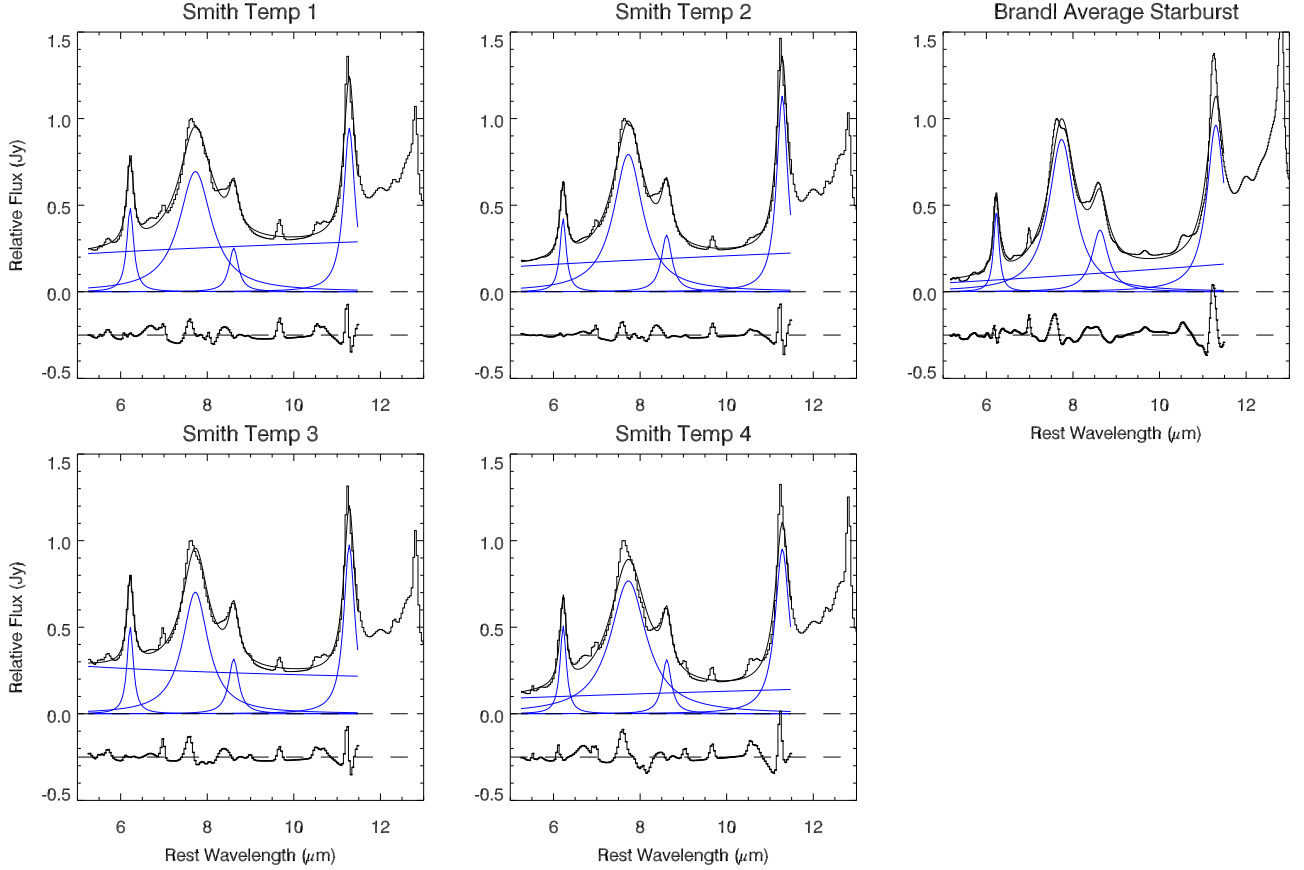


Fig. 5. Representative IRS spectra of star-forming galaxies with the PAH fit results overlaid. An averaged spectrum of nearby starburst galaxies of Brandl et al. (2006; top right) and four “noise-free galaxy spectral templates” of Smith et al. (2007; remaining four panels) are shown in black lines. The individual PAH features (blue), the power-law continuum (blue), and their sum (black) are overlaid in each panel. The residual of the fit (observed–fitted) is shown at offset baseline (horizontal broken line) for clarity.

profile width when compared to the results on the IRS templates described above, particularly when the signal-to-noise is low. This is most likely because we cannot firmly constrain the PAH 11.3 μm profile due to limited wavelength coverage, particularly when this feature comes near the end of our wavelength coverage due to redshift. This feature goes out of the wavelength coverage at $z \gtrsim 0.2$. Therefore, we limited the allowed range of this width in the fit just to include the measured widths on the IRS templates, and considered the fit valid even when the best fit is found at the limits. We find, by changing this allowed width range, that other fit parameters (parameters of other PAH features and redshift) are insensitive to this fit condition. Because of such problem in the profile fitting, we decided not to discuss the PAH 11.3 μm properties in detail in this paper.

We do not include extinction in the PAH fit on the SPICY spectra, and here discuss potential problems in neglecting the extinction and how to mitigate them in our following analysis. We tested the extinction effect with an extinction fitting in the PAH fit, and find that the extinction cannot be well constrained for many sources due to limited wavelength coverage at long side of the redshifted silicate absorption feature. We adopted an extinction curve towards Galactic centre of Chiar & Tielens (2006) that shows a prominent broad (8–12 μm) silicate absorption feature peaking at 9.7 μm , and assumed a screen geometry. At $z < 0.15$, we find that the optical depth at 9.7 μm is typically $\tau(9.7 \mu\text{m}) \lesssim 0.01$ (or $A_V \lesssim 0.1$ mag) for bright sources, and $\tau(9.7 \mu\text{m}) \lesssim 0.1$ (or $A_V \lesssim 1$ mag) with very large uncertainties for fainter sources. At $z \gtrsim 0.2$, we cannot constrain the extinction for most cases, because peak of the

PAH 11.3 μm goes out of our wavelength coverage, and PAH-free region at red side of the PAH 8.6 μm comes at the end of the coverage. The silicate absorption profile is not fully covered at this redshift range, and quality of the extinction measurement becomes worse particularly when the signal-to-noise is low. Given the uncertainties of the extinction, measurements of the PAH 7.7 μm and PAH 6.2 μm are more robust than that for the PAH 11.3 μm . This is because the silicate absorption profile extends to $>11.3 \mu\text{m}$, whereas it does not to $<7.7 \mu\text{m}$. In contrast, the redshift measurement is little affected by the extinction, because it relies much more on fits over the PAH 6.2 μm and 7.7 μm . Therefore, we decided not to include extinction in the fit for all sources, and will focus mostly on the luminosities of both PAH 6.2 μm and 7.7 μm , as well as redshift, in our following analysis. Section 4.1.2 shows more discussion about the extinction based on photometric information.

We finally examine accuracy of redshifts from the PAH fit by comparing to those from the optical spectroscopy. We identify 32 galaxies with detectable PAH features in the SPICY spectra with secure⁴ optical redshifts either by Shim et al. (2013), Oi et al. (2014), or our own observations (Table C.2). In our own observations, we performed optical spectroscopy with the OSIRIS at the Gran Telescopio Canarias (GTC) in 10A and 14A semesters (PI: T. Miyaji). We find that redshifts from the PAH fit are accurate at a level of 1% or less in $dz/(1+z)$ (Fig. 6).

⁴ We adopted the optical redshifts if their “quality flags” are either four (secure; identified by more than two features) or three (acceptable and almost good; identified by two features) according to Shim et al. (2013).

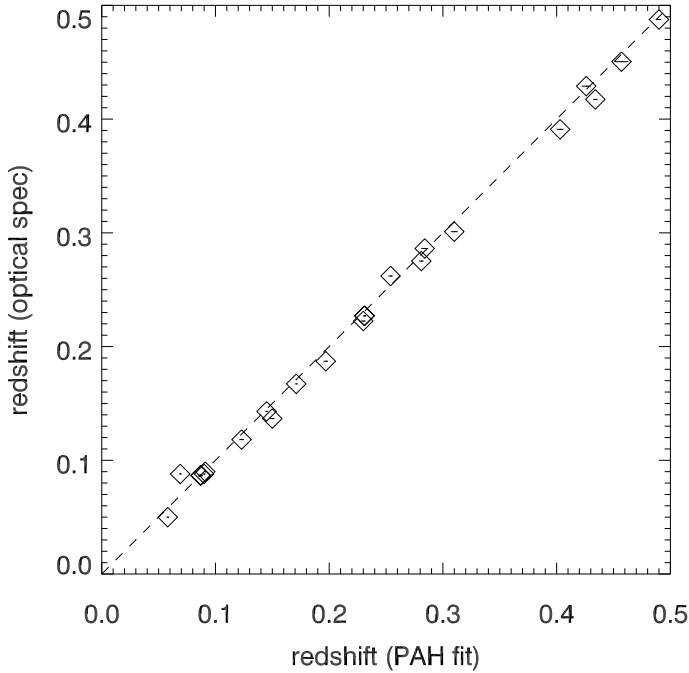


Fig. 6. Comparison of the redshifts between the PAH fit and optical spectroscopy for the PAH galaxies. Error of the optical spectroscopic redshift is not shown, but we plot only the sources with good redshift measurements (quality flag of 3 or 4 in Shim et al. 2013; see text). The diagonal broken line is for the same redshifts in the two measurements.

2.3.3. Results

We fitted all extragalactic SPICY spectra with the PAH fit, and identify 48 “PAH galaxies” with successful PAH fits (Fig. 4). We refer to those without PAH detections (i.e. sources with unsuccessful PAH fits) as “non-PAH galaxies”. Some of the non-PAH galaxies are bright and photometrically similar to the PAH galaxies (Sect. 3.2.1), but we cannot detect their PAH features due to problems in the spectral data (contamination and truncation; Sect. 2.2). Other non-PAH galaxies show either lower signal-to-noise spectra or intrinsically weak PAH features (e.g. elliptical galaxies without prominent PAH features or AGNs), and the PAH fit fails to detect the features. Table 1 summarises numbers of sources in each category. Table C.1 shows source identification, cross-identification with the IRC NEP-Wide catalogue (Lee et al. 2009; Kim et al. 2012), and the SPICY S9W (9.0 μ m) photometry of the PAH galaxies, as well as cross-identification with the CFHT optical NEP photometric catalogue (Hwang et al. 2007).

We compare the SPICY PAH galaxies and the IRS spectral templates of nearby star-forming galaxies (Brandl et al. 2006; Smith et al. 2007) by using the PAH fit. Figure 7 shows distributions of widths of both PAH 6.2 μ m and PAH 7.7 μ m, and an inter-band flux ratio of the PAH 6.2 μ m to the PAH 7.7 μ m of the SPICY spectra⁵. We find that all these parameters are similar to those of the IRS templates. The PAH 6.2 μ m is not resolved in most SPICY spectra, because the wavelength resolv-

ing width of our instrument is slightly larger than the widths of the PAH 6.2 μ m of the IRS templates. We also measured equivalent widths of the PAH 6.2 μ m for the SPICY PAH galaxies to be mostly 0.8–2.0 μ m (with a median of 1.4 μ m). They are consistent with those of the IRS spectral templates showing 0.6 μ m (template three of Smith et al. 2007)–2.3 μ m (average starburst of Brandl et al. 2006). They are also consistent with those of typical starburst galaxies reported in literature (e.g. Brandl et al. 2006; Spoon et al. 2007; Weedman & Houck 2008).

We measured integrated (under the PAH profile) spectroscopic PAH luminosities of the PAH 6.2 μ m, $L_{\text{PAH}}(6.2 \mu\text{m})$, and the PAH 7.7 μ m, $L_{\text{PAH}}(7.7 \mu\text{m})$ of the PAH galaxies by using the PAH fit. We also measured the spectroscopic monochromatic luminosity at the PAH 7.7 μ m peak, $\nu L_{\nu \text{ spec}}(7.7 \mu\text{m})$ (hereafter, spectroscopic monochromatic luminosity at 7.7 μ m; also called as peak luminosity of the PAH 7.7 μ m; Weedman & Houck 2008) by using the PAH fit. This spectroscopic monochromatic luminosity includes contributions of the underlying continuum. Table C.2 lists the PAH fit results of the PAH galaxies as well as the optical spectroscopic redshifts.

2.4. Multi-band photometry

We compiled photometric information for all SPICY extragalactic sources at OPT–NIR–MIR wavelengths. The NEP-Wide photometric catalogue (Lee et al. 2009; Kim et al. 2012) provides eight IRC filter fluxes ($N2$, $N3$, $N4$, $S7$, $S9W$, $S11$, $L15$, and $L18W$ ⁶) centred approximately at 2.4, 3.2, 4.1, 7.0, 9.0, 11.0, 15.0, and 18.0 μ m, respectively (see Onaka et al. 2007 for more filter specifications). We do not use the $L24$ (22.9 μ m) flux in our analysis, because it is much shallower than the others, although it is included in the catalogue. We compared the SPICY S9W photometry of the PAH galaxies (Sect. 2.3.3) with that in the NEP-Wide catalogue, and find that they are consistent with each other (Fig. 8). The CFHT optical NEP photometric catalogue (Hwang et al. 2007) provides five optical filter fluxes (u^* , g' , r' , i' , and z'). In total, as many as 13-band broad-band photometric data, covering 0.37–18 μ m, are available. Tables C.3 and C.4 show the NIR–MIR and OPT photometries of the PAH galaxies, respectively. Because the photometric catalogues are deeper than the SPICY spectroscopy (>0.3 mJy at S9W), almost all photometric data across OPT–NIR–MIR wavelengths are available, although the u^* band is often unavailable due to faintness of the sources and limited sensitivity in this band.

3. Analysis and results

3.1. Spectroscopic characteristics

The redshift distribution of the SPICY PAH galaxies extends up to $z \approx 0.5$, with a few notable narrow peaks (left panel of Fig. 9). Such peaks are likely due to real galaxy distribution towards the NEP, rather than due to our source selection bias. The S9W filter (6.7–11.6 μ m) used for our source selection (Sect. 2.1) is broad and covers most of the redshifted PAH 7.7 μ m in our redshift coverage ($z = 0.0$ – 0.5). The similar redshift distribution with three notable peaks ($z \lesssim 0.1$, $z \lesssim 0.2$, and $z \lesssim 0.3$; right panel of Fig. 9) is also found in the optical spectroscopic survey towards the NEP

⁵ We do not show parameters involving the PAH 8.6 μ m (inter-band flux ratios of PAH 8.6 μ m/PAH 7.7 μ m and PAH 8.6 μ m/PAH 6.2 μ m, and the PAH 8.6 μ m widths), and will not discuss them in the following. This is because they typically show much larger uncertainties than for other PAH features, and this is likely caused by our low spectral resolution ($R \approx 50$) to clearly isolate this feature on the profile of nearby stronger PAH 7.7 μ m.

⁶ The IRC has three optical channels, “NIR”, “MIR-S” (S for short), and “MIR-L” (L for long), and each channel has filters whose names start with “N”, “S”, and “L”, respectively. These initial characters are followed by approximate central wavelengths of the filters in μ m. Both S9W and L18W filters cover wider wavelength ranges than other filters, and their names include “W” (for wide) after the wavelengths.

Table 1. Numbers of SPICY sources in different classifications discussed in this paper.

Classification	N Total (bright)	Redshift bin	N (PAH galaxies) Sub-total (PAH enhanced)
AGN candidates	11 (6)		
Non-PAH galaxies	112 (39)		
PAH galaxies	48 (24)	Nearby	13 (0)
		Mid- z	23 (1)
		Higher- z	12 (9)
Total	171 (93)		48 (10)

Notes. In each classification, numbers of the bright samples (Sect. 3.2.1) are shown in parentheses. For the PAH galaxies, their numbers for each redshift bin (Sect. 3.1) are also shown. Numbers of the PAH-enhanced galaxies (Sect. 3.3.2) are shown in parentheses.

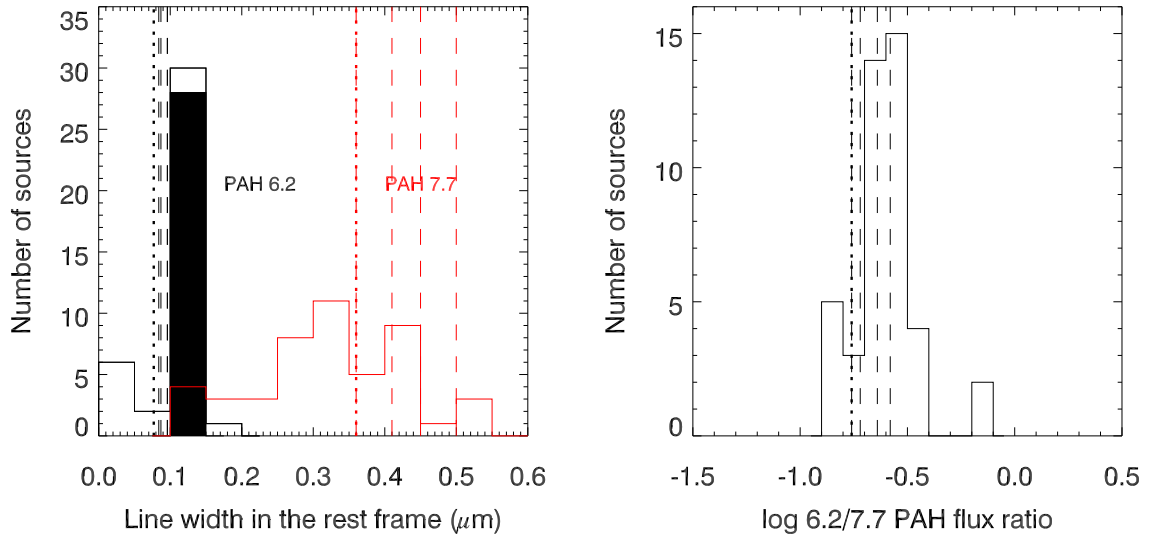


Fig. 7. Distributions of the PAH shape parameters of the PAH galaxies. *Left:* PAH widths (Lorentzian half width at half maximum (HWHM) in the rest frame) of the PAH $6.2\,\mu\text{m}$ (black) and the PAH $7.7\,\mu\text{m}$ (red). The wavelength resolving widths of our instrument are subtracted from the measured widths in quadrature. When the PAH $6.2\,\mu\text{m}$ is unresolved, the instrumental width is used to indicate the upper limit of the intrinsic width (filled histogram). *Right:* inter-band flux ratio of PAH $6.2\,\mu\text{m}$ /PAH $7.7\,\mu\text{m}$. In both panels, corresponding measured parameters of the IRS starburst templates of Brandl et al. (2006; one template; dotted line) and Smith et al. (2007; four templates; dashed lines) are indicated by vertical lines.

by Shim et al. (2013), in spite of their slightly different survey coverage and target selection functions from us. In particular, the first redshift peak is due to a supercluster at $z \approx 0.087$ towards the NEP (Ko et al. 2012). At $z \gtrsim 0.5$, the red side of the most prominent PAH $7.7\,\mu\text{m}$ goes out of our wavelength coverage ($\gtrsim 13\,\mu\text{m}$; see Sect. 3.3.2 for more discussion), and no PAH galaxies are detected in this redshift range. In the following, we group our sample by redshifts into three bins. Redshift ranges of the bins are defined as $z < 0.1$, $0.1 < z < 0.35$, and $0.35 < z < 0.5$, and numbers of the sources are 13, 23, and 12 in the respective bins (Table 1). We respectively call them nearby, mid- z , and higher- z bins in the following. The boundary between the mid- z and higher- z bins is set so that the peak at $z \lesssim 0.3$ is included in the mid- z bin. The boundary between the nearby and mid- z bins is set so that the peak at $z \lesssim 0.1$ is included in the nearby bin.

3.2. Photometric characteristics

3.2.1. Broad-band colours and photometric type classification

We first compare the $S9W$ ($9.0\,\mu\text{m}$) and $L15$ ($15.0\,\mu\text{m}$) fluxes of the SPICY sources. The $S9W$ band is the source detection band in our survey, and the $L15$ band is similar to the

LW3 band of the ISOCAM, which was extensively used for the ISOCAM deep extragalactic surveys (Sect. 1). Figure 10 shows number distributions of the sources as a function of $\log L15/S9W$. The non-PAH sources are shown separately for bright and faint sources, because detection of the PAH features depends on the MIR fluxes. We refer to sources that are brighter than $0.3\,\text{mJy}$ in all $S7$ ($7.0\,\mu\text{m}$), $S9W$ ($9.0\,\mu\text{m}$), and $S11$ ($11.0\,\mu\text{m}$) bands as “bright” sources, because the PAH $7.7\,\mu\text{m}$, if any, is expected to be detected at least in one of the three bands. All other sources are referred to as faint sources. Numbers of the bright sources are summarised in Table 1. We find that $\log L15/S9W$ shows a tight distribution around ≈ 0 , with a typical scatter of ± 0.2 , for both PAH and non-PAH sources (see also Sect. 3.2.2), excluding the AGN candidates (see below for the definition and identification of the AGN candidates) showing larger $\log L15/S9W \approx 0.3$.

We then analyse the relationship among broad-band colours, or flux ratios, of the SPICY sources to broadly characterise their SED types. We compare $N3$ ($3.2\,\mu\text{m}$)/ $N2$ ($2.4\,\mu\text{m}$) and $S7$ ($7.0\,\mu\text{m}$)/ $N3$ ($3.2\,\mu\text{m}$) between the observations and the SED templates (Fig. 11). Takagi et al. (2010) adopted this colour combination by following the colour diagram of $[3.6] - [5.8]$ vs. $[4.5] - [8.0]$ with IRAC to identify AGN candidates (Lacy et al. 2004; see

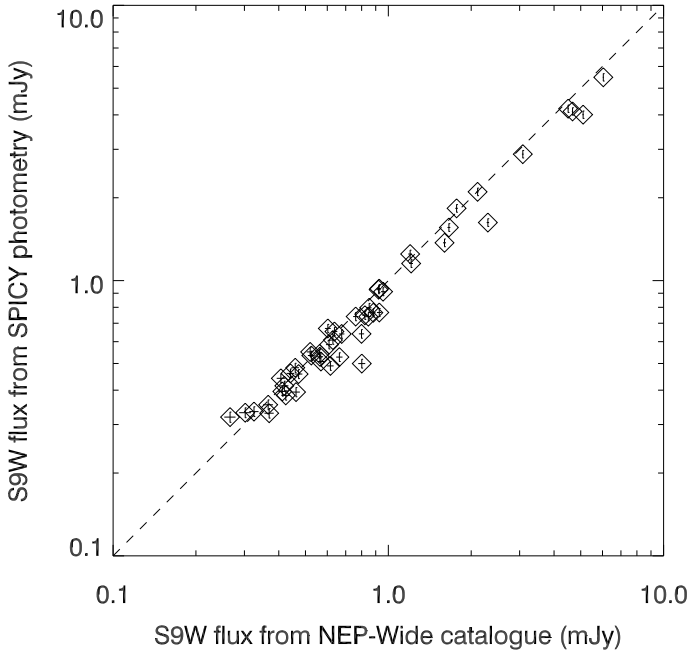


Fig. 8. Comparison between the $S9W$ ($9.0\mu\text{m}$) SPICY photometry of the PAH galaxies and that in the NEP-Wide catalogue. The diagonal broken line is for the same fluxes in the two measurements.

also Takagi et al. 2007). We adopted SED templates of elliptical (E), late type spiral (Sc), starburst (M 82), LIRG (NGC 6090⁷), and AGN (Mrk 231) from the SWIRE library (Polletta et al. 2007), and calculated their colours for a range of redshift. Most PAH galaxies are blue at NIR ($-0.3 \lesssim \log N3/N2 \lesssim 0.0$) and blue-moderately red at NIR-MIR ($-0.2 \lesssim \log S7/N3 \lesssim 0.5$). Their $S7/N3$ colour gets bluer with redshift, as predicted by the templates of Sc, starburst, and LIRG. Some of the non-PAH sources show very blue $S7/N3$ ($\log S7/N2 < -0.2$) or red $N3/N2$ ($\log N3/N2 > 0.1$) colours. The former can be reproduced by the templates of Sc, E, or their intermediate types (e.g. Sa). The latter can be reproduced only by the AGN template in a wide redshift range (at least up to $z \sim 3$; Fig. 11). It is known that red continuum-dominated power-law-like SED at OPT-MIR ($\alpha \sim -1$ where $f_\nu \propto \nu^\alpha$; e.g. Edelson et al. 1987; Elvis et al. 1994) makes an AGN red in both NIR/NIR and MIR/NIR colours in the very wide redshift range (e.g. Lacy et al. 2004; Donley et al. 2012). To confirm this, we examined observed SEDs of the latter sources (Fig. 12), and find that they indeed show red continuum-dominated, AGN-like SEDs at NIR-MIR wavelengths. In contrast, all kinds of galaxy templates (E, Sc, starburst, and LIRG) predict blue NIR colour ($\log N3/N2 < 0.0$) at $z = 0.0-0.5$, because the NIR bands cover the stellar bump peaking at $1.6\mu\text{m}$ (see also Fig. 13). Takagi et al. (2010) confirm that most of such $N3/N2$ -red sources in their NEP-Deep photometric sample are indeed AGNs with optical spectroscopy. Therefore, red NIR colour is a clear AGN signature in our redshift coverage ($z = 0.0-0.5$).

We define the AGN candidates in the $N3$ ($3.2\mu\text{m}$)/ $N2$ ($2.4\mu\text{m}$) and $S7$ ($7.0\mu\text{m}$)/ $N3$ ($3.2\mu\text{m}$) diagram (Fig. 11). We

required that the AGN SED template is clearly separated from a range of the galaxy templates in this colour-colour diagram, and that all PAH galaxies are classified as non-AGNs. We set two colour conditions for the AGNs: $\log N3/N2 > 0.1$ and $\log S7/N3 > 0.0$. The secondary colour condition is useful to separate galaxies and AGNs at $0.35 < z < 0.5$, when both types are closer in $N3/N2$ while they are more separated in $S7/N3$. We identify 11 AGN candidates (including six bright ones), and Table 1 includes their numbers. In the following, we pay more attention to the bright AGN candidates, because we are sure about intrinsic faintness of their PAH features. The number fraction of the bright AGN candidates is 9% (=6 bright AGN candidates/(45 bright non-PAH galaxies including the bright AGN candidates+24 bright PAH galaxies)) among all bright sources. Table C.5 shows source identification, cross-identification with the NEP-Wide catalogue (Lee et al. 2009; Kim et al. 2012), and the SPICY $S9W$ ($9.0\mu\text{m}$) photometry of the bright AGN candidates, as well as cross-identification with the CFHT optical NEP photometric catalogue (Hwang et al. 2007) and the optical type classification by Shim et al. (2013). Tables C.6 and C.7 show their NIR-MIR and OPT photometries, respectively.

We finally cross-check our AGN classification with information from other wavelengths. The X-ray luminosities for the sources found in the X-ray catalogue of Krumpe et al. (2015) are consistent with our classification. We find only one X-ray source (F09-2) among the PAH galaxies. Its $0.5-7\text{ keV}$ luminosity is $\approx 8 \times 10^{40} \text{ erg s}^{-1}$ and can be accounted for by a pure star-forming activity. Among six bright AGN candidates, we find three (F00-3 = ANEPDCX0004, F10-20 = ANEPDCX0221, and F04-20 = ANEPDCX0138) X-ray sources. For the two such sources with measured redshifts, F00-3 and F10-20, their $0.5-7\text{ keV}$ luminosities ($\approx 2 \times 10^{43}$ and $\approx 5 \times 10^{42} \text{ erg s}^{-1}$, respectively) are in a range of typical Seyfert galaxies. The remaining three bright AGN candidates are outside of the X-ray survey area. Our AGN classification seems also valid when compared to the optical emission-line ratio diagnostics results of Shim et al. (2013). Four (out of all six) bright AGN candidates with the optical spectroscopy are classified as “TYPE1” AGNs. Figure 2 shows the SPICY spectrum of the brightest spectroscopically confirmed AGN, F05-1, at $z = 0.4508$ (quality flag = 4). This object indeed shows a featureless red continuum at $5-11.5\mu\text{m}$ as the NIR-MIR SED indicates (Fig. 12), followed by a pronounced decline in the spectrum around $11.5-13\mu\text{m}$, which is likely due to redshifted silicate $9.7\mu\text{m}$ absorption. We caution that this identification is tentative because the absorption peak is not seen within the wavelength coverage. If this is indeed due to silicate absorption, such characteristic MIR spectrum is typically found in type-2 AGNs (e.g. Hao et al. 2007). None of the 32 (out of all 48) PAH galaxies with optical spectroscopy (Sect. 2.3.2) are classified as AGNs.

3.2.2. Colour-redshift diagrams of the PAH galaxies

The colours of the SPICY PAH galaxies depend strongly on redshift in different ways for different colours. Figure 13 compares the flux ratios of $N3$ ($3.2\mu\text{m}$)/ $N2$ ($2.4\mu\text{m}$), $S7$ ($7.0\mu\text{m}$)/ $N3$ ($3.2\mu\text{m}$), $S11$ ($11.0\mu\text{m}$)/ $S7$ ($7.0\mu\text{m}$), and $L15$ ($15.0\mu\text{m}$)/ $S9W$ ($9.0\mu\text{m}$) as a function of redshift between the PAH galaxies and the SED templates. We again adopted the SWIRE SED templates of normal and star-forming galaxies; Sc, starburst (M 82), and LIRG (NGC 6090). We find very similar results as Takagi et al. (2010) and Hanami et al. (2012), who analyse colour-redshift diagrams for their NEP-Deep photometric sample up to larger

⁷ NGC 6090 is a strongly interacting LIRG (e.g. Scoville et al. 2000) with moderately strong starburst activity ($\log L_{\text{IR}} = 11.56(L_\odot)$; Sanders et al. 2003; after being converted to our assumed cosmology). The SED template of this galaxy is constructed by a physical starburst model GRASIL (Silva et al. 1998), and therefore a possible AGN contribution to this galaxy is not considered.

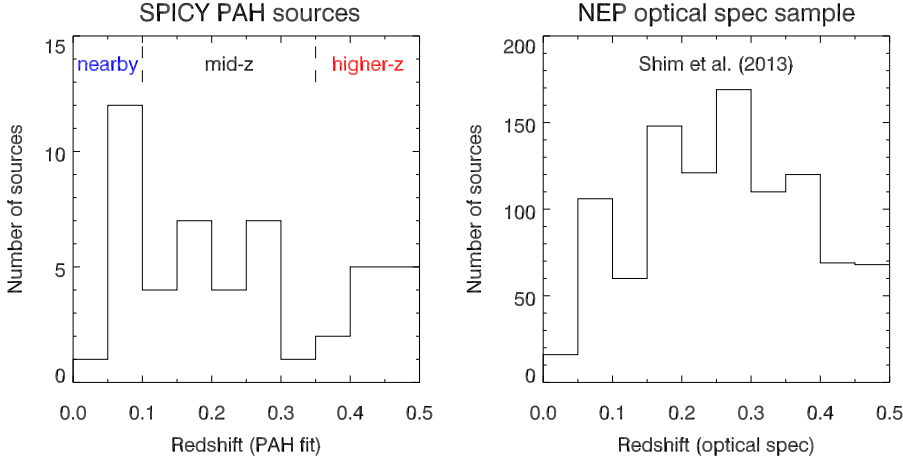


Fig. 9. Redshift distributions of the SPICY PAH galaxies (left) and the optical spectroscopic sample of Shim et al. (2013) towards the NEP (right). In the right panel, we only show the sources with good redshift measurements (quality flag of 3 or 4 in Shim et al. 2013; see text). We also indicate ranges of the three redshift bins; nearby (including 13 PAH galaxies), mid- z (23), and higher- z (12) bins, in the left panel.

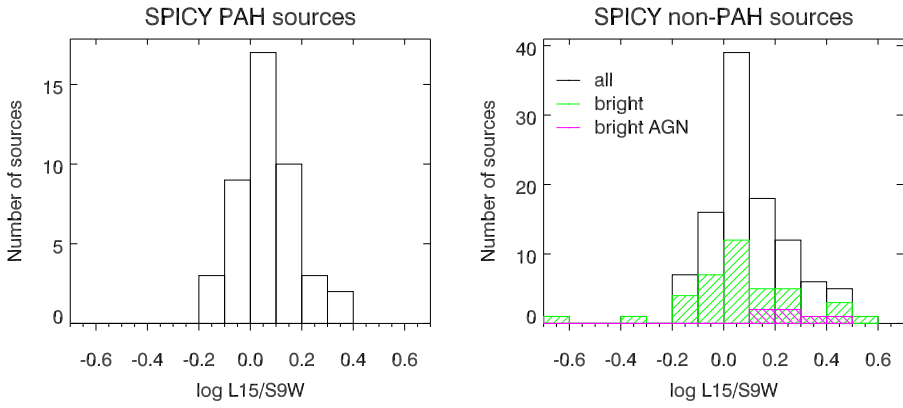


Fig. 10. Number distributions of the PAH (left panel) and non-PAH (right panel) sources as a function of $\log L15/S9W$ ($15.0\mu\text{m}/9.0\mu\text{m}$). In the right panel, number distributions of bright non-PAH sources and bright AGN candidates are also shown in green and magenta, respectively.

redshift ($z \sim 1-2$). In the NIR, both a stellar bump peaking at $1.6\mu\text{m}$ and stellar CO $v = 2-0$ absorptions with their band-head at $2.3\mu\text{m}$ affect the colours. The templates predict that the $N3/N2$ becomes smaller (bluer) with increasing redshift at $z \lesssim 0.2$, because the $2.3\mu\text{m}$ absorption feature moves from the $N2$ to $N3$ bands. The ratio then becomes larger (redder) with increasing redshift at $z \gtrsim 0.2$, because the $1.6\mu\text{m}$ feature moves from the $N2$ to $N3$ bands. The observations seem to follow such a colour trend at $z = 0.0-0.5$, although the overall change in this NIR colour is relatively small (by $\lesssim 0.2$ dex) in our redshift coverage ($z = 0.0-0.5$). In the MIR, because the prominent PAH features around $7.7\mu\text{m}$ move across the bands, the flux ratios show extreme diversity in the colour-redshift diagrams. The $S7/N3$ and $S11/S7$ become smaller (bluer) and larger (redder), respectively, with increasing redshift. In particular, the $S11/S7$ changes by as much as a factor of ten in our redshift coverage. This is primarily because the PAH $7.7\mu\text{m}$ moves from the $S7$ to $S11$ bands with increasing redshift. In contrast, the $L15/S9W$ shows little systematic change (by $\lesssim 0.2$ dex in our redshift coverage) with redshift. This is because the most prominent PAH $7.7\mu\text{m}$ is included within the $S9W$ band in most of our redshift coverage. The M82 SED template seems to show too much hot dust continuum at long side of the PAH $7.7\mu\text{m}$ to over-estimate the $L15/S9W$ in most of our redshift coverage (see also Sect. 3.4.1; Fig. 22).

3.2.3. Rest-frame SEDs of the PAH galaxies

We examine rest-frame SEDs of the SPICY PAH galaxies constructed by utilising 13 OPT-NIR-MIR broad-band photometric data and redshift from the PAH fit. As we show in the

following, the rest-frame SEDs have almost identical shapes for a range of redshift, making our analysis easier and probably more fundamental, in contrast to the observed-frame information that shows diversity. The observed photometric data were simply de-redshifted and normalised to the rest-frame $7.7\mu\text{m}$ and $3.5\mu\text{m}$ fluxes for the MIR- and NIR-normalised rest-frame SEDs, respectively (Fig. 14). Similar $3.5\mu\text{m}$ -normalised rest-frame SEDs are presented by Hanami et al. (2012) for their NEP-Deep photometric sample at $0.4 < z < 2$. The MIR normalisation wavelength is chosen at a peak of the PAH $7.7\mu\text{m}$, and flux there was estimated by simply interpolating fluxes of two filters that encompass the wavelength. The NIR normalisation wavelength is chosen as the longest wavelength within the stellar SED bump that the $N4$ band can cover even at $z > 0.35$. The $3.5\mu\text{m}$ flux was estimated by using linear interpolation or extrapolation among the three NIR bands in log wavelength-log flux space for sources at $z < 0.35$, because the stellar spectrum there can be approximated by a simple Rayleigh-Jeans power-law. The resultant SEDs indeed show such a power-law form at NIR in the rest frame. For sources at $z > 0.35$, we used only $N3$ and $N4$ bands for the interpolation, because the $N2$ band covers the peak of the stellar SED at $1.6\mu\text{m}$, and the Rayleigh-Jeans approximation is inappropriate there. We also constructed the median-averaged rest-frame SEDs by taking median values of normalised fluxes for each filter and redshift bin (Fig. 15). Missing flux data, if any, were ignored in taking the median.

The normalised rest-frame SEDs clearly illustrate their characteristic two-component shape. The MIR-normalised rest-frame SEDs are composed of the MIR bump ($5-10\mu\text{m}$, PAH peak) and the OPT-NIR one ($0.3-4\mu\text{m}$, red giant peak), with a clear dip around $\approx 4\mu\text{m}$ between the two bumps. We find that

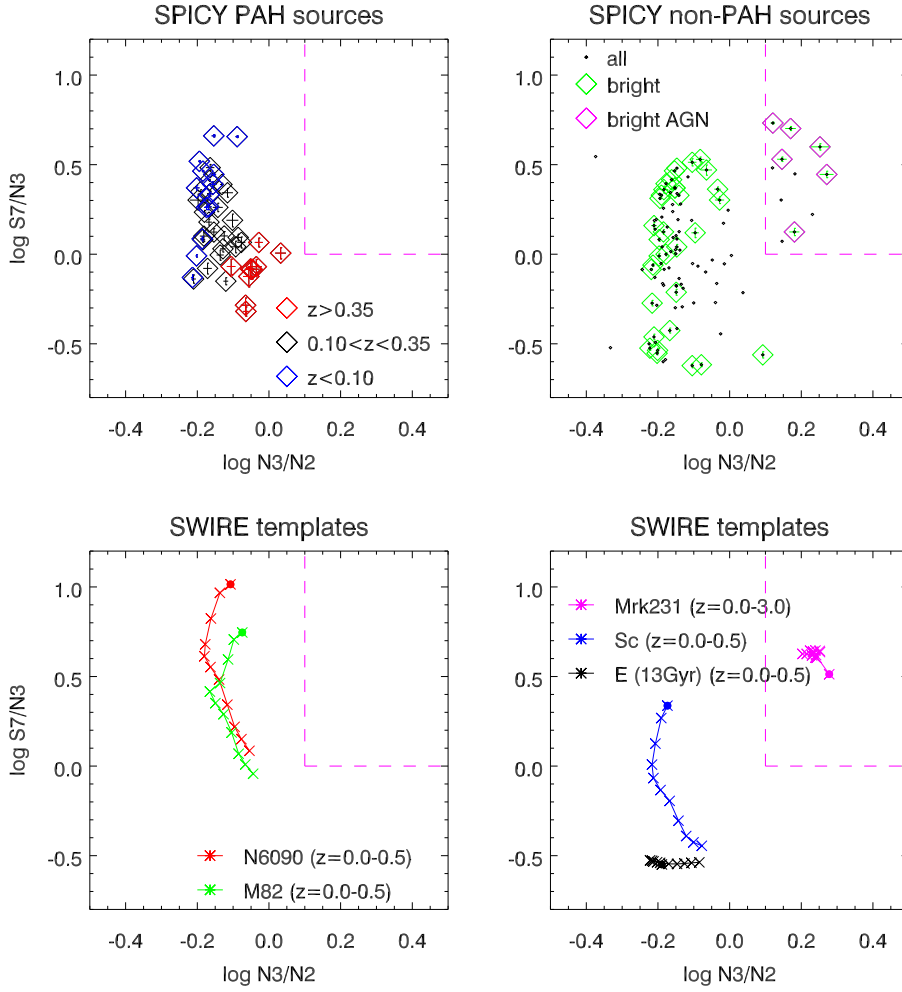


Fig. 11. Flux ratio diagrams of $\log N3$ ($3.2\mu\text{m}$)/ $N2$ ($2.4\mu\text{m}$) and $\log S7$ ($7.0\mu\text{m}$)/ $N3$ ($3.2\mu\text{m}$) of the SPICY sources. *Top left:* flux ratios of the PAH sources shown with one-sigma error bars in blue, black, and red diamonds for the nearby, mid- z , and higher- z sources, respectively. *Top right:* same diagram as the top left panel, but for non-PAH sources (black). Bright non-PAH sources are shown with one-sigma error bars and diamonds (green). For the faint non-PAH sources, error bars are omitted for clarity of the figure. *Bottom:* same diagrams as the top panels, but for redshifted SWIRE NGC 6090, M 82 (*left panel*), Sc, E (13 Gyr old), and AGN (Mrk 231) (*right panel*) templates with red, green, blue, black, and magenta connected crosses, respectively. The flux ratios of the AGN template are plotted at $z = 0.0-3.0$ in steps of 0.5, whereas those of other templates are plotted at $z = 0.0-0.5$ in steps of 0.05. The flux ratios of the templates at $z = 0.0$ are indicated by filled circles in both *bottom panels*. A space of the flux ratios to identify photometric AGN candidates (see text for the definition) is outlined by magenta dashed lines in all panels. Bright photometric AGN candidates are shown with magenta diamonds in the *top right panel*.

most sources have very similar MIR bump shape for a range of redshift, indicating that the PAH features look almost identical among the sources at this spectral resolution. In the meantime, the OPT–NIR bump becomes weaker with respect to the MIR one at higher redshifts. The NIR-normalised rest-frame SEDs clearly show that the OPT–NIR bump shape, particularly at NIR, is also almost identical among the sources for a range of redshift, showing a broad bump peaking at $\sim 1-2\mu\text{m}$ as expected for the stellar SEDs. Therefore, each of the SED bumps has its own shape with little systematic change as a function of redshift, and sources at higher redshifts show systematically more enhanced MIR bump with respect to the stellar SED.

3.3. Combined spectroscopic and photometric characteristics of the PAH galaxies

3.3.1. PAH luminosities

We compare the photometric and spectroscopic PAH luminosities of the SPICY PAH galaxies to test accuracy and robustness of our photometric measurement of the PAH luminosity, and to bridge the results from the PAH fit and the analysis based on the rest-frame SEDs. We already measured the spectroscopic PAH luminosities, $L_{\text{PAH}}(6.2\mu\text{m})$ and $L_{\text{PAH}}(7.7\mu\text{m})$, and spectroscopic monochromatic luminosity at $7.7\mu\text{m}$, $\nu L_{\nu \text{ spec}}(7.7\mu\text{m})$, in Sect. 2.3. In addition, we measured the photometric monochromatic luminosity at $7.7\mu\text{m}$, $\nu L_{\nu \text{ photo}}(7.7\mu\text{m})$ (hereafter, photometric monochromatic luminosity at $7.7\mu\text{m}$) while constructing the MIR-normalised rest-frame SEDs (Table C.8).

This photometric monochromatic luminosity includes contributions of the underlying continuum. Both the spectroscopic and photometric monochromatic luminosities at $7.7\mu\text{m}$ are intended to measure luminosities at the PAH $7.7\mu\text{m}$ peak by using the SPICY spectra and broad-band SEDs, respectively. Figure 16 compares the three kinds of the PAH $7.7\mu\text{m}$ luminosities, and shows good linear correlations among them, with a slope of unity. Their ratios show no dependence on redshift, indicating little systematics in the photometric measurement of the PAH peak fluxes, although the PAH $7.7\mu\text{m}$ is covered with different filters depending on redshift. The resultant scaling relations are: $\log \nu L_{\nu \text{ photo}}(7.7\mu\text{m}) = (0.60 \pm 0.16) + \log L_{\text{PAH}}(7.7\mu\text{m})$ ⁸ and $\log \nu L_{\nu \text{ photo}}(7.7\mu\text{m}) = (-0.28 \pm 0.09) + \log \nu L_{\nu \text{ spec}}(7.7\mu\text{m})$. Here, quoted uncertainties are for one-sigma scatter of the ratio between the luminosities. Such good correlations imply that our photometric measurement of the PAH feature provides a good estimate of the PAH luminosities.

We characterise the PAH luminosity of the SPICY PAH galaxies by comparing to a representative IRS sample in the

⁸ This rather large offset (0.60 ± 0.16 in log) is mostly due to different definitions of the two luminosities. For $\nu L_{\nu}(7.7\mu\text{m})$, we multiply the peak flux of the PAH $7.7\mu\text{m}$ profile (including the underlying continuum) by the peak frequency (corresponding to $7.7\mu\text{m}$ in wavelength). For $L_{\text{PAH}}(7.7\mu\text{m})$, we integrate under the PAH $7.7\mu\text{m}$ profile by using the best-fit Lorentzian function. This integration can be analytically made as $\pi \times (\text{amplitude of the PAH } 7.7\mu\text{m} \text{ profile}) \times (\text{HWHM of the profile; corresponding to } \approx 0.3\mu\text{m} \text{ in wavelength; Fig. 7})$. The former luminosity is, by definition, larger than the latter by a factor of $\approx \pi \times 0.3\mu\text{m}/7.7\mu\text{m}$ (plus a contribution of the continuum).

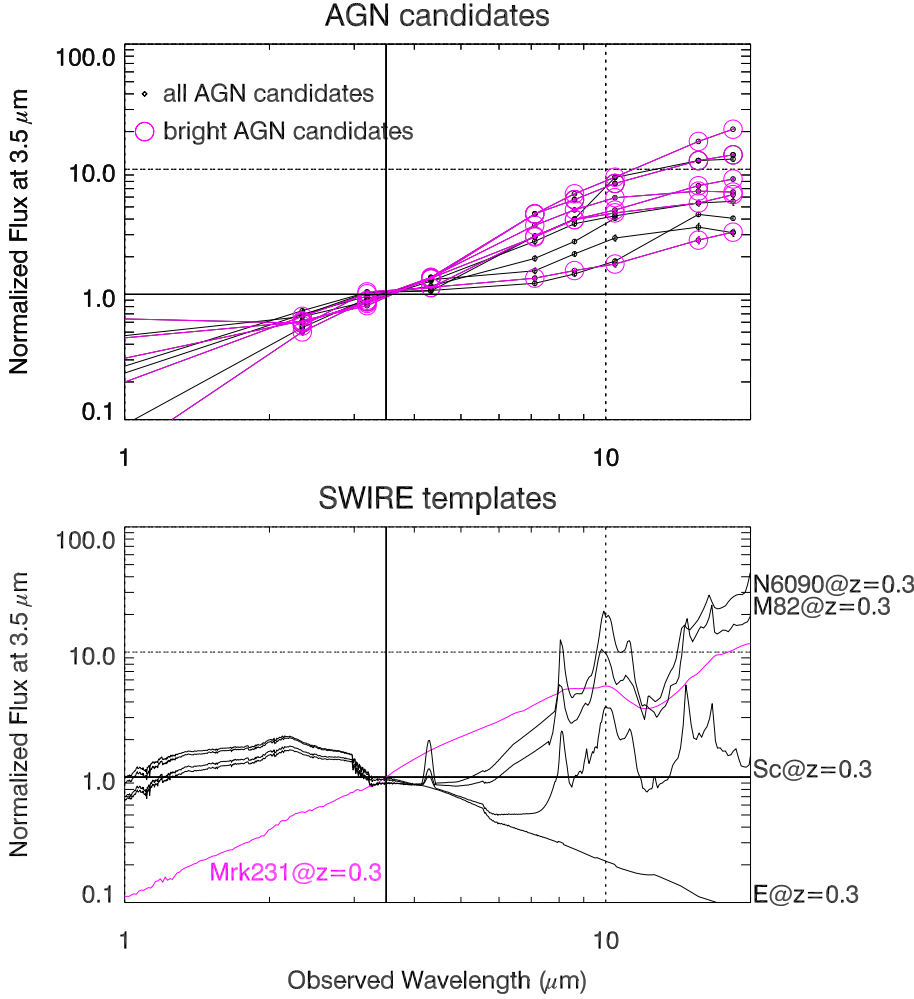


Fig. 12. Observed SEDs of the AGN candidates and comparison with various SED templates. *Top:* SEDs of the AGN candidates normalised at $3.5\mu\text{m}$. The bright AGN candidates are marked with magenta circles. *Bottom:* similarly normalised SWIRE SED templates of AGN (Mrk 231; magenta) and galaxies of E (13 Gyr old), Sc, M 82, and NGC 6090 (black) redshifted to $z = 0.3$. The normalisation wavelength is indicated by a black solid vertical line in each panel.

similar redshift range. Figure 17 compares the spectroscopic monochromatic luminosities at $7.7\mu\text{m}$ of the SPICY PAH galaxies and those of the star-forming galaxies observed with the IRS low-resolution mode in a sample of Weedman & Houck (2008). We neglected the effect of different spectroscopic resolutions between the IRS and IRC, because the PAH $7.7\mu\text{m}$ is intrinsically broad and resolved by both instruments. This IRS sample is a collection of wide variety of star-forming galaxies showing strong PAH features, including nearby bright ULIRGs, nearby starburst galaxies, MIPS $24\mu\text{m}$ -selected sources in the NOAO Boötes survey, the “First Look Survey”, and so on (see Weedman & Houck (2008) for the details of their sample). The SPICY PAH galaxies occupy near lower end of the $\nu L_{\nu\text{ spec}}$ ($7.7\mu\text{m}$) distribution of the IRS sample, meaning that the SPICY PAH galaxies are systematically less luminous for a given redshift.

We estimate the IR luminosities ($8\text{--}1000\mu\text{m}$; L_{IR}) of the SPICY PAH galaxies from the photometric monochromatic luminosities at $7.7\mu\text{m}$ by using a calibration from Takagi et al. (2010; see also Houck et al. 2007). We find that the PAH galaxies show $10 \lesssim \log L_{\text{IR}}(L_{\odot}) \lesssim 11.6$ (Fig. 18), and therefore have the luminosity of LIRGs ($11 < \log L_{\text{IR}}(L_{\odot}) < 12$) or less. We note that the NEP-Deep photometric samples at $z \gtrsim 1\text{--}2$ are typically more IR luminous with $\log L_{\text{IR}}(L_{\odot}) \gtrsim 12$ (Takagi et al. 2010; Hanami et al. 2012; see also Goto et al. 2010, 2011a). The inferred SFR by using the conversion between L_{IR} and SFR (Kennicutt 1998) is $\gtrsim 30 M_{\odot}\text{yr}^{-1}$ for luminous PAH galaxies at $z \gtrsim 0.35$.

3.3.2. SED shape variation and its interpretation with spectroscopy information

The normalised rest-frame SEDs of the SPICY PAH galaxies show a hint of systematic variation of the SED shape as a function of redshift (Sect. 3.2.3). We characterise the shape variation by comparing the photometric monochromatic luminosities and flux ratios measured at four wavelengths in the rest frame. We already measured the photometric monochromatic luminosities at $7.7\mu\text{m}$, $\nu L_{\nu\text{ photo}}$ ($7.7\mu\text{m}$), and $3.5\mu\text{m}$, $\nu L_{\nu\text{ photo}}$ ($3.5\mu\text{m}$), in constructing the MIR- and NIR-normalised rest-frame SEDs, respectively. In addition, we measured photometric monochromatic luminosities at $2.0\mu\text{m}$, $\nu L_{\nu\text{ photo}}$ ($2.0\mu\text{m}$), and $11.3\mu\text{m}$, $\nu L_{\nu\text{ photo}}$ ($11.3\mu\text{m}$). The wavelength of $2.0\mu\text{m}$ is the shortest wavelength that the NIR filters can cover even for the lowest redshift galaxies. The rest-frame $2.0\mu\text{m}$ flux was measured in the same way as the $3.5\mu\text{m}$ flux, but by using only the $N2$ ($2.4\mu\text{m}$) and $N3$ ($3.2\mu\text{m}$) bands for all sources. This is because the $2.0\mu\text{m}$ is close to the $1.6\mu\text{m}$ stellar SED peak, and we cannot assume a simple Rayleigh-Jeans approximation there. The wavelength of $11.3\mu\text{m}$ is to cover the PAH $11.3\mu\text{m}$ and dust continuum underneath. The rest-frame $11.3\mu\text{m}$ flux was measured in the same way as the $7.7\mu\text{m}$ flux, but with the $L15$ ($15.0\mu\text{m}$) and $L18W$ ($18.0\mu\text{m}$) bands at $z > 0.25$, and the $S11$ ($11.0\mu\text{m}$) and $L15$ ($15.0\mu\text{m}$) bands at $z < 0.25$. The rest-frame flux ratios of the $7.7\mu\text{m}$ flux to the $3.5\mu\text{m}$ flux, the $3.5\mu\text{m}$ flux to the $2.0\mu\text{m}$ flux, and the $11.3\mu\text{m}$ flux to the $7.7\mu\text{m}$ flux (hereafter, $F_{\text{rest } 7.7\mu\text{m}}/F_{\text{rest } 3.5\mu\text{m}}$,

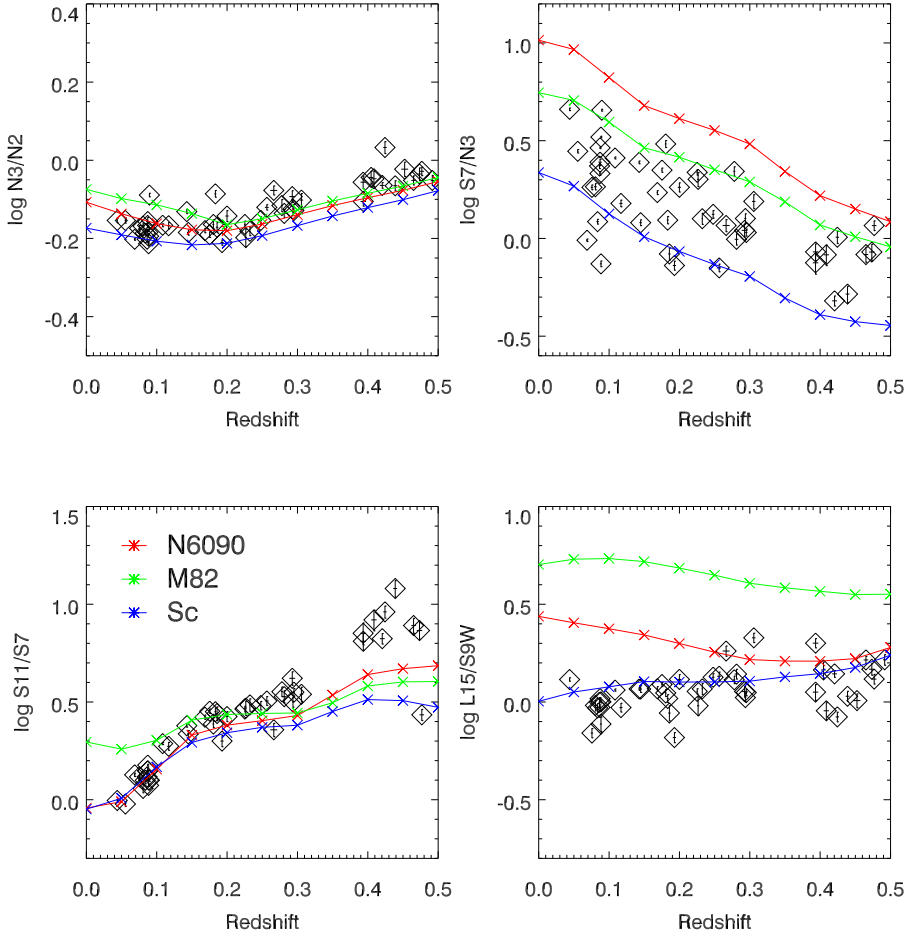


Fig. 13. NIR and MIR flux ratios of $N3$ ($3.2\mu\text{m}$)/ $N2$ ($2.4\mu\text{m}$), $S7$ ($7.0\mu\text{m}$)/ $N3$ ($3.2\mu\text{m}$), $S11$ ($11.0\mu\text{m}$)/ $S7$ ($7.0\mu\text{m}$), and $L15$ ($15.0\mu\text{m}$)/ $S9W$ ($9.0\mu\text{m}$) of the PAH galaxies as a function of redshift. Error bars are for one sigma. The flux ratios of the redshifted SWIRE SED templates of Sc (blue), M82 (green), and NGC 6090 (red) are overlaid with connected crosses. To enable easier visual comparison among the panels, the Y axis covers the same 1.8 dex-wide range in the flux ratios, excluding the panel of $N3/N2$ (covering half the range).

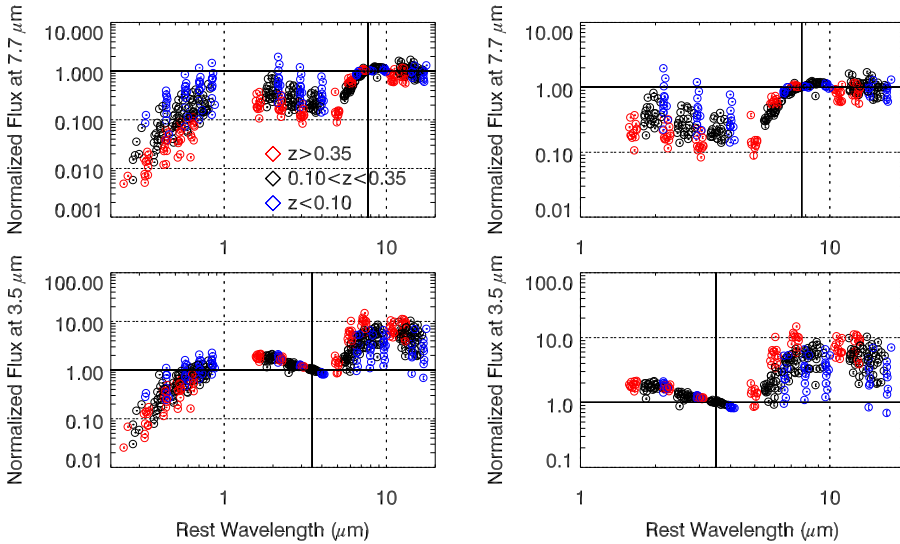


Fig. 14. Rest-frame SEDs of the PAH galaxies normalised at $7.7\mu\text{m}$ (MIR-normalised; *top*) and $3.5\mu\text{m}$ (NIR-normalised; *bottom*) with one-sigma error bars. The normalisation wavelengths are indicated by solid vertical lines in all panels. The *left* and *right* panels show the same SEDs but for the entire OPT-NIR-MIR and only the NIR-MIR wavelengths, respectively. The SEDs are shown in different colours for different redshift bins: blue, black, and red for the nearby, mid- z , and higher- z galaxies, respectively.

$F_{\text{rest } 3.5\mu\text{m}}/F_{\text{rest } 2.0\mu\text{m}}$, and $F_{\text{rest } 11.3\mu\text{m}}/F_{\text{rest } 7.7\mu\text{m}}$ ⁹, respectively) are then calculated. Table C.8 lists the luminosities and flux ratios of the PAH galaxies.

We find a significant systematic variation of relative strength of the MIR bump with respect to the OPT-NIR one at $z \gtrsim 0.35$. Figure 18 compares $\nu L_{\nu \text{ photo}}$ ($7.7\mu\text{m}$) and

⁹ Although $F_{\text{rest } 11.3\mu\text{m}}/F_{\text{rest } 7.7\mu\text{m}}$ and $S11$ ($11.0\mu\text{m}$)/ $S7$ ($7.0\mu\text{m}$) (Sect. 3.2.2) apparently look similar, they are quite different at $z > 0$. For example, $S11/S7$ is closer to $F_{\text{rest } 7.7\mu\text{m}}/F_{\text{rest } 3.5\mu\text{m}}$ at $0.35 < z < 0.5$.

$\nu L_{\nu \text{ photo}}$ ($3.5\mu\text{m}$), indicating that the slope of the correlation is not unity. In particular, we find a population showing stronger $\nu L_{\nu \text{ photo}}$ ($7.7\mu\text{m}$) with respect to $\nu L_{\nu \text{ photo}}$ ($3.5\mu\text{m}$) at $z > 0.35$ when compared to galaxies at $0.1 < z < 0.35$. We defined a PAH-enhanced population as a group of galaxies following $\log \nu L_{\nu \text{ photo}} (7.7\mu\text{m}) > 0.50 + \log \nu L_{\nu \text{ photo}} (3.5\mu\text{m})$ (or, equivalently, $F_{\text{rest } 7.7\mu\text{m}}/F_{\text{rest } 3.5\mu\text{m}} > 7.0$). We find ten PAH-enhanced galaxies in total, nine of which are at $z > 0.35$ (out of all 12 galaxies in this redshift range; Table 1). All three remaining PAH galaxies at $z \gtrsim 0.35$ are not

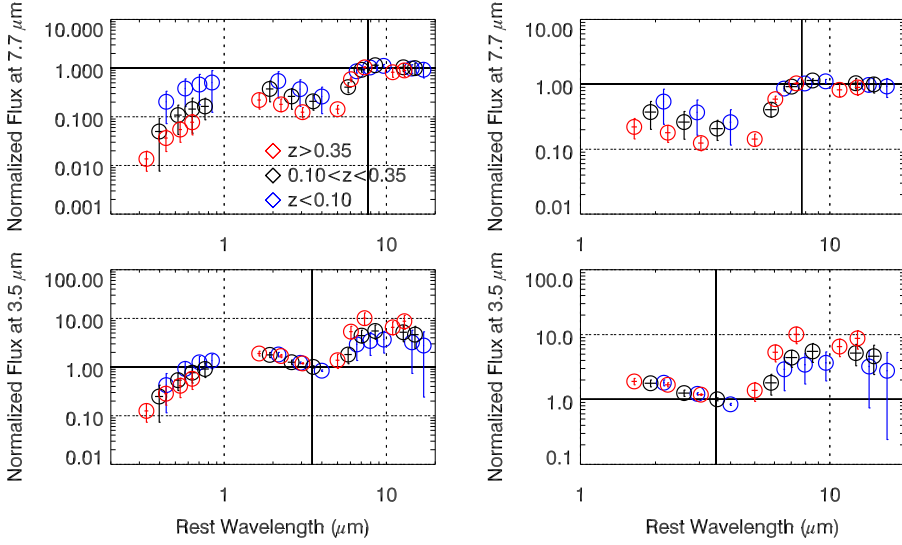


Fig. 15. Same SED plots as Fig. 14, but for median-averaged ones (see text). Error bars represent one-sigma scatter of the normalised photometric data along both the flux and wavelength directions around the medians.

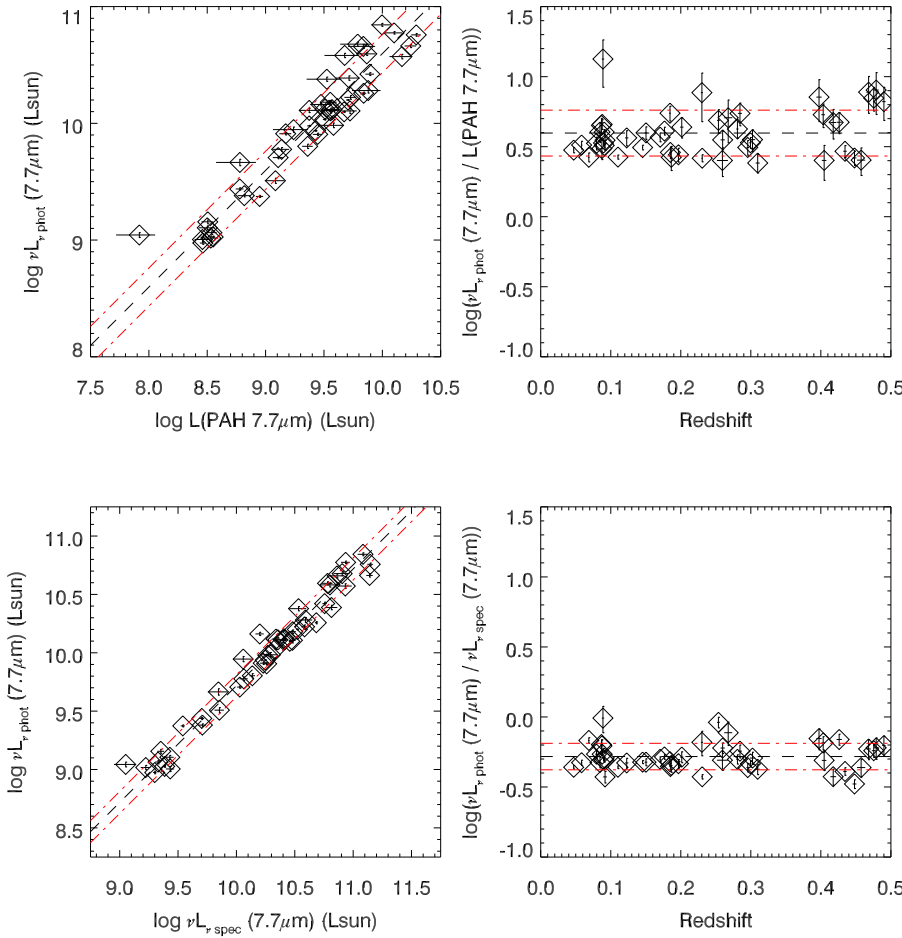


Fig. 16. Comparisons between the spectroscopic and photometric PAH 7.7 μm luminosities of the PAH galaxies. The photometric monochromatic luminosity at 7.7 μm , $\nu L_{\nu \text{ photo}} (7.7 \mu\text{m})$, is compared with the spectroscopic PAH 7.7 μm luminosity, $L_{\text{PAH}} (7.7 \mu\text{m})$ (*top*), and with the spectroscopic monochromatic luminosity at 7.7 μm , $\nu L_{\nu \text{ spec}} (7.7 \mu\text{m})$ (*bottom*). Their luminosity ratios are plotted as a function of redshift in the *right panels*. Error bars are for one sigma. In all panels, black broken lines represent the best-fit linear functions with fixed unity slopes, and red dot-dashed lines indicate the one-sigma scatters.

PAH-enhanced according to our definition, but they show modest PAH enhancement when compared to $z \sim 0$ SDSS main-sequence galaxies (Elbaz et al. 2007; Fig. 18). This figure also shows SFR inferred from $\nu L_{\nu \text{ photo}} (7.7 \mu\text{m})$ (Sect. 3.3.1) and stellar mass measured by using $\nu L_{\nu \text{ photo}} (3.5 \mu\text{m})$. Here, the stellar mass was measured by adopting the NGC 6090 SWIRE SED template, but this mass measurement is insensitive to types of galaxy SEDs adopted; the difference from the case with the M82 template is 0.12 dex. Thus, the trend of the relative enhancement of $\nu L_{\nu \text{ photo}} (7.7 \mu\text{m})$ over $\nu L_{\nu \text{ photo}} (3.5 \mu\text{m})$ can be

interpreted that SFR becomes larger with respect to the stellar mass at higher redshifts, particularly for the PAH-enhanced population at $z \gtrsim 0.35$ (see Sect. 4.1.1 for more discussions). Similarly, Fig. 19 shows that $F_{\text{rest } 7.7 \mu\text{m}} / F_{\text{rest } 3.5 \mu\text{m}}$ increases as both PAH 7.7 μm and 6.2 μm luminosities increase. This suggests that the relative strength of the MIR bump is controlled by the PAH luminosity, and that SFR per unit stellar mass (specific SFR or sSFR) becomes larger with SFR.

We further explore the SED shape variations of the PAH galaxies by using other rest-frame flux ratios. The

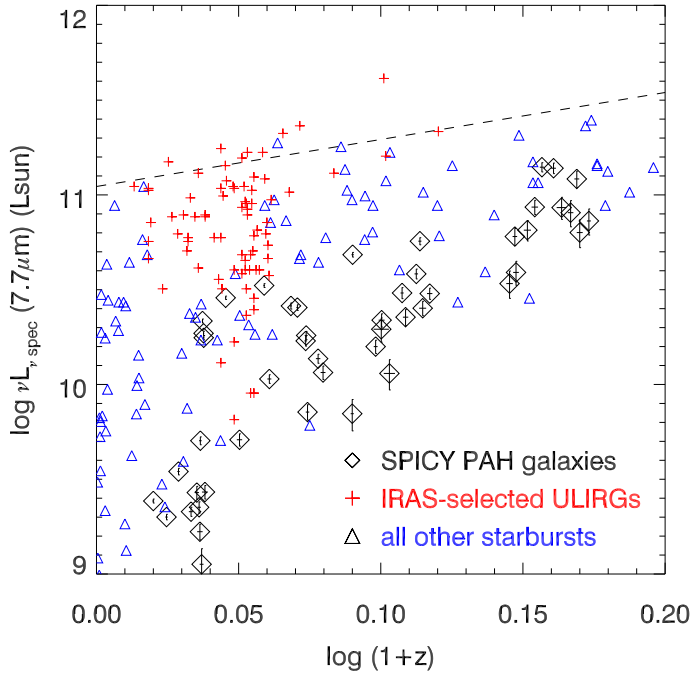


Fig. 17. Spectroscopic monochromatic luminosities at $7.7\mu\text{m}$, $\nu L_{\nu, \text{spec}} (7.7\mu\text{m})$, as a function of redshift. The SPICY PAH galaxies are shown with black diamonds with one-sigma error bars, and the IRS galaxies in a sample of Weedman & Houck (2008) are shown with red pluses and blue triangles for starburst-component of the IRAS-selected ULIRGs and all other starburst galaxies, respectively. A black broken line represents a limit of “maximum starburst” of Weedman & Houck (2008) fitted at $z = 0.0\text{--}2.5$.

$F_{\text{rest } 3.5\mu\text{m}}/F_{\text{rest } 2.0\mu\text{m}}$ ratio corresponds to slope of the stellar SED bump at its longer side of its peak ($1.6\mu\text{m}$), if the stellar SED dominates at NIR. The $F_{\text{rest } 11.3\mu\text{m}}/F_{\text{rest } 7.7\mu\text{m}}$ ratio is a flux ratio at two peaks of the PAH $11.3\mu\text{m}$ and $7.7\mu\text{m}$ features, although the ratio can be modified by either hot dust continuum underneath the PAH features, silicate absorption around $9.7\mu\text{m}$, or red AGN continuum (Sect. 4.1.2 for more discussion). Figure 20 shows the redshift dependence of these two rest-frame line ratios as well as $F_{\text{rest } 7.7\mu\text{m}}/F_{\text{rest } 3.5\mu\text{m}}$. Figure 21 shows correlations among these three flux ratios. As we saw earlier, the $F_{\text{rest } 7.7\mu\text{m}}/F_{\text{rest } 3.5\mu\text{m}}$ ratio shows enhancement at $z \gtrsim 0.35$ constituting the PAH-enhanced population, whereas it shows significant scatter for a given redshift at $z \lesssim 0.35$. In the meantime, the $F_{\text{rest } 11.3\mu\text{m}}/F_{\text{rest } 7.7\mu\text{m}}$ ratio is almost constant at $z \lesssim 0.35$, and it decreases by a factor of $\lesssim 2$ at $z \gtrsim 0.35$ while $F_{\text{rest } 7.7\mu\text{m}}/F_{\text{rest } 3.5\mu\text{m}}$ increases by a factor of ~ 2 . In contrast, the $F_{\text{rest } 3.5\mu\text{m}}/F_{\text{rest } 2.0\mu\text{m}}$ ratio shows only a small variation with redshift.

We examine possible selection bias on the observed systematic SED variation caused by using the $S9W$ ($9.0\mu\text{m}$) filter for the source detection. The most prominent PAH $7.7\mu\text{m}$ feature is fully covered with the $S9W$ filter up to $z \simeq 0.35$, and its red part goes out of the filter bandpass at $0.35 \lesssim z \lesssim 0.5$ although its peak is still included within the filter. This leads to the selection bias of preferentially detecting the PAH-bright sources at $0.35 \lesssim z \lesssim 0.5$, meaning that PAH-enhanced but PAH-faint population would be missed in our sample. In contrast, PAH-less-enhanced but PAH-bright population (e.g. massive Sa–Sc galaxies) can be detected with the $S9W$ filter, and lack of such population (Figs. 14, 18) indicates that they are indeed rare. At $z \lesssim 0.35$, both galaxies with and without the PAH

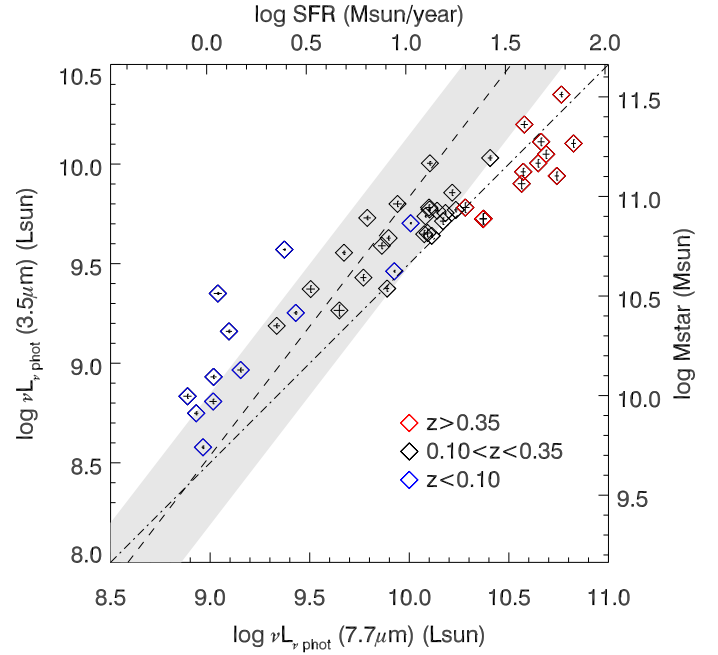


Fig. 18. Comparison between the photometric monochromatic luminosities at $7.7\mu\text{m}$, $\nu L_{\nu, \text{photo}} (7.7\mu\text{m})$, and at $3.5\mu\text{m}$, $\nu L_{\nu, \text{photo}} (3.5\mu\text{m})$. The PAH galaxies are shown with one-sigma error bars in different colours for different redshift bins: blue, black, and red for the nearby, mid- z , and higher- z galaxies, respectively. SFR and stellar mass are estimated from $\nu L_{\nu, \text{photo}} (7.7\mu\text{m})$ and $\nu L_{\nu, \text{photo}} (3.5\mu\text{m})$, respectively, as explained in the text. A correlation between stellar mass and SFR for main sequence galaxies for $z \sim 0$ SDSS sample (Elbaz et al. 2007) is indicated by a grey hatched area, showing one-sigma scatter around the best fit line (broken line). A diagonal dot-broken line for a fixed PAH-to-stellar luminosity ratio ($\log \nu L_{\nu, \text{photo}} (7.7\mu\text{m}) = 0.50 + \log \nu L_{\nu, \text{photo}} (3.5\mu\text{m})$) is used to identify the PAH-enhanced population (on the lower right side of this line).

enhancement can be detected, because they are brighter in the $S9W$ filter due to their proximity and better coverage of the PAH $7.7\mu\text{m}$ profile within its bandpass. This indicates that lack of the PAH-enhanced population at $z \lesssim 0.35$ is not due to the selection bias. Therefore, it is safe to conclude that the PAH-enhanced population emerges at $z > 0.35$ and dominates among the vigorous star-forming populations showing high PAH luminosity. Another trend of systematically depressed $F_{\text{rest } 11.3\mu\text{m}}/F_{\text{rest } 7.7\mu\text{m}}$ for galaxies with enhanced $F_{\text{rest } 7.7\mu\text{m}}/F_{\text{rest } 3.5\mu\text{m}}$ at $z \gtrsim 0.35$ seems not due to any selection biases. This is because the $L15$ ($15.0\mu\text{m}$) band that covers the rest-frame $11.3\mu\text{m}$ at $z \gtrsim 0.35$ is not considered for source selection.

There remains a question if the apparent emergence of the PAH-enhanced population at $z \gtrsim 0.35$ is statistically significant or by chance due to small number statistic. We tested if the observed relative fractions of the PAH-enhanced population in the higher- z and mid- z redshift bins are statistically significantly different from each other. We find one and nine PAH-enhanced galaxies out of all 23 and 12 galaxies in the mid- z and higher- z bins, respectively (Table 1). We performed Fisher’s exact test¹⁰ to calculate the total probability of the observed numbers of the PAH-enhanced population, given the sample size, being as extreme or more extreme if the null hypothesis (expectations of

¹⁰ This is an exact test of independence of two nominal variables, and works even on small samples. We used a “fisher.exact” function in the “stats” package of the “R” language.

the fractions of the PAH-enhanced population in both redshift bins are the same) is true. We find $p = 2.8 \times 10^{-5}$ (p : probability that one expects the result being the same as, or more extreme than, the actual observed result when the null hypothesis is true), meaning that this null hypothesis is rejected at >99% significance level. Therefore, we conclude that the PAH-enhanced population indeed emerges at $z \gtrsim 0.35$, although analysis with larger sample size and more fair sampling at $z \gtrsim 0.35$ is preferred to confirm this conclusion.

3.4. Template and model SED fit to the rest-frame SEDs of the PAH galaxies

In an attempt to understand the typical SED shape of the PAH galaxies and its systematic variation as demonstrated so far, we compare the observed rest-frame SEDs with the SEDs of templates and models of known characteristics. We again adopted the SED templates of Sc, starburst (M82), and LIRG (NGC 6090) from the SWIRE SED library. In addition, we adopted SEDs of a physical starburst model SBURT (Takagi et al. 2003a) to gain insight into the physical parameters of star formation. The SBURT models have been tested for ultraviolet-selected starbursts and ULIRGs (Takagi et al. 2003a,b), and applied to, for example, the sub-millimetre galaxies (e.g. Takagi et al. 2004) and NEP-Deep photometric samples (e.g. Takagi et al. 2007, 2010). We fitted the averaged SEDs and their systematic variation, rather than fitting SEDs of individual galaxies. In order to make fair and direct comparisons between the SEDs of the templates and the models, and ones of the observations, we considered smoothing of the spectral features due to our filter bandpasses. We simulated observations of redshifted templates and model galaxies, by redshifting their SEDs and calculating in-band fluxes through the IRC filters, to make a synthetic photometric catalogue. Then the rest-frame SEDs were reconstructed from this synthetic catalogue, and the flux ratios of $F_{\text{rest } 3.5\mu\text{m}}/F_{\text{rest } 2.0\mu\text{m}}$, $F_{\text{rest } 7.7\mu\text{m}}/F_{\text{rest } 3.5\mu\text{m}}$, and $F_{\text{rest } 11.3\mu\text{m}}/F_{\text{rest } 7.7\mu\text{m}}$ were calculated by following exactly the same procedure as for the real observations.

Before comparing with the observations, we verify our method of photometrically measuring the SED shape by using the synthetic catalogue of the template and model SEDs. The reconstructed rest-frame flux ratios from the synthetic catalogue should not change as a function of redshift, although this is not the case in reality. This is because the spectral resolution of the IRC photometry ($R \approx 5$) is not high enough to properly sample complicated rich PAH features, and different filters with different spectral resolutions are used to sample such features depending on the redshift. We find that the synthetic flux ratios change by ~ 0.2 dex in our redshift coverage ($z = 0.0\text{--}0.5$; e.g. Fig. 20), indicating that our analysis methods are reliable within ~ 0.2 dex.

3.4.1. Comparison with the SWIRE SED templates

We compare the observations of the PAH galaxies and the SWIRE SED templates by using the three rest-frame flux ratios (Figs. 20, 21) and in a form of SEDs (Fig. 22). To reproduce the observed range of $F_{\text{rest } 7.7\mu\text{m}}/F_{\text{rest } 3.5\mu\text{m}}$ at $z \lesssim 0.35$ (2–7), a range of template types between Sc and starburst is needed. The E and Sa templates show too small $F_{\text{rest } 7.7\mu\text{m}}/F_{\text{rest } 3.5\mu\text{m}}$ (~ 1). The larger observed $F_{\text{rest } 7.7\mu\text{m}}/F_{\text{rest } 3.5\mu\text{m}}$ at $z \gtrsim 0.35$ (7–14) can be reproduced by the LIRG template, although the depressed $F_{\text{rest } 11.3\mu\text{m}}/F_{\text{rest } 7.7\mu\text{m}}$ cannot be reproduced at the same time. The starburst template predicts too large $F_{\text{rest } 11.3\mu\text{m}}/F_{\text{rest } 7.7\mu\text{m}}$

ratio in our redshift coverage due to too steep increase of the red continuum at $>10\mu\text{m}$ (Fig. 22). The NIR flux ratio of $F_{\text{rest } 3.5\mu\text{m}}/F_{\text{rest } 2.0\mu\text{m}}$ can be reproduced by all Sc, starburst, and LIRG templates.

3.4.2. Comparison with the SBURT models

The SBURT model is a simple physical starburst model, in which a star cluster evolves and radiative transfer of the cluster light through dusty medium is solved to predict the observed SED (see Takagi et al. 2003a for full details). Input parameters of the model are dust composition, age of the starburst (t_{burst}), and the compactness parameter of the star cluster radial distribution (Θ : the mean stellar density becomes higher for smaller Θ). For simplicity, we fixed dust composition the Milky-Way type, which produces the most enhanced PAH emission due to larger PAH fraction among three possible choices available within the SBURT, and is suited to fit the PAH-enhanced population. A starburst happens at the central star cluster following the gas supply from a galactic infall, and the SFR increases until $t_{\text{burst}} = 100$ Myr, which equals to the time scale of the infall¹¹. Both PAH features and hot dust continuum are enhanced as SFR increases due to increased number of UV photons from young stars. In the meantime, the stellar mass accumulates as the star formation continues, and the stellar continuum emission at NIR increases with t_{burst} . Therefore, the $F_{\text{rest } 7.7\mu\text{m}}/F_{\text{rest } 3.5\mu\text{m}}$ ratio is larger at $t_{\text{burst}} \approx 100$ Myr, and it becomes smaller at $t_{\text{burst}} > 100$ Myr. The optical depth, which is calculated based on amount of the gas for star formation and the cluster compactness, is larger in more compact (smaller Θ) star cluster. The OPT-NIR colours are redder and $F_{\text{rest } 7.7\mu\text{m}}/F_{\text{rest } 3.5\mu\text{m}}$ is larger with larger optical depth. The younger starburst ($t_{\text{burst}} < 100$ Myr) shows larger $F_{\text{rest } 3.5\mu\text{m}}/F_{\text{rest } 2.0\mu\text{m}}$ due to enhanced hot dust continuum that contributes to even the $3.5\mu\text{m}$ flux. In contrast, the $F_{\text{rest } 11.3\mu\text{m}}/F_{\text{rest } 7.7\mu\text{m}}$ ratio changes only a little over a wide range of the input parameters. This is because no mechanism of changing PAH inter-band flux ratios is implemented in the model, and change of the dust continuum underneath the PAH features does not affect the flux ratio very much due to the small wavelength separation.

In order to reproduce galaxies with moderately enhanced PAH emission ($F_{\text{rest } 7.7\mu\text{m}}/F_{\text{rest } 3.5\mu\text{m}} \approx 7\text{--}10$) while keeping the constraint of the NIR colour ($F_{\text{rest } 3.5\mu\text{m}}/F_{\text{rest } 2.0\mu\text{m}}$), one needs middle-aged ($t_{\text{burst}} = 200$ Myr) starburst with larger compactness parameter ($\Theta \approx 5.0$; Figs. 20, 21, 22). In order to reproduce galaxies with less-enhanced PAH emission ($F_{\text{rest } 7.7\mu\text{m}}/F_{\text{rest } 3.5\mu\text{m}} \lesssim 7$), one needs older starbursts with larger compactness parameter ($t_{\text{burst}} > 200$ Myr, $\Theta \approx 5.0$). Such starburst can explain the wide range of $F_{\text{rest } 7.7\mu\text{m}}/F_{\text{rest } 3.5\mu\text{m}}$ as a function of the burst age, while keeping the NIR colour. In order to reproduce galaxies with more enhanced PAH emission ($F_{\text{rest } 7.7\mu\text{m}}/F_{\text{rest } 3.5\mu\text{m}} \approx 14$), one needs a younger starburst ($t_{\text{burst}} < 200$ Myr) or a starburst with smaller Θ (≈ 2). Although the NIR SED is almost insensitive to the burst age and optical depth, such starburst fails to reproduce the NIR colour due to non-negligible hot dust continuum contribution at $3.5\mu\text{m}$ or too large optical depth for reddening even at NIR. The OPT SEDs provide an independent constraint on the SBURT models. This is because all these SBURT models predict blue OPT SEDs due to young and blue stars in the star clusters, whereas the OPT SEDs are typically as red as those of very old populations (Fig. 22).

¹¹ An absolute age of 100 Myr here and in the following is a model parameter that can be selected from outside (Takagi et al. 2003a).

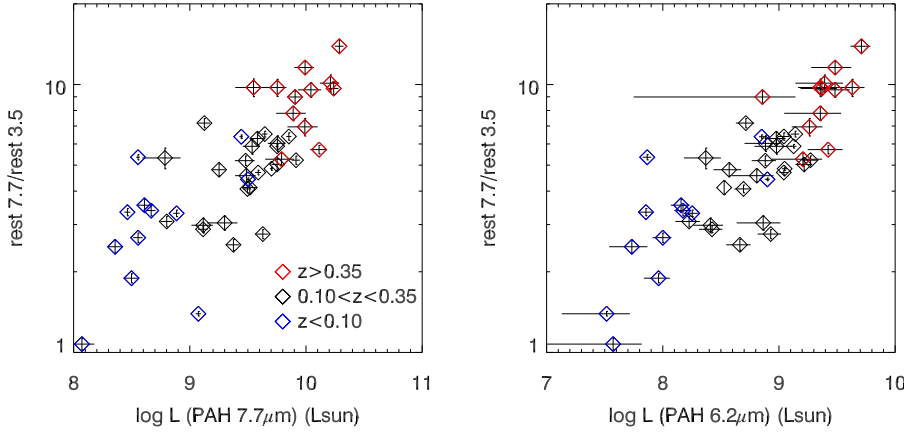


Fig. 19. Correlations between $F_{\text{rest } 7.7 \mu\text{m}}/F_{\text{rest } 3.5 \mu\text{m}}$ and the spectroscopic luminosities of the PAH 7.7 μm , $L_{\text{PAH}} (7.7 \mu\text{m})$ (left), and PAH 6.2 μm , $L_{\text{PAH}} (6.2 \mu\text{m})$ (right). The PAH galaxies are shown with one-sigma error bars in different colours for different redshift bins: blue, black, and red for the nearby, mid- z , and higher- z galaxies, respectively.

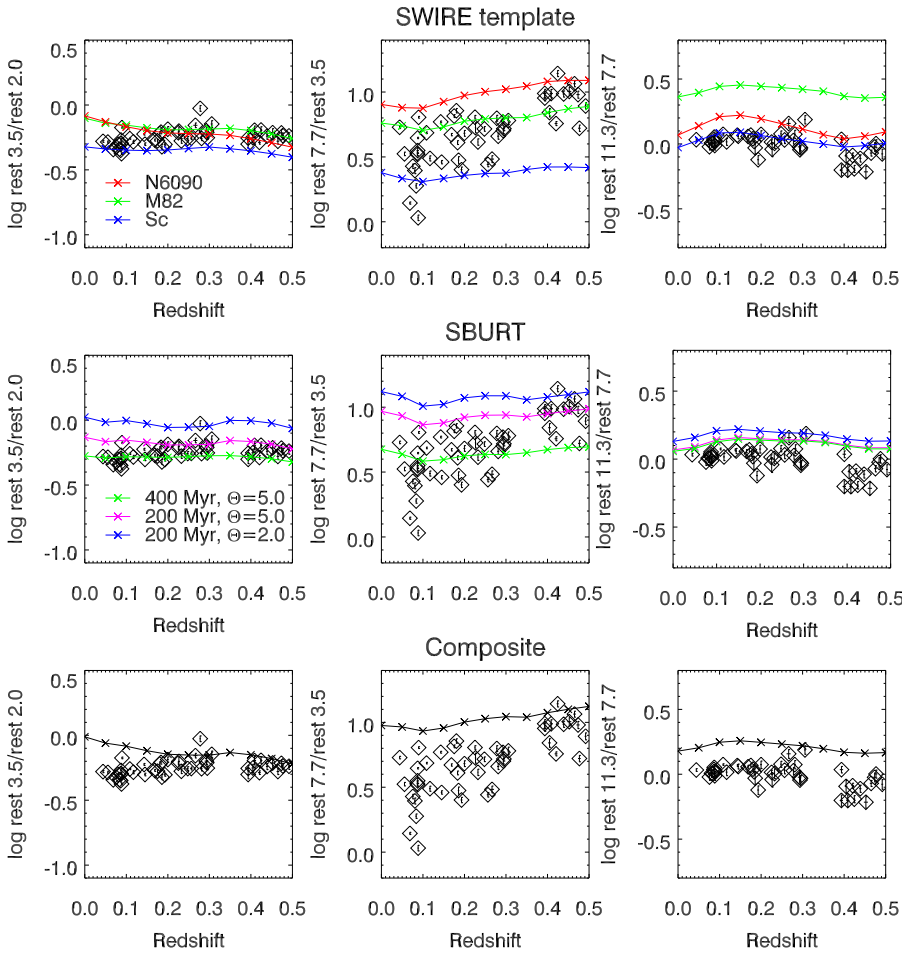


Fig. 20. Rest-frame flux ratios of $F_{\text{rest } 3.5 \mu\text{m}}/F_{\text{rest } 2.0 \mu\text{m}}$ (left), $F_{\text{rest } 7.7 \mu\text{m}}/F_{\text{rest } 3.5 \mu\text{m}}$ (middle), and $F_{\text{rest } 11.3 \mu\text{m}}/F_{\text{rest } 7.7 \mu\text{m}}$ (right) as a function of redshift. The flux ratios of the PAH galaxies are shown with diamonds with one-sigma error bars, and ones of the templates and the models are shown with connected crosses. To enable easier visual comparison among the panels, all three kinds of the panels cover the same 1.6 dex-wide range in the flux ratios. *Top:* SWIRE SED templates of Sc (blue), M82 (green), and NGC 6090 (red). *Middle:* SBURT models of $(t_{\text{burst}}, \Theta) = (400 \text{ Myr}, 5.0)$, $(200 \text{ Myr}, 5.0)$, and $(200 \text{ Myr}, 2.0)$ in green, magenta, and blue, respectively. *Bottom:* composite model. We caution that small changes of the flux ratios of the templates and the models are not to predict real changes of the ratios as a function of redshift, but to demonstrate an accuracy of our analysis method (Sect. 3.4).

If the observed range of $F_{\text{rest } 7.7 \mu\text{m}}/F_{\text{rest } 3.5 \mu\text{m}}$ is due to a range of the burst age, the OPT SEDs also change accordingly, unless the optical depth is also adjusted to compensate the effect of the burst age.

3.4.3. Comparison with the burst-on-old composite models

We have shown above that SBURT models for reproducing pronounced PAH bump cannot consistently reproduce the OPT-NIR-MIR SEDs. This is particularly true for the PAH-enhanced population at $z \gtrsim 0.35$: one needs a starburst that shows nearly maximum $F_{\text{rest } 7.7 \mu\text{m}}/F_{\text{rest } 3.5 \mu\text{m}}$ to enhance the PAH bump as observed, but such starburst inevitably predicts much bluer

OPT SEDs than the observations. To solve this problem, we explore two-component composite models that combine very young ($t_{\text{burst}} \lesssim 100 \text{ Myr}$) and old ($\approx 10 \text{ Gyr}$) populations for the PAH-enhanced population. If the very old component with relatively red OPT SED dominates the OPT-NIR SED, and the very young starburst with strong PAH emission dominates the MIR SED, we may be able to enhance the PAH bump for a given OPT-NIR SED by increasing the relative flux contribution of the starburst component. To also reproduce the observed narrow NIR colour range, however, the very young component must be highly reddened not to significantly contribute to the 3.5 μm flux. A very young starburst with small compactness parameter can be very optically thick, and seems appropriate for

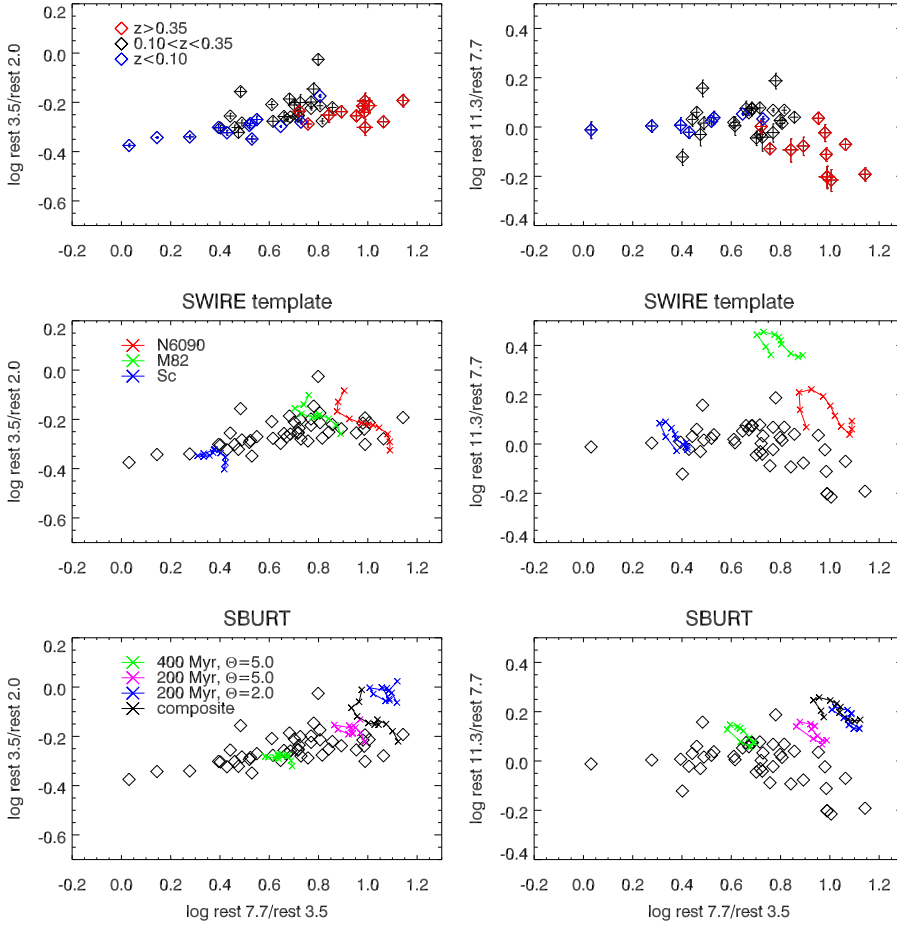


Fig. 21. Rest-frame flux ratio diagrams between $F_{\text{rest } 7.7 \mu\text{m}}/F_{\text{rest } 3.5 \mu\text{m}}$ and $F_{\text{rest } 3.5 \mu\text{m}}/F_{\text{rest } 2.0 \mu\text{m}}$ (left) and between $F_{\text{rest } 7.7 \mu\text{m}}/F_{\text{rest } 3.5 \mu\text{m}}$ and $F_{\text{rest } 11.3 \mu\text{m}}/F_{\text{rest } 7.7 \mu\text{m}}$ (right). The flux ratios of the observations are shown with diamonds, and ones of the templates and the models are shown with connected crosses. *Top*: PAH galaxies in the nearby, mid- z , and higher- z redshift bins in blue, black, and red, respectively, with one-sigma error bars. *Middle*: SWIRE SED templates of Sc (blue), M82 (green), and NGC 6090 (magenta) at $z = 0.0$ – 0.5 in steps of 0.05. *Bottom*: SBURT models of $(t_{\text{burst}}, \Theta) = (400 \text{ Myr}, 5.0)$, $(200 \text{ Myr}, 5.0)$, and $(200 \text{ Myr}, 2.0)$, and the composite model in green, magenta, blue, and black, respectively. We caution that small changes of the flux ratios of the templates and the models are not to predict real changes of the ratios as a function of redshift, but to demonstrate an accuracy of our analysis method (Sect. 3.4).

the composite. Figure 22 shows one example of such composite models, in which an E (13 Gyr old) SWIRE template is combined with a very young ($t_{\text{burst}} = 70 \text{ Myr}$), compact ($\Theta = 1.0$), and thus optically very thick ($\tau(V) \simeq 16.5$) SBURT model. The parameters of this composite model (t_{burst} and Θ of the young starburst, and the relative flux contribution of the young starburst with respect to the old population) were found so that the composite SED reproduces the typical rest-frame colours of the PAH-enhanced population ($\log F_{\text{rest } 7.7 \mu\text{m}}/F_{\text{rest } 3.5 \mu\text{m}} \geq 1.1$ and $-0.3 \leq \log F_{\text{rest } 3.5 \mu\text{m}}/F_{\text{rest } 2.0 \mu\text{m}} \leq -0.2$; see Fig. 20). We here focused on these two rest-frame NIR and MIR colours because they best characterise the NIR–MIR SED of the PAH galaxies (Sect. 3.3.2), and the OPT SED is not sensitive to the parameters of this burst-on-old composite. We caution that very similar composite SEDs can be constructed with different mixtures of populations with slightly different parameters. For example, the $F_{\text{rest } 7.7 \mu\text{m}}/F_{\text{rest } 3.5 \mu\text{m}}$ ratio of the very young component changes with the burst age, but the ratio of the composite SED can be unchanged if their relative flux contribution is adjusted.

This composite SED better reproduces the PAH-enhanced population than any single-component SBURT models (Figs. 20–22). We note that the SWIRE SED template of NGC 6090, which fits the SEDs of the PAH-enhanced population in all OPT–NIR–MIR wavelengths (Fig. 22; Sect. 3.4.1), resembles this composite SED very much. We caution that, although this composite model can reproduce the most representative characteristics of the observe SEDs of the PAH-enhanced population, as well as the SFR–sSFR correlation among the PAH galaxies in general (Sect. 4.1.1), we cannot confirm if these galaxies are indeed made of this kind of composite. In particular, the presence of the highly absorbed starburst cannot

be confirmed based on our spectral analysis (Sect. 2.3.2). A weakness of the composite model is that it still cannot reproduce the relatively depressed $F_{\text{rest } 11.3 \mu\text{m}}/F_{\text{rest } 7.7 \mu\text{m}}$ for the PAH-enhanced population at $z \gtrsim 0.35$, for the same reason as for the single-component SBURT models (Sect. 3.4.2)¹².

4. Discussion

4.1. PAH-enhanced population

4.1.1. Star formation rate and specific star formation rate

We find that the PAH-enhanced population at $z \gtrsim 0.35$ shows vigorous star formation. Their PAH luminosity ($\log \nu L_{\nu \text{ photo}}(7.7 \mu\text{m})(L_{\odot}) > 10.3$) corresponds to $\log L_{\text{IR}}(L_{\odot}) > 11.0$, or $\text{SFR} \gtrsim 30 M_{\odot} \text{ yr}^{-1}$, and they are in a class of LIRGs (Sect. 3.3.1). This population seems to emerge at $z \gtrsim 0.35$. As we noted earlier (Sect. 3.3.2), the selection bias caused by the source detection with the S9W (9.0 μm) filter cannot explain this trend. Also, the difference in the fractions of the PAH-enhanced population between the mid- z and higher- z redshift bins looks statistically significant. We further note that the survey volume is smaller by a factor of about two in $0.2 < z < 0.35$ than in $0.35 < z < 0.5$ for the same sky coverage and the same redshift interval of $dz = 0.15$, causing detecting a rare population

¹² This composite SED actually shows slightly larger $F_{\text{rest } 11.3 \mu\text{m}}/F_{\text{rest } 7.7 \mu\text{m}}$ than the SBURT model of $t_{\text{burst}} = 200 \text{ Myr}$, $\Theta \simeq 5.0$ that can well describe the NIR–MIR SED of the PAH-enhanced population (Figs. 20–22). This is because the very young component in the composite model adds the 11.3 μm flux due to more pronounced red dust continuum.

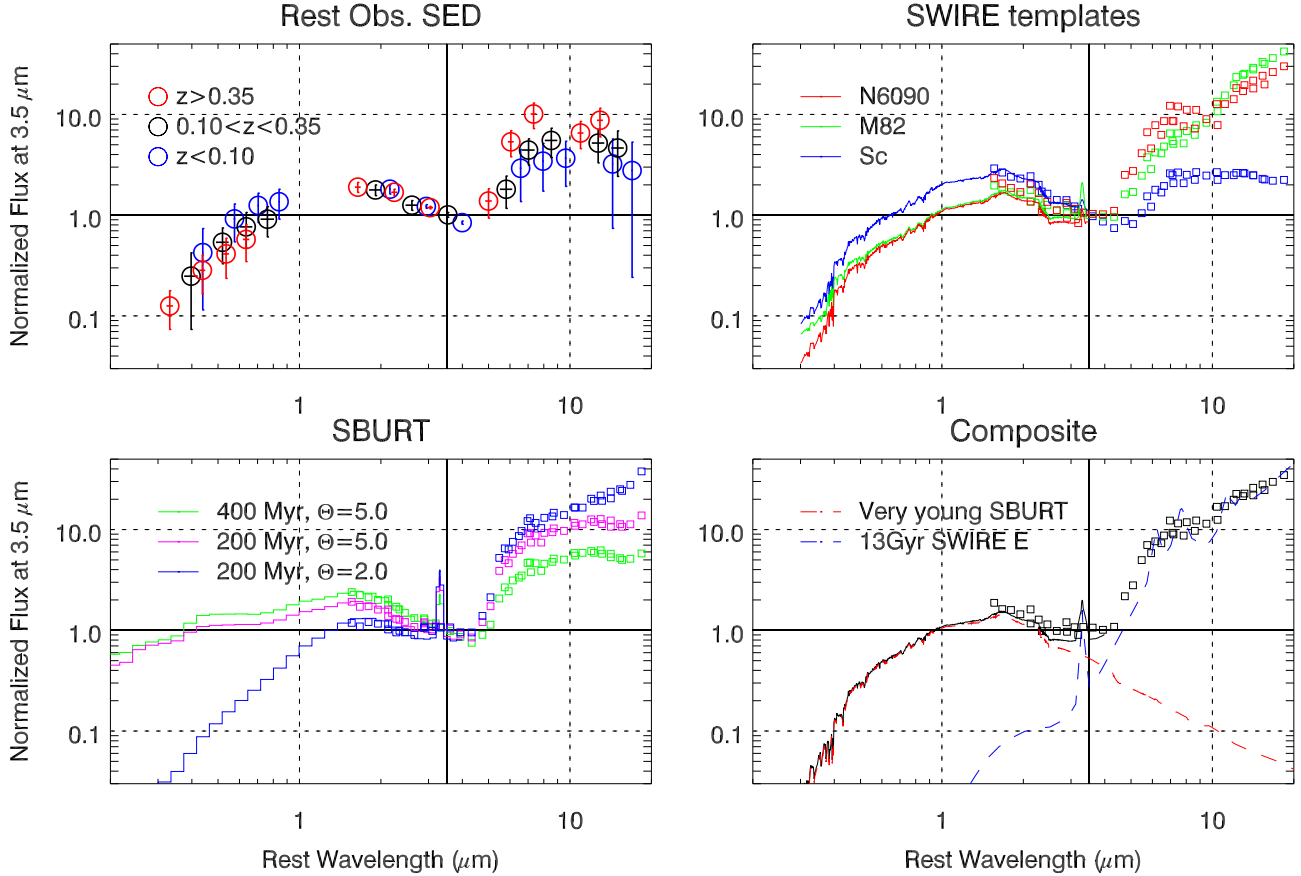


Fig. 22. Comparisons of the NIR-normalised rest-frame SEDs between the PAH galaxies and the templates and models. The normalisation wavelength is indicated by a black solid vertical line in each panel. *Top left:* averaged observed SEDs in each redshift bin from Fig. 15. *Top right:* SWIRE SED templates of Sc (blue), M82 (green), and NGC 6090 (red). *Bottom left:* SBURT SED models with $(t_{\text{burst}}, \Theta) = (400 \text{ Myr}, 5.0)$, $(200 \text{ Myr}, 5.0)$, and $(200 \text{ Myr}, 2.0)$ in green, magenta, and blue, respectively. *Bottom right:* two-component composite SED (black) that combines the SWIRE E (13 Gyr old) SED template (red broken line) and a very young and compact SBURT SED model (70 Myr, 1.0; blue broken line). For the template and the model SEDs, the reconstructed SEDs from the synthetic catalogue are shown with small boxes at NIR–MIR wavelengths, whereas the full-resolution original SEDs are shown at OPT–NIR wavelengths.

statistically more difficult in the lower redshift. However, such survey volume difference unlikely reproduces sudden change of the distribution of $F_{\text{rest } 7.7 \mu\text{m}}/F_{\text{rest } 3.5 \mu\text{m}}$ of the PAH galaxies at $z \approx 0.3\text{--}0.35$ (Fig. 20). Therefore, we conclude that abundance of the PAH-enhanced LIRGs becomes higher at $z \gtrsim 0.35$. This trend could be a part of the cosmic SFRD evolution whose peak comes at $z \approx 1\text{--}2$ (e.g. Menéndez-Delmestre et al. 2007; Farrah et al. 2008; Pope et al. 2008; Elbaz et al. 2011; Nordon et al. 2012; see also Goto et al. 2010, 2011a,b).

The fact that the PAH-luminous galaxies tend to show the PAH enhancement indicates that sSFR is larger in galaxies with larger SFR (Sect. 3.3.2). More specifically, vigorous starburst galaxies at $z > 0.35$ with $\text{SFR} \gtrsim 30 M_{\odot} \text{ yr}^{-1}$ show enhanced sSFR by up to a factor of two than an upper envelope of the sSFR distribution of modest starburst galaxies at $z < 0.35$ (Fig. 18). When compared to main sequence galaxies of $z \sim 0$ SDSS sample (Elbaz et al. 2007), the PAH-luminous and PAH-enhanced galaxies show larger sSFR than the local blue galaxies, whereas the PAH galaxies without PAH enhancement in the mid- z ($0.1 < z < 0.35$) redshift bin more closely follow the sequence. Takagi et al. (2010) identify their PAH-selected galaxies as $S11(11.0 \mu\text{m})/S7(7.0 \mu\text{m}) > 8$ at $z \sim 0.5$ in their NEP-Deep photometric sample, and argue that they are sources with larger sSFR. The PAH-enhanced population in this paper shows

$S11/S7 > 6$ at $z > 0.35$, about a half of which actually shows $S11/S7 > 8$ (Fig. 13). Hanami et al. (2012) find that sSFR in their MIR-detected star-formation-dominated population in their NEP-Deep photometric sample is higher at higher redshifts up to $z \sim 2$ at all stellar masses. Such redshift trend about sSFR in the SPICY sample as well as the NEP-Deep photometric samples seems in agreement with the fact that sSFR in star-forming galaxies is on average higher at higher redshifts (e.g. Elbaz et al. 2007, 2011; Schreiber et al. 2015).

The positive correlation between SFR and sSFR for the SPICY PAH galaxies can be naturally explained if they are burst-on-old composite. If one adds a burst of star formation on top of the old population, both SFR and sSFR of this galaxy increase. We introduced such composite to explain the PAH-enhanced population at $z \gtrsim 0.35$ (Sect. 3.4.3), but we can also generate a range of composites by adding different amount of the burst component, naturally generating the positive SFR–sSFR correlation. Takagi et al. (2010) have already demonstrated need for such composite population for their PAH-selected galaxies. They performed the SBURT SED fitting on their NEP-Deep photometric sample up to $z \sim 1$, and show that the single-burst models often predict weaker PAH features than the observations. They fitted the OPT–NIR–MIR SEDs of their PAH-selected sample, and obtain reasonably good fits for about half of their

sample galaxies, but fail for the other half because of their stronger-than-modeled PAH $7.7\mu\text{m}$. Their fit generally favours older ($t_{\text{burst}} \approx 400\text{ Myr}$) starbursts than our favoured middle-aged ones ($t_{\text{burst}} \approx 200\text{ Myr}$; Sect. 3.4.2) for the NIR–MIR SEDs, because they fitted the OPT SED together with the NIR–MIR one. The redder OPT SED causes the failure to reproduce the enhanced PAH features at the same time. Their results can be interpreted that such PAH-enhanced (U)LIRGs at $0.35 \lesssim z \lesssim 1$ are experiencing younger ($t_{\text{burst}} < 400\text{ Myr}$) starburst on top of old stellar components. We note that LIRGs are often interacting galaxies, if not major mergers (e.g. Armus et al. 2009; Kartaltepe et al. 2010, 2012; Stierwalt et al. 2013), and the burst-on-old composite seems a natural consequence in the interacting LIRGs, because the starburst there is triggered during the course of the interaction. NGC 6090 is also a merging LIRG, and it is not surprising that its SED resembles our composite SED (Sect. 3.4.3). We caution that, although the composite model is the preferred explanation of the SFR–SFR correlation, we cannot confirm this composite based on our spectral analysis (see also Sect. 3.4.3).

4.1.2. $F_{\text{rest } 11.3\mu\text{m}}/F_{\text{rest } 7.7\mu\text{m}}$ variation

We have shown that both the NGC 6090 SED template and the composite SED have problems in reproducing the relatively depressed $F_{\text{rest } 11.3\mu\text{m}}/F_{\text{rest } 7.7\mu\text{m}}$ for the PAH-enhanced population at $z \gtrsim 0.35$ (Sect. 3.4). In such starburst templates and models, both PAH $11.3\mu\text{m}$ and PAH $7.7\mu\text{m}$ luminosities, as well as hot dust continuum beneath these PAH features, increase in a similar way with SFR, causing only a small $F_{\text{rest } 11.3\mu\text{m}}/F_{\text{rest } 7.7\mu\text{m}}$ variation. The observations indeed show relatively small variation in this flux ratio at $z < 0.35$ (Figs. 20, 21).

We first examine effect of possible AGN contribution to the observed $F_{\text{rest } 11.3\mu\text{m}}/F_{\text{rest } 7.7\mu\text{m}}$ variation, and find this possibility very low. Although we already removed AGN-dominated sources based on the NIR/NIR–MIR/NIR colour–colour diagram (Sect. 3.2.1), a possibility remains that AGNs partly contribute to the total observed SEDs. We find that the unobscured AGNs, which typically show red continuum-dominated SEDs (Fig. 12), should not dominate at NIR. This is because the $F_{\text{rest } 3.5\mu\text{m}}/F_{\text{rest } 2.0\mu\text{m}}$ ratio shows little scatter and is consistent with the colour of the stellar SEDs (Sect. 3.3.2), and the rest-frame SEDs show a clear dip around $\approx 4\mu\text{m}$ (Sect. 3.2.3). Such constraints at NIR, however, do not apply to buried AGNs (e.g. Imanishi et al. 2007), because their SEDs are almost completely hidden at OPT–NIR wavelengths. The contribution of such buried AGNs seems also insignificant, because we find that the MIR SED is dominated by the PAH features around $7.7\mu\text{m}$ (Sect. 3.3.2). In addition, contribution of the red MIR continuum of both unobscured and buried AGNs would increase both $F_{\text{rest } 7.7\mu\text{m}}/F_{\text{rest } 3.5\mu\text{m}}$ and $F_{\text{rest } 11.3\mu\text{m}}/F_{\text{rest } 7.7\mu\text{m}}$, contradicting the observed trend for the PAH-enhanced population.

We examine other possible mechanisms to explain the observed $F_{\text{rest } 11.3\mu\text{m}}/F_{\text{rest } 7.7\mu\text{m}}$ trend, although we cannot identify the true cause. One possibility is that the broad $9.7\mu\text{m}$ silicate absorption absorbs more at $11.3\mu\text{m}$ than at $7.7\mu\text{m}$. We did not fit the SPICY spectra with the absorption (Sect. 2.3), but we instead compare the observed rest-frame SEDs with the absorbed NGC 6090 SED template. We adopted an extinction curve of Chiar & Tielens (2006) and a screen geometry, and followed the same procedure to reconstruct the rest-frame SED of the template by using synthetic photometry (Sect. 3.4). Figure 23 illustrates how the $11.3\mu\text{m}$ and the $7.7\mu\text{m}$ fluxes are

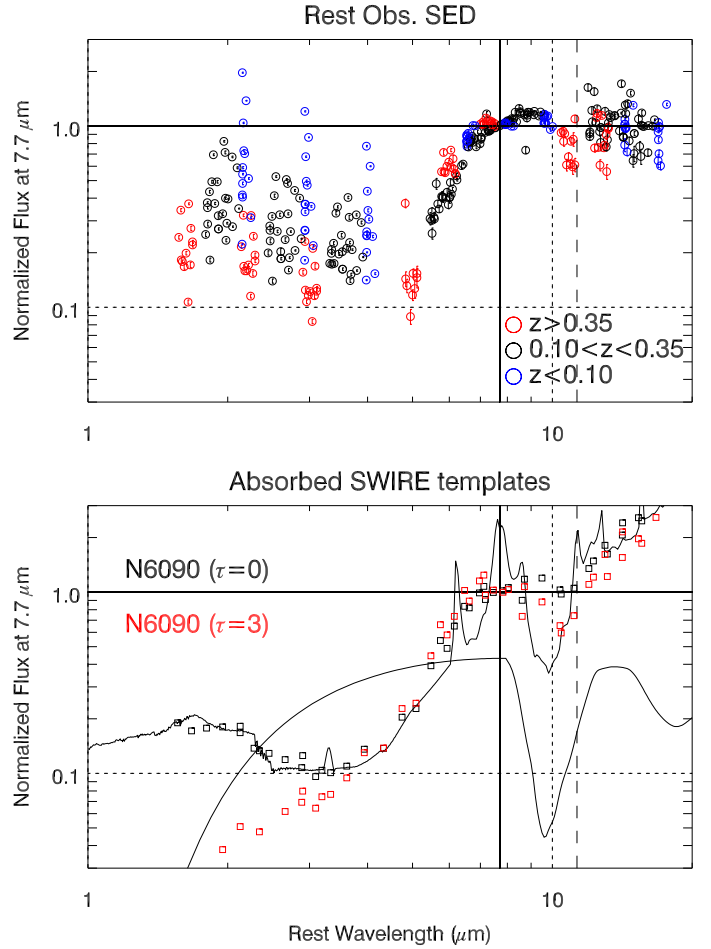


Fig. 23. Comparison between the observed MIR-normalised rest-frame SEDs of the PAH galaxies (taken from Fig. 14; top) and the absorbed and unabsorbed NGC 6090 SEDs (bottom). The unabsorbed ($\tau(9.7\mu\text{m}) = 0.0$) NGC 6090 SED (taken from Fig. 22) and the similar but absorbed ($\tau(9.7\mu\text{m}) = 3.0$) one are shown in black and red, respectively, in the bottom panel. We use the reconstructed SEDs from the synthetic catalogues. In addition, a full-resolution original (unabsorbed) NGC 6090 SED and an extinction curve for $\tau(9.7\mu\text{m}) = 3.0$ (with an arbitrary offset) are shown for reference. The normalisation wavelength ($7.7\mu\text{m}$) and the wavelength of $11.3\mu\text{m}$ are indicated by black solid and broken vertical lines, respectively, in each panel.

absorbed for the same amount of extinction. We find that the observations can be reproduced if the $9.7\mu\text{m}$ optical depth is as large as ≈ 3 . Galaxies with such deep silicate absorption are known to show much smaller ($\lesssim 1/10$) PAH equivalent widths than usual star-forming galaxies (Spoon et al. 2007). The PAH-enhanced population shows prominent PAH $6.2\mu\text{m}$ whose equivalent width is typically $1\mu\text{m}$ (Sect. 3.1), indicating that their MIR spectra are similar to PAH-rich star-forming galaxies without heavy silicate absorption. Although it seems unlikely based on the photometric analysis that most of the PAH-enhanced population suffers from such strong silicate absorption, we cannot test this possibility based on the spectroscopy due to limited wavelength coverage to enable the PAH fit with extinction for most of our sample. Another possibility to modify $F_{\text{rest } 11.3\mu\text{m}}/F_{\text{rest } 7.7\mu\text{m}}$ is to modify the PAH $11.3\mu\text{m}/7.7\mu\text{m}$ inter-band flux ratio by charging the PAH particles. Draine & Li (2001) show that this inter-band ratio in the warm ionised medium, as in PDRs, are quite different (smaller by up to about five times) from those in the cold neutral medium, such as in

the general ISM (see also Li & Draine 2001). Although this mechanism in principle can reproduce the observations, we cannot test this possibility due to lack of wavelength coverage for the redshifted PAH $11.3\,\mu\text{m}$ at $z \gtrsim 0.2$.

4.2. Advantages and limits of our slitless spectroscopic survey at MIR and its joint analysis with multi-band photometry

We have conducted the SPICY slitless spectroscopic survey at MIR, and studied extragalactic sources together with OPT–NIR–MIR multi-band photometry. We summarise what we can successfully perform with our unique dataset, and what we cannot due to the limitations. First, we can identify AGN-dominated sources with little ambiguity, by employing either our simple NIR colour selection and multi-band SED analysis (Sect. 3.2.1). Second, we can measure redshifts by using the simple PAH fit from the slitless survey data. We demonstrated that the PAH redshift is reasonably accurate and robust (1% or less in $dz/(1+z)$, without outliers, at $z < 0.5$), enabling good spectroscopic PAH luminosity measurement for the blindly selected sources at MIR. Third, we have shown that the photometric SED analysis by using the IRC filter set can provide good photometric PAH luminosity estimates without assuming models or intrinsic SED shapes. We then calibrated the photometric PAH luminosities to the spectroscopic ones, and find tight correlations without redshift dependence between them (Sect. 3.3.1). We thereby demonstrated that uncertainty associated with the K -correction is small for the photometric luminosity measurements. Because photometric observations can be deeper and reach much fainter sources below the spectroscopy sensitivity limit, the photometric approach may be essential for studying much fainter and more distant sources in the future. Spectroscopy following-up in the MIR of at least the brighter sub-sample should remain important to calibrate the photometric analysis results. Fourth, we can measure the stellar mass with little ambiguity by using the rest-frame NIR photometry of the stellar SED. By combining with the PAH luminosities, we can discuss star formation activities in terms of both SFR and sSFR up to $z \simeq 0.5$ without assuming the SED types with little ambiguity due to dust extinction. We emphasise that we can do such study for unbiased MIR-selected spectroscopic sample. We can also characterise the NIR–MIR SEDs of the PAH galaxies (tight NIR colour distribution, almost universal MIR bump shape, and systematic change of the MIR/NIR SED bump ratio), and broadly classify types of the galaxies (e.g. Sc, starburst, LIRG) only with photometric information (Sect. 3.4).

Despite the successes and advantages discussed above, our extragalactic survey has also suffered from many limitations. First, our redshift coverage is only limited to $z \simeq 0.5$ in order to detect the PAH $7.7\,\mu\text{m}$ in our wavelength coverage below $13\,\mu\text{m}$. To go beyond the current redshift limit to approach when SFRD shows its peak ($z \sim 2$), we need both longer wavelength coverage and more sensitivity to detect prominent PAH features. Second, we cannot detect the PAH $11.3\,\mu\text{m}$ for the PAH-enhanced population at $z > 0.35$ to distinguish physical reasons for the photometric $F_{\text{rest } 11.3\,\mu\text{m}}/F_{\text{rest } 7.7\,\mu\text{m}}$ variation (Sect. 4.1.2). Third, we cannot fit the $9.7\,\mu\text{m}$ silicate absorption for most cases. To reliably fit this broad absorption, one needs to cover up to rest-frame $\sim 14\,\mu\text{m}$ or longer so that hot dust continuum beyond the PAH complex around 11.3 – $13\,\mu\text{m}$ is included in the fit. Most of these limitations are caused by the limited long wavelength coverage of the instrument ($\simeq 13\,\mu\text{m}$). The higher spectral resolution than in our survey ($R \simeq 50$) would also help to fit the silicate absorption by better constraining the PAH profiles, especially (red tail

of) the PAH $8.6\,\mu\text{m}$ and (blue tail of) the PAH $11.3\,\mu\text{m}$, with more complicated and realistic spectral models of the PAHs. Fourth, although we can reliably measure the PAH luminosities, an ambiguity remains in converting the PAH luminosity to total IR luminosity and, thus, SFR (e.g. Nordon et al. 2012). The SED analysis over entire MIR and FIR wavelengths is needed. Fifth, we have no information about distributions of spectral or even photometric properties of individual galaxies due to lack of spatial resolution. We anticipate that such spatial information would provide us additional independent clues to identify physical processes that are responsible for the observed global characteristics. By mapping the PAH fluxes as well as the stellar continuum, we can find distributions of, for example, SFR, sSFR, and possible PAH inter-band flux ratios. We can then correlate these properties with distributions of, for example, usual disk star-forming regions and star formation induced by galaxy interaction or merger, as well as the nuclear activities (AGN or starburst). Such study would enable finding links to physical mechanisms that govern the galaxy evolution. Most of this limitation can be removed with larger-aperture and more-sensitive next-generation space infrared telescopes such as JWST (Kalirai 2018) and SPICA (Nakagawa et al. 2017).

5. Conclusions

In this paper, we have reported results from our MIR spectroscopic survey towards the NEP with the IRC on the AKARI space telescope. The survey, known as “slitless Spectroscopic survey of galaxies” (SPICY), is a slitless spectroscopic survey of a $9\,\mu\text{m}$ flux-selected sample. This is the very first blind spectroscopic survey conducted at MIR wavelengths. The biggest advantage of the slitless spectroscopy is that the survey can be unbiased, because sources are selected simply based on their flux at the same wavelengths as for the spectroscopy. This enables us to study the MIR evolution of galaxies in more robust way. We analysed the SPICY MIR spectra at 5 – $13\,\mu\text{m}$, together with multi (13)-band photometric data at OPT–NIR–MIR wavelengths (0.37 – $18\,\mu\text{m}$) from the combined AKARI–CFHT NEP photometric catalogue, to investigate star formation properties of galaxies at $z = 0.0$ – 0.5 .

We summarise the main results and conclusions below.

1. We collected 5 – $13\,\mu\text{m}$ low-resolution ($R \simeq 50$) spectra of $S9W$ ($9.0\,\mu\text{m}$) $> 0.3\,\text{mJy}$ sources within 14 IRC FOVs ($\simeq 14 \times 10' \times 10'$ regions). We performed simple PAH fit for the 6.2 , 7.7 , 8.6 , and $11.3\,\mu\text{m}$ PAH features on the detected extragalactic sources, excluding sources with damaged spectra (due to contamination and truncation that can randomly happen on the slitless spectroscopy images). We then find 48 galaxies with typical PAH features for star-forming galaxies (the PAH galaxies), with redshifts ranging $z = 0.0$ – 0.5 . We also identify 11 AGN candidates by using red NIR colours at 2 – $3\,\mu\text{m}$ (and also red MIR/NIR colours at 3 – $7\,\mu\text{m}$ as a secondary condition), so that the colours are consistent with those of the red continuum-dominated AGN SED template and all PAH galaxies are classified as non-AGNs. We confirm that the AGN candidates show red continuum-dominated SEDs at NIR–MIR wavelengths. The remaining non-AGN and non-PAH galaxies are mostly E–Sa with intrinsically weak PAH features, or faint Sc–starburst galaxies below the spectroscopy sensitivity, according to their broadband colours. Basic information about the PAH galaxies, including their source positions, OPT–NIR–MIR photometry, as well as the PAH fit results (redshifts and luminosities of the PAH $6.2\,\mu\text{m}$ and $7.7\,\mu\text{m}$), are reported. Similar

basic information about the bright AGN candidates are also reported.

2. We constructed rest-frame SEDs of the PAH galaxies at OPT–NIR–MIR wavelengths, with redshifts from the PAH fit. We find that the rest-frame SEDs look much simpler and universal within the sample, although the observed colours show extreme diversity as functions of spectral types (Sc, starburst, or LIRG) and redshift. This makes our analysis easier and probably more fundamental, in contrast to ones based on the observed-frame information. The SED is composed of an OPT–NIR (0.4–4 μm) bump (the stellar component) and a MIR (5–18 μm) one with a peak around 7.7 μm . Both the NIR slope of the OPT–NIR bump and shape of the MIR bump are almost identical within the sample. To characterise the SED shape, we defined and measured rest-frame flux ratios of $F_{\text{rest } 11.3 \mu\text{m}}/F_{\text{rest } 7.7 \mu\text{m}}$, $F_{\text{rest } 7.7 \mu\text{m}}/F_{\text{rest } 3.5 \mu\text{m}}$, and $F_{\text{rest } 3.5 \mu\text{m}}/F_{\text{rest } 2.0 \mu\text{m}}$. The $F_{\text{rest } 7.7 \mu\text{m}}/F_{\text{rest } 3.5 \mu\text{m}}$ ratio, which represents the relative strength of the MIR bump over the OPT–NIR one, systematically changes with redshift in a range of 2–14. This ratio increases with spectroscopic PAH luminosities, $L_{\text{PAH}}(7.7 \mu\text{m})$ and $L_{\text{PAH}}(6.2 \mu\text{m})$, indicating that the MIR bump is essentially composed of the PAH features around 7.7 μm , and specific SFR (SFR per stellar mass; sSFR) is higher for sources with higher SFR. In contrast, the $F_{\text{rest } 3.5 \mu\text{m}}/F_{\text{rest } 2.0 \mu\text{m}}$ ratio shows tight distribution and is consistent with the stellar colour. The $F_{\text{rest } 11.3 \mu\text{m}}/F_{\text{rest } 7.7 \mu\text{m}}$ ratio decreases by a factor of $\lesssim 2$ as $F_{\text{rest } 7.7 \mu\text{m}}/F_{\text{rest } 3.5 \mu\text{m}}$ increases by a factor of ~ 2 at $z \gtrsim 0.35$.
3. We photometrically measured the monochromatic luminosities at the peak of the PAH 7.7 μm ($\nu L_{\nu \text{ photo}}(7.7 \mu\text{m})$), and compared them with those of the spectroscopy (spectroscopic PAH 7.7 μm luminosity, $L_{\text{PAH}}(7.7 \mu\text{m})$, and spectroscopic monochromatic luminosities at the peak of the PAH 7.7 μm , $\nu L_{\nu \text{ spec}}(7.7 \mu\text{m})$). We find tight correlations among them, with little systematic offset as a function of redshift, and report the scaling relations.
4. We identify PAH-enhanced population showing $\log \nu L_{\nu \text{ photo}}(7.7 \mu\text{m}) > 0.50 + \log \nu L_{\nu \text{ photo}}(3.5 \mu\text{m})$ (or, equivalently, $F_{\text{rest } 7.7 \mu\text{m}}/F_{\text{rest } 3.5 \mu\text{m}} > 7.0$) at $z \gtrsim 0.35$. Here, $\nu L_{\nu \text{ photo}}(3.5 \mu\text{m})$ is a monochromatic photometric luminosities at 3.5 μm . They show elevated SFR ($\gtrsim 30 M_{\odot} \text{ yr}^{-1}$), being comparable to LIRGs, and also elevated sSFR (by about a factor of two when compared to the upper envelope of the sSFR distribution at $z < 0.35$). We find no such PAH-enhanced population at lower redshifts, and we argue that this is neither due to source selection biases nor by chance due to small number statistic.
5. We find that the SWIRE SED templates of normal and star-forming galaxies, Sc, starburst (M82), and LIRG (NGC 6090), can mostly reproduce both the rest-frame SEDs and the flux ratios of the PAH galaxies. We also find that the SBURT starburst models (Takagi et al. 2003a) for older ($t_{\text{burst}} \gtrsim 200 \text{ Myr}$) starburst with modest optical depth can mostly reproduce the observations. For the PAH-luminous and PAH-enhanced population at $z \gtrsim 0.35$ in particular, both the NGC 6090 template and the SBURT model for middle-aged ($t_{\text{burst}} \approx 200 \text{ Myr}$) starburst with modest optical depth can reproduce the observed NIR–MIR SEDs. This SBURT model, however, has a problem in reproducing relatively red OPT SEDs at the same time as the enhanced MIR bump. We developed a composite SED that combines a very young ($\approx 70 \text{ Myr}$), compact ($\Theta = 1.0$) and, hence, optically very thick SBURT model and a very old (13 Gyr old) SWIRE template, and find that it can reproduce the overall OPT–NIR–

MIR SEDs of the PAH-enhanced population. This suggests that the PAH-enhanced population shows very young and vigorous star-formation activities on the old stellar system, although we cannot confirm the presence of the optically thick component from our spectral analysis. We note that the positive correlation between SFR and sSFR for the PAH galaxies in general can also be explained by the composite models, by changing relative contribution of the very young component over the old one. Both this composite SED and the NGC 6090 SED template still have difficulties in reproducing the relatively depressed $F_{\text{rest } 11.3 \mu\text{m}}/F_{\text{rest } 7.7 \mu\text{m}}$ for the PAH-enhanced population.

Acknowledgements. YO acknowledges supports from Ministry of Science and Technology (MOST) of Taiwan MOST 106-2112-M-001-008- and MOST 107-2119-M-001-026-. MI acknowledges the support from the National Research Foundation of Korea (NRFC) grant, No. 2017R1A3A3A001362, funded by the Korean government (MSIP). GJW gratefully acknowledges support from The Leverhulme Trust. TM is supported by UNAM-DGAPA PAPIIT IN104216 and CONACyT 252531. TN acknowledges support from the JSPS KAKENHI Grant Number 26247030. This research is based on observations with AKARI, a JAXA project with the participation of ESA, and is partly supported with the Grant-in-Aid for Scientific Research (21340042) from the JSPS. This work is based in part on observations made with the *Spitzer* Space Telescope, obtained from the NASA/IPAC Infrared Science Archive, both of which are operated by the Jet Propulsion Laboratory, California Institute of Technology under a contract with the National Aeronautics and Space Administration. This research used observations made with the Gran Telescopio Canarias (GTC), installed in the Spanish Observatorio del Roque de los Muchachos of the Instituto de Astrofísica de Canarias, in the island of La Palma.

References

- Armus, L., Mazzarella, J. M., Evans, A. S., et al. 2009, *PASP*, **121**, 559
- Babbedge, T. S. R., Rowan-Robinson, M., Vaccari, M., et al. 2006, *MNRAS*, **370**, 1159
- Bavouzet, N., Dole, H., Le Floc'h, E., et al. 2008, *A&A*, **479**, 83
- Berta, S., Magnelli, B., Nordon, R., et al. 2011, *A&A*, **532**, A49
- Bertin, E., & Arnouts, S. 1996, *A&AS*, **117**, 393
- Brandl, B. R., Bernard-Salas, J., Spoon, H. W. W., et al. 2006, *ApJ*, **653**, 1129
- Caputi, K. I., Lagache, G., Yan, L., et al. 2007, *ApJ*, **660**, 97
- Castro, A., Miyaji, T., Shirahata, M., et al. 2014, *PASJ*, **66**, 110
- Cesarsky, C. J., Abergel, A., Agnese, P., et al. 1996, *A&A*, **315**, L32
- Chary, R., & Elbaz, D. 2001, *ApJ*, **556**, 562
- Chiar, J. E., & Tielens, A. G. G. M. 2006, *ApJ*, **637**, 774
- Dale, D. A., Helou, G., Contursi, A., Silbermann, N. A., & Kolhatkar, S. 2001, *ApJ*, **549**, 215
- Dale, D. A., Smith, J. D. T., Armus, L., et al. 2006, *ApJ*, **646**, 161
- Dole, H., Lagache, G., Puget, J.-L., et al. 2006, *A&A*, **451**, 417
- Donley, J. L., Koekemoer, A. M., Brusa, M., et al. 2012, *ApJ*, **748**, 142
- Draine, B. T., & Li, A. 2001, *ApJ*, **551**, 807
- Edelson, R., Malkan, M., & Rieke, G. 1987, *ApJ*, **321**, 233
- Elbaz, D., Cesarsky, C. J., Fadda, D., et al. 1999, *A&A*, **351**, L37
- Elbaz, D., Cesarsky, C. J., Chanial, P., et al. 2002, *A&A*, **384**, 848
- Elbaz, D., Daddi, E., Le Borgne, D., et al. 2007, *A&A*, **468**, 33
- Elbaz, D., Dickinson, M., Hwang, H. S., et al. 2011, *A&A*, **533**, A119
- Elvis, M., Wilkes, B. J., McDowell, J. C., et al. 1994, *ApJS*, **95**, 1
- Farrah, D., Bernard-Salas, J., Spoon, H. W. W., et al. 2007, *ApJ*, **667**, 149
- Farrah, D., Lonsdale, C. J., Weedman, D. W., et al. 2008, *ApJ*, **677**, 957
- Fazio, G. G., Hora, J. L., Allen, L. E., et al. 2004, *ApJS*, **154**, 10
- Geach, J. E., Dunlop, J. S., Halpern, M., et al. 2017, *MNRAS*, **465**, 1789
- Genzel, R., Lutz, D., Sturm, E., et al. 1998, *ApJ*, **498**, 579
- Goto, T., Takagi, T., Matsuhara, H., et al. 2010, *A&A*, **514**, A6
- Goto, T., Arnouts, S., Inami, H., et al. 2011a, *MNRAS*, **410**, 573
- Goto, T., Arnouts, S., Malkan, M., et al. 2011b, *MNRAS*, **414**, 1903
- Gruppioni, C., Pozzi, F., Rodighiero, G., et al. 2013, *MNRAS*, **432**, 23
- Hanami, H., Ishigaki, T., Fujishiro, N., et al. 2012, *PASJ*, **64**, 70
- Hao, L., Weedman, D. W., Spoon, H. W. W., et al. 2007, *ApJ*, **655**, L77
- Houck, J. R., Roellig, T. L., van Cleve, J., et al. 2004, *ApJS*, **154**, 18
- Houck, J. R., Weedman, D. W., Le Floc'h, E., & Hao, L. 2007, *ApJ*, **671**, 323
- Hwang, N., Lee, M. G., Lee, H. M., et al. 2007, *ApJS*, **172**, 583
- Ichikawa, K., Imanishi, M., Ueda, Y., et al. 2014, *ApJ*, **794**, 139
- Imanishi, M., Dudley, C. C., Maiolino, R., et al. 2007, *ApJS*, **171**, 72
- Imanishi, M., Nakagawa, T., Ohyama, Y., et al. 2008, *PASJ*, **60**, S489

- Imanishi, M., Nakagawa, T., Shirahata, M., Ohyama, Y., & Onaka, T. 2010, *ApJ*, **721**, 1233
- Ishihara, D., Onaka, T., Katata, H., et al. 2010, *A&A*, **514**, A1
- Ita, Y., Onaka, T., Kato, D., et al. 2008, *PASJ*, **60**, 435
- Jeon, Y., Im, M., Ibrahimov, M., et al. 2010, *ApJS*, **190**, 166
- Jeon, Y., Im, M., Kang, E., Lee, H. M., & Matsuhara, H. 2014, *ApJS*, **214**, 20
- John, T. L. 1988, *A&A*, **193**, 189
- Kalirai, J. 2018, *Contemporary Physics*, **59**, 251
- Karl, S. J., Naab, T., Johansson, P. H., et al. 2010, *ApJ*, **715**, L88
- Kartaltepe, J. S., Sanders, D. B., Le Floch, E., et al. 2010, *ApJ*, **721**, 98
- Kartaltepe, J. S., Dickinson, M., Alexander, D. M., et al. 2012, *ApJ*, **757**, 23
- Kennicutt, Jr., R. C. 1998, *ARA&A*, **36**, 189
- Kennicutt, Jr., R. C., Armus, L., Bendo, G., et al. 2003, *PASP*, **115**, 928
- Kessler, M. F., Steinz, J. A., Anderegg, M. E., et al. 1996, *A&A*, **315**, L27
- Kim, S. J., Lee, H. M., Matsuhara, H., et al. 2012, *A&A*, **548**, A29
- Ko, J., Im, M., Lee, H. M., et al. 2012, *ApJ*, **745**, 181
- Krumpe, M., Miyaji, T., Brunner, H., et al. 2015, *MNRAS*, **446**, 911
- Lacy, M., Storie-Lombardi, L. J., Sajina, A., et al. 2004, *ApJS*, **154**, 166
- Lagache, G., Dole, H., Puget, J.-L., et al. 2004, *ApJS*, **154**, 112
- Lee, H. M., Kim, S. J., Im, M., et al. 2009, *PASJ*, **61**, 375
- Le Floch, E., Papovich, C., Dole, H., et al. 2005, *ApJ*, **632**, 169
- Li, A., & Draine, B. T. 2001, *ApJ*, **554**, 778
- Lutz, D., Spoon, H. W. W., Rigopoulou, D., Moorwood, A. F. M., & Genzel, R. 1998, *ApJ*, **505**, L103
- Magdis, G. E., Daddi, E., Béthermin, M., et al. 2012, *ApJ*, **760**, 6
- Magnelli, B., Popesso, P., Berta, S., et al. 2013, *A&A*, **553**, A132
- Matsuhara, H., Wada, T., Matsuura, S., et al. 2006, *PASJ*, **58**, 673
- Menéndez-Delmestre, K., Blain, A. W., Alexander, D. M., et al. 2007, *ApJ*, **655**, L65
- Murakami, H., Baba, H., Barthel, P., et al. 2007, *PASJ*, **59**, 369
- Murata, K., Matsuhara, H., Wada, T., et al. 2013, *A&A*, **559**, A132
- Murphy, E. J., Chary, R.-R., Dickinson, M., et al. 2011, *ApJ*, **732**, 126
- Nakagawa, T., Shibai, H., Kaneda, H., et al. 2017, *Pub. Korean Astron. Soc.*, **32**, 331
- Nordon, R., Lutz, D., Genzel, R., et al. 2012, *ApJ*, **745**, 182
- Ohyama, Y., Onaka, T., Matsuhara, H., et al. 2007, *PASJ*, **59**, 411
- Oi, N., Matsuhara, H., Murata, K., et al. 2014, *A&A*, **566**, A60
- Onaka, T., Matsuhara, H., Wada, T., et al. 2007, *PASJ*, **59**, 401
- Pearson, C. P. 2001, *MNRAS*, **325**, 1511
- Pearson, C. P., Oyabu, S., Wada, T., et al. 2010, *A&A*, **514**, A8
- Pérez-González, P. G., Rieke, G. H., Egami, E., et al. 2005, *ApJ*, **630**, 82
- Pilbratt, G. L., Riedinger, J. R., & Passvogel, T. 2010, *A&A*, **518**, LL1
- Polletta, M., Tajer, M., Maraschi, L., et al. 2007, *ApJ*, **663**, 81
- Pope, A., Chary, R.-R., Alexander, D. M., et al. 2008, *ApJ*, **675**, 1171
- Rieke, G. H., Young, E. T., Engelbracht, C. W., et al. 2004, *ApJS*, **154**, 25
- Rigopoulou, D., Spoon, H. W. W., Genzel, R., et al. 1999, *AJ*, **118**, 2625
- Rowan-Robinson, M., Lari, C., Perez-Fournon, I., et al. 2004, *MNRAS*, **351**, 1290
- Sajina, A., Yan, L., Armus, L., et al. 2007, *ApJ*, **664**, 713
- Sanders, D. B., Mazzarella, J. M., Kim, D.-C., Surace, J. A., & Soifer, B. T. 2003, *AJ*, **126**, 1607
- Sawicki, M. 2002, *AJ*, **124**, 3050
- Schreiber, C., Pannella, M., Elbaz, D., et al. 2015, *A&A*, **575**, A74
- Scoville, N. Z., Evans, A. S., Thompson, R., et al. 2000, *AJ*, **119**, 991
- Serjeant, S., Oliver, S., Rowan-Robinson, M., et al. 2000, *MNRAS*, **316**, 768
- Shim, H., Im, M., Ko, J., et al. 2013, *ApJS*, **207**, 37
- Shipley, H. V., Papovich, C., Rieke, G. H., Brown, M. J. I., & Moustakas, J. 2016, *ApJ*, **818**, 60
- Silva, L., Granato, G. L., Bressan, A., & Danese, L. 1998, *ApJ*, **509**, 103
- Smith, J. D. T., Draine, B. T., Dale, D. A., et al. 2007, *ApJ*, **656**, 770
- Stierwalt, S., Armus, L., Surace, J. A., et al. 2013, *ApJS*, **206**, 1
- Spinoglio, L., Malkan, M. A., Rush, B., Carrasco, L., & Recillas-Cruz, E. 1995, *ApJ*, **453**, 616
- Spoon, H. W. W., Marshall, J. A., Houck, J. R., et al. 2007, *ApJ*, **654**, L49
- Takagi, T., & Pearson, C. P. 2005, *MNRAS*, **357**, 165
- Takagi, T., Arimoto, N., & Hanami, H. 2003a, *MNRAS*, **340**, 813
- Takagi, T., Vansevicius, V., & Arimoto, N. 2003b, *PASJ*, **55**, 385
- Takagi, T., Hanami, H., & Arimoto, N. 2004, *MNRAS*, **355**, 424
- Takagi, T., Matsuhara, H., Wada, T., et al. 2007, *PASJ*, **59**, 557
- Takagi, T., Ohyama, Y., Goto, T., et al. 2010, *A&A*, **514**, A5
- Takagi, T., Matsuhara, H., Goto, T., et al. 2012, *A&A*, **537**, A24
- Wada, T., Oyabu, S., Ita, Y., et al. 2007, *PASJ*, **59**, 515
- Wada, T., Matsuhara, H., Oyabu, S., et al. 2008, *PASJ*, **60**, 517
- Weedman, D. W., & Houck, J. R. 2008, *ApJ*, **686**, 127
- Woo, J.-H., Kim, J. H., Imanishi, M., & Park, D. 2012, *AJ*, **143**, 49
- Wu, Y., Helou, G., Armus, L., et al. 2010, *ApJ*, **723**, 895
- Xu, C., Hacking, P. B., Fang, F., et al. 1998, *ApJ*, **508**, 576
- Yan, L., Helou, G., Fadda, D., et al. 2004, *ApJS*, **154**, 60
- Yan, L., Sajina, A., Fadda, D., et al. 2007, *ApJ*, **658**, 778
- Yano, K., Nakagawa, T., Isobe, N., & Shirahata, M. 2016, *ApJ*, **833**, 272
- 1 Academia Sinica, Institute of Astronomy and Astrophysics, 11F of Astronomy-Mathematics Building, AS/NTU, No. 1, Sec. 4, Roosevelt Rd., Taipei 10617, Taiwan, ROC
e-mail: ohyama@asiaa.sinica.edu.tw
 - 2 Institute of Space and Astronautical Science, Japan Aerospace Exploration Agency, 3-1-1 Yoshinodai, Chuo-ku, Sagami-hara, Kanagawa 252-5210, Japan
 - 3 Japan Space Forum, Shin-Ochanomizu Urban Trinity Bldg. 2F 3-2-1, Kandasurugadai, Chiyoda-ku, Tokyo 101-0062, Japan
 - 4 Division of Astronomy and Astrophysics, University of California, Los Angeles, 430 Portola Plaza, Box 951547, Los Angeles, CA 90095-1547, USA
 - 5 Dark Cosmology Centre, Niels Bohr Institute, University of Copenhagen, Juliane Maries Vej 30, 2100 Copenhagen Ø, Denmark
 - 6 National Tsing hua University, No. 101, Section 2, Kuang-Fu Road, Hsinchu 30013, Taiwan, ROC
 - 7 Steward Observatory, University of Arizona, 933 N. Cherry Ave, Tucson, AZ 85721, USA
 - 8 Astronomy Program, Department of Physics and Astronomy, Seoul National University, Shillim-Dong, Kwanak-Gu, Seoul 151-742, Republic of Korea
 - 9 Subaru Telescope, National Astronomical Observatory of Japan, 650 North Aohoku Place, Hilo, HI 96720, USA
 - 10 RAL Space, STFC Rutherford Appleton Laboratory, Chilton, Didcot, Oxfordshire OX11 0QX, UK
 - 11 Department of Physics and Astronomy, The Open University, Walton Hall, Milton Keynes MK7 6AA, UK
 - 12 Oxford Astrophysics, Denys Wilkinson Building, University of Oxford, Keble Rd, Oxford OX1 3RH, UK
 - 13 National Optical Astronomy Observatory, 950 North Cherry Avenue, Tucson, AZ 85719, USA
 - 14 CRAL, Observatoire de Lyon, 9, avenue Charles André, 69561 Saint-Genis-Laval, France
 - 15 Graduate School of Science, Nagoya University, Furo-cho, Chikusa-ku, Nagoya, Aichi 464-8602, Japan
 - 16 Graduate School of Science, The University of Tokyo, 7-3-1 Hongo, Bunkyo-ku, Tokyo 113-0033, Japan
 - 17 Center for Planetary Science, Graduate School of Science, Kobe University, 7-1-48 Minatogijima-Minamimachi, Chuo-Ku, Kobe 650-0047, Japan
 - 18 Laboratoire d'Astrophysique de Marseille, Pôle de l'Étoile Site de Château-Gombert 38, rue Frédéric Joliot-Curie, 13388 Marseille Cedex 13, France
 - 19 National Astronomical Observatory of Japan, 2-21-1 Osawa, Mitaka, Tokyo 181-8588, Japan
 - 20 Korea Astronomy and Space Science Institute, 776 Daedeokdae-ro, Yuseong-gu, Daejeon 34055, Republic of Korea
 - 21 Instituto de Astronomía Campus Ensenada, Universidad Nacional Autónoma de México, Km. 103 Carretera Tijuana-Ensenada, Ensenada, Baja California 22860, Mexico
 - 22 Physics Section, Faculty of Humanities and Social Sciences, Iwate University, Morioka 020-8550, Japan
 - 23 Department of Astronomy, Kyoto University, Kitashirakawa-Oiwake-cho, Sakyo-ku, Kyoto 606-8502, Japan

Appendix A: Design of the SPICY survey in detail

The SPICY survey is a blind slitless spectroscopic extragalactic survey at MIR by using the IRC onboard AKARI (Sect. 2.1). We targeted the NEP located in the continuous visibility zone (CVZ) of the AKARI satellite in sun-synchronous orbit. Due to severe scheduling constraints posed mostly by the all sky survey of the AKARI mission, the NEP is the only field on the sky where AKARI was able to perform repeated observations of the same field for deeper observations (Matsuhara et al. 2006). For the SPICY survey, we visited the same pointing coordinates nine or ten times to achieve our sensitivity goal (Sect. 2.1). Another CVZ field, the south ecliptic pole (SEP), shows much more Galactic cirrus and is close to the LMC, so is less-suited to extragalactic deep surveys. This survey programme was conducted as one of AKARI's key projects ("mission programme"), and ≈ 110 pointing opportunities were assigned for it during the cold phase of the AKARI mission. This survey was executed during July 2006 and August 2007.

The SPICY survey footprint was designed to efficiently combine spectra taken with the separate cameras of the IRC, under the following technical limitations. The IRC (see Onaka et al. 2007 for full details) is composed of three independent cameras that operate simultaneously, and they are called "NIR", "MIR-S", and "MIR-L" for wavelength ranges of $2\text{--}5\mu\text{m}$, $6\text{--}13\mu\text{m}$, and $13\text{--}27\mu\text{m}$, respectively. Each camera covers an $\approx 10' \times 10'$ FOV, and the NIR and MIR-S share the same FOV via a beam splitter. The MIR-L has its own FOV to cover slightly offset ($\approx 20'$) sky area. By overlapping the FOV coverage of the MIR-L onto ones of the NIR and MIR-S, we achieved the combined

wavelength coverage between $2\mu\text{m}$ and $27\mu\text{m}$. We note, however, that we utilise only the MIR-S spectra for the purpose of this paper (Sect. 2.1). To enable this, we utilised the fact that the IRC FOV rotates by 1° per day at the NEP due to AKARI's sun-synchronous orbit. We scheduled all observations for a pointing coordinate as close in time as possible to each other to minimise such FOV rotation. This set of the observations defines one observing field, called a tile. After completing the very first tile, the second tile was observed about three months later, when the FOV had rotated by 90° and the new square tile could be directly overlaid on the previous square (but 90° rotated) tile. Here, the new pointing coordinates were set in order to overlay the new MIR-L tile on the previous tile of NIR and MIR-S. This generated a new tile of NIR and MIR-S $\approx 20'$ off the first tile. This new coverage of the second NIR and MIR-S tile was further observed about another three month later with the MIR-L. We repeated this sequence every ≈ 3 months, to extend a chain of the tiles where all NIR, MIR-S, and MIR-L FOVs overlap with each other. The survey tiles thus created are distributed in a non-contiguous way around the NEP, showing a complicated shape of folded chains of 14 tiles (Fig. 1). In reality, however, the chain of the tiles was interrupted a few times before completing the survey, due to telescope scheduling constraints.

Appendix B: Spectra of all SPICY PAH galaxies.

The SG1 and SG2 spectra of all 48 SPICY PAH galaxies are presented with the PAH fit results overlaid. Only four of them are shown as examples in Fig. 4.

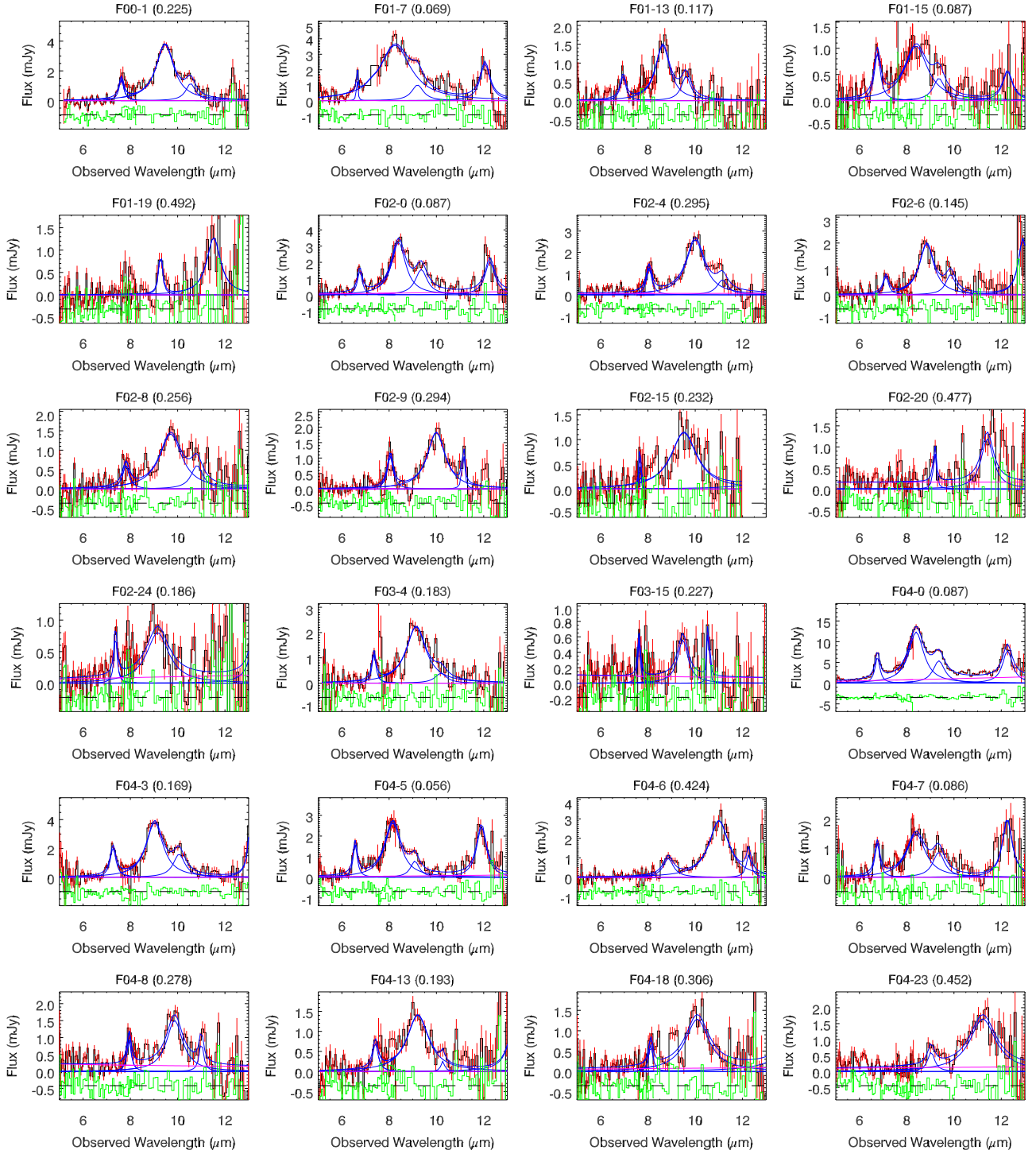


Fig. B.1. SG1 and SG2 spectra of the SPICY PAH galaxies with the PAH fit results overlaid. The observed spectrum is shown in red line with one-sigma error bars, with the fitted individual PAH components (blue), the power-law continuum (magenta), and their sum (blue) in each panel. The residual of the fit (observed–fitted) is shown in green at offset baseline (horizontal broken line) for clarity. The redshift from the PAH fit is indicated next to the source name in the plot title. The Y axis is scaled to have the same PAH 7.7 μm peak height for all galaxies.

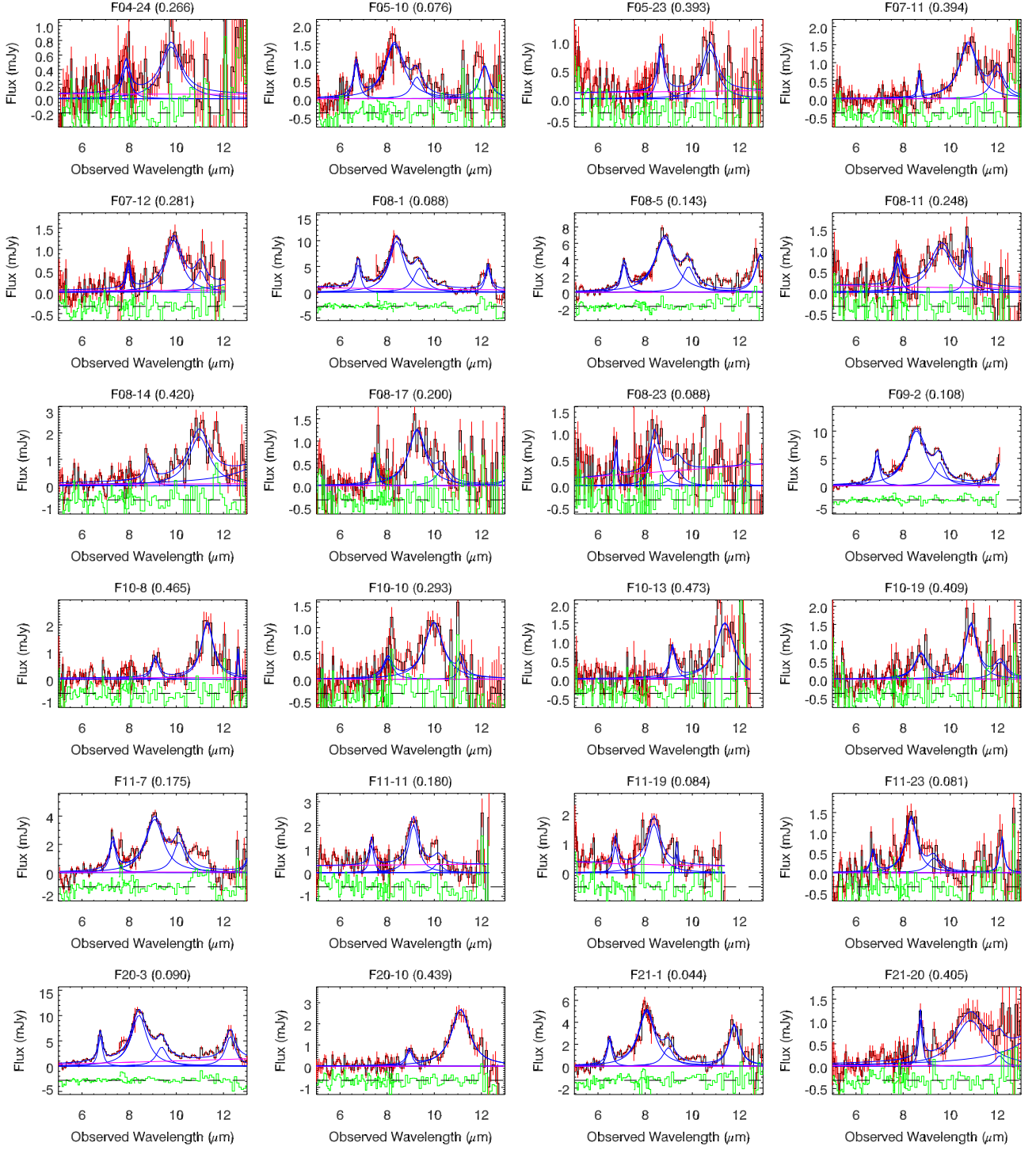


Fig. B.1. continued.

Appendix C: Additional tables

Table C.1. Source identification, cross-identification with the NEP-Wide catalogue, and the SPICY S_{9W} ($9.0\mu\text{m}$) photometry of the PAH galaxies, together with cross-identification with the CFHT optical NEP photometric catalogue.

SPICY ID	NEP-Wide catalogue			SPICY S_{9W} flux (mJy)	CFHT NEP catalogue	
	ID	RA J2000 (hms)	Dec J2000 (dms)		ID	FIELD
F00-1	65030479	17 55 19.91	+66 41 45.2	1.25 ± 0.04	48924	2
F01-7	65047593	17 58 40.87	+66 22 14.1	1.63 ± 0.05	23532	2
F01-13	65042346	17 57 39.74	+66 20 53.2	0.64 ± 0.02	20669	2
F01-15	65046006	17 58 21.61	+66 24 45.8	0.59 ± 0.02	25461	2
F01-19	65042020	17 57 35.87	+66 22 04.4	0.40 ± 0.02	21980	2
F02-0	65056911	18 00 28.93	+66 12 29.6	1.37 ± 0.04	9818	1
F02-4	65059749	18 00 59.84	+66 10 56.5	0.91 ± 0.03	7723	1
F02-6	65063554	18 01 42.08	+66 13 00.4	0.77 ± 0.03	10219	1
F02-8	65060828	18 01 11.75	+66 11 39.6	0.67 ± 0.02	8535	1
F02-9	65057478	18 00 35.22	+66 13 44.9	0.65 ± 0.02	10871	1
F02-15	65060902	18 01 12.43	+66 16 54.4	0.46 ± 0.02	14047	1
F02-20	65058156	18 00 42.29	+66 08 20.4	0.39 ± 0.02	4847	1
F02-24	65057873	18 00 39.35	+66 13 52.3	0.33 ± 0.01	11076	1
F03-4	65019934	17 53 06.59	+66 34 28.4	0.93 ± 0.03	38180	2
F03-15	65020331	17 53 11.78	+66 36 08.5	0.33 ± 0.01	40557	2
F04-0	65037228	17 56 39.96	+66 48 00.6	5.48 ± 0.17	56817	2
F04-3	65038399	17 56 53.90	+66 39 22.3	1.83 ± 0.06	45137	2
F04-5	65039972	17 57 11.55	+66 45 23.0	1.15 ± 0.04	54615	2
F04-6	65041345	17 57 27.79	+66 45 56.6	0.76 ± 0.03	53989	2
F04-7	65038112	17 56 50.77	+66 44 44.7	0.74 ± 0.03	53152	2
F04-8	65041041	17 57 24.35	+66 42 36.5	0.61 ± 0.02	49849	2
F04-13	65040771	17 57 21.13	+66 42 34.6	0.50 ± 0.02	50195	2
F04-18	65040361	17 57 15.99	+66 43 40.0	0.44 ± 0.02	51197	2
F04-23	65035546	17 56 19.78	+66 47 36.1	0.41 ± 0.02	55840	2
F04-24	65040327	17 57 15.56	+66 48 21.6	0.38 ± 0.01 ^a
F05-10	65054492	18 00 01.60	+66 54 02.4	0.75 ± 0.03	59396	1
F05-23	65054321	17 59 59.66	+66 50 09.2	0.33 ± 0.01	52788	1
F07-11	65026631	17 54 33.33	+66 47 47.7	0.55 ± 0.02	56082	2
F07-12	65020847	17 53 18.84	+66 44 39.7	0.53 ± 0.02	52573	2
F08-1	65027087	17 54 38.96	+66 23 16.2	4.01 ± 0.12 ^b
F08-5	65030601	17 55 21.36	+66 24 26.4	2.88 ± 0.09	24990	2
F08-11	65031482	17 55 31.62	+66 23 42.1	0.80 ± 0.03	23958	2
F08-14	65030371	17 55 18.77	+66 25 30.9	0.74 ± 0.03	26271	2
F08-17	65028594	17 54 57.58	+66 25 52.6	0.54 ± 0.02	26549	2
F08-23	65027474	17 54 43.76	+66 21 04.0	0.49 ± 0.02	20996	2
F09-2	65023172	17 53 48.51	+66 39 20.9	4.21 ± 0.13	45556	2
F10-8	65038265	17 56 52.46	+66 27 36.0	0.53 ± 0.02	28701	2
F10-10	65041559	17 57 30.25	+66 30 06.1	0.48 ± 0.02	31653	2
F10-13	65037342	17 56 41.54	+66 27 04.1	0.46 ± 0.02	27999	2
F10-19	65041158	17 57 25.61	+66 29 46.5	0.35 ± 0.01	31398	2
F11-7	65038292	17 56 52.78	+66 06 40.8	1.56 ± 0.05	3548	2
F11-11	65040931	17 57 22.90	+66 05 09.5	0.94 ± 0.03	1673	2
F11-19	65040367	17 57 16.08	+66 04 54.4	0.64 ± 0.02	2082	2
F11-23	65043924	17 57 58.08	+66 07 09.0	0.53 ± 0.02	4163	2
F20-3	65045989	17 58 21.42	+66 28 55.3	4.12 ± 0.13	30856	2
F20-10	65051479	17 59 26.77	+66 29 39.3	0.51 ± 0.02	31374	2
F21-1	65032713	17 55 46.52	+66 38 39.9	2.10 ± 0.07	44027	2
F21-20	65031307	17 55 29.48	+66 40 35.5	0.32 ± 0.01	46860	2

Notes. FIELD indicates one of the two survey fields defined in [Hwang et al. \(2007\)](#); 1 and 2 for the NEP-E and NEP-W fields, respectively). ^(a)This source is damaged due to a nearby bright and saturated star on the CFHT image, and is not catalogued. ^(b)This source falls on one of CCD gaps on the CFHT image, and is not catalogued.

Table C.2. Results of the PAH fit of the SPICY PAH galaxies.

ID	SPICY PAH fit				Optical spectroscopy		
	Redshift (z)	$\log L$ (PAH 6.2 μm) (L_\odot)	$\log L$ (PAH 7.7 μm) (L_\odot)	$\log \nu L_{\nu\text{spec}}$ (7.7 μm) (L_\odot)	Redshift (z)	Quality	Source
F00-1	0.225 ± 0.001	$9.042^{+0.047}_{-0.052}$	$9.853^{+0.021}_{-0.022}$	$10.670^{+0.012}_{-0.012}$	0.2270,0.227	4,4	1,2
F01-7	0.069 ± 0.001	$7.516^{+0.201}_{-0.386}$	$9.074^{+0.022}_{-0.023}$	$9.586^{+0.013}_{-0.014}$	0.0880	4	1
F01-13	0.117 ± 0.002	$8.226^{+0.093}_{-0.118}$	$8.802^{+0.048}_{-0.053}$	$9.673^{+0.030}_{-0.032}$	0.1182	4	1
F01-15	0.087 ± 0.002	$8.157^{+0.073}_{-0.088}$	$8.610^{+0.058}_{-0.067}$	$9.263^{+0.035}_{-0.038}$	0.0870	4	1
F01-19	0.492 ± 0.002	$9.356^{+0.179}_{-0.311}$	$9.889^{+0.109}_{-0.145}$	$10.901^{+0.061}_{-0.071}$	0.4876	4	1
F02-0	0.087 ± 0.001	$8.253^{+0.052}_{-0.059}$	$8.886^{+0.027}_{-0.028}$	$9.754^{+0.016}_{-0.017}$
F02-4	0.295 ± 0.002	$9.272^{+0.060}_{-0.069}$	$9.914^{+0.034}_{-0.037}$	$10.747^{+0.017}_{-0.018}$
F02-6	0.145 ± 0.002	$8.424^{+0.089}_{-0.112}$	$9.115^{+0.039}_{-0.043}$	$9.989^{+0.021}_{-0.022}$	0.1367	4	1
F02-8	0.256 ± 0.003	$8.929^{+0.090}_{-0.113}$	$9.629^{+0.050}_{-0.056}$	$10.359^{+0.026}_{-0.027}$
F02-9	0.294 ± 0.001	$9.217^{+0.065}_{-0.076}$	$9.752^{+0.044}_{-0.049}$	$10.592^{+0.024}_{-0.025}$
F02-15	0.232 ± 0.001	<8.528	$9.516^{+0.062}_{-0.072}$	$10.176^{+0.031}_{-0.034}$
F02-20	0.477 ± 0.003	$9.206^{+0.165}_{-0.269}$	$9.790^{+0.106}_{-0.141}$	$10.844^{+0.058}_{-0.068}$
F02-24	0.186 ± 0.002	$8.410^{+0.109}_{-0.146}$	$9.116^{+0.083}_{-0.102}$	$9.821^{+0.042}_{-0.046}$
F03-4	0.183 ± 0.001	$8.695^{+0.065}_{-0.077}$	$9.496^{+0.032}_{-0.035}$	$10.255^{+0.018}_{-0.019}$
F03-15	0.227 ± 0.002	$8.370^{+0.131}_{-0.188}$	$8.787^{+0.134}_{-0.195}$	$9.848^{+0.072}_{-0.087}$	0.2225	4	1
F04-0	0.087 ± 0.001	$8.900^{+0.021}_{-0.022}$	$9.506^{+0.014}_{-0.015}$	$10.336^{+0.010}_{-0.010}$	0.0880	4	1
F04-3	0.169 ± 0.001	$9.042^{+0.036}_{-0.039}$	$9.589^{+0.025}_{-0.026}$	$10.411^{+0.014}_{-0.015}$	0.1672	4	1
F04-5	0.056 ± 0.001	$7.855^{+0.054}_{-0.062}$	$8.463^{+0.025}_{-0.026}$	$9.267^{+0.014}_{-0.014}$	0.050	4	3
F04-6	0.424 ± 0.002	$9.710^{+0.077}_{-0.094}$	$10.287^{+0.036}_{-0.040}$	$11.124^{+0.022}_{-0.023}$	0.4173	4	1
F04-7	0.086 ± 0.001	$8.174^{+0.063}_{-0.074}$	$8.667^{+0.038}_{-0.042}$	$9.415^{+0.023}_{-0.024}$	0.0864	4	1
F04-8	0.278 ± 0.001	$8.977^{+0.080}_{-0.099}$	$9.582^{+0.056}_{-0.064}$	$10.457^{+0.028}_{-0.030}$	0.2752	4	1
F04-13	0.193 ± 0.002	$8.664^{+0.093}_{-0.118}$	$9.375^{+0.052}_{-0.058}$	$10.099^{+0.025}_{-0.027}$	0.1871	3	1
F04-18	0.306 ± 0.002	$8.884^{+0.127}_{-0.181}$	$9.754^{+0.069}_{-0.083}$	$10.475^{+0.033}_{-0.036}$	0.3010	4	1
F04-23	0.452 ± 0.005	$9.393^{+0.158}_{-0.173}$	$10.211^{+0.075}_{-0.091}$	$10.936^{+0.041}_{-0.045}$	0.4500	4	1
F04-24	0.266 ± 0.005	$8.864^{+0.149}_{-0.228}$	$9.300^{+0.112}_{-0.151}$	$10.095^{+0.057}_{-0.066}$
F05-10	0.076 ± 0.002	$8.001^{+0.074}_{-0.089}$	$8.555^{+0.038}_{-0.042}$	$9.293^{+0.022}_{-0.023}$
F05-23	0.393 ± 0.004	$9.355^{+0.132}_{-0.191}$	$9.548^{+0.115}_{-0.157}$	$10.530^{+0.060}_{-0.070}$
F07-11	0.394 ± 0.004	$8.858^{+0.284}_{-1.110}$	$9.907^{+0.057}_{-0.085}$	$10.783^{+0.033}_{-0.039}$	0.391	4	2
F07-12	0.281 ± 0.003	$8.809^{+0.144}_{-0.216}$	$9.487^{+0.080}_{-0.098}$	$10.377^{+0.039}_{-0.043}$	0.2862	4	1
F08-1	0.088 ± 0.001	$8.884^{+0.023}_{-0.024}$	$9.413^{+0.016}_{-0.016}$	$10.253^{+0.010}_{-0.010}$	0.090	4	2
F08-5	0.143 ± 0.001	$9.126^{+0.024}_{-0.026}$	$9.752^{+0.014}_{-0.014}$	$10.507^{+0.009}_{-0.009}$	0.143	4	2
F08-11	0.248 ± 0.002	$8.882^{+0.092}_{-0.117}$	$9.481^{+0.077}_{-0.093}$	$10.199^{+0.037}_{-0.040}$	0.262	4	2
F08-14	0.420 ± 0.003	$9.423^{+0.125}_{-0.175}$	$10.112^{+0.065}_{-0.076}$	$10.923^{+0.036}_{-0.039}$	0.429	4	2
F08-17	0.200 ± 0.002	$8.571^{+0.103}_{-0.136}$	$9.252^{+0.055}_{-0.062}$	$10.077^{+0.029}_{-0.032}$	0.1991,0.200	4,4	1,2
F08-23	0.088 ± 0.002	$7.572^{+0.246}_{-0.624}$	$8.071^{+0.106}_{-0.141}$	$9.159^{+0.065}_{-0.076}$	0.0880	3	1
F09-2	0.108 ± 0.001	$9.048^{+0.021}_{-0.022}$	$9.703^{+0.013}_{-0.013}$	$10.440^{+0.008}_{-0.008}$
F10-8	0.465 ± 0.003	$9.483^{+0.139}_{-0.205}$	$9.992^{+0.076}_{-0.092}$	$11.062^{+0.041}_{-0.045}$	0.472	4	3
F10-10	0.293 ± 0.004	$8.978^{+0.131}_{-0.189}$	$9.536^{+0.068}_{-0.081}$	$10.369^{+0.037}_{-0.040}$	0.3025,0.303	4,4	1,2
F10-13	0.473 ± 0.004	$9.482^{+0.126}_{-0.179}$	$10.043^{+0.089}_{-0.112}$	$10.932^{+0.051}_{-0.058}$	0.472	4	3
F10-19	0.409 ± 0.004	$9.630^{+0.106}_{-0.140}$	$9.753^{+0.080}_{-0.097}$	$10.808^{+0.045}_{-0.050}$	0.423	4	2
F11-7	0.175 ± 0.001	$9.140^{+0.034}_{-0.037}$	$9.645^{+0.023}_{-0.024}$	$10.444^{+0.012}_{-0.013}$
F11-11	0.180 ± 0.001	$8.715^{+0.072}_{-0.086}$	$9.125^{+0.049}_{-0.055}$	$10.202^{+0.026}_{-0.028}$
F11-19	0.084 ± 0.002	$7.963^{+0.097}_{-0.126}$	$8.498^{+0.060}_{-0.069}$	$9.425^{+0.031}_{-0.034}$	0.0864	4	1
F11-23	0.081 ± 0.002	$7.734^{+0.134}_{-0.195}$	$8.357^{+0.057}_{-0.066}$	$9.315^{+0.033}_{-0.036}$
F20-3	0.090 ± 0.001	$8.851^{+0.022}_{-0.023}$	$9.443^{+0.015}_{-0.015}$	$10.273^{+0.010}_{-0.010}$	0.0875	4	1
F20-10	0.448 ± 0.003	$9.391^{+0.129}_{-0.185}$	$10.243^{+0.047}_{-0.052}$	$11.141^{+0.027}_{-0.029}$	0.4588	4	1
F21-1	0.044 ± 0.001	$7.866^{+0.036}_{-0.039}$	$8.555^{+0.016}_{-0.016}$	$9.339^{+0.010}_{-0.010}$
F21-20	0.405 ± 0.003	$9.262^{+0.113}_{-0.152}$	$9.990^{+0.111}_{-0.150}$	$10.630^{+0.068}_{-0.080}$	0.3930,0.393	3,4	1,2

Notes. The optical spectroscopic redshifts and their measurement quality flags (4 = secure; identified by more than two features, 3 = acceptable and almost good; identified by two features, according to Shim et al. 2013) are also shown if available. When there are two independent measurements, we show both results. Sources of the redshift are 1 for Shim et al. (2013), 2 for Oi et al. (2014), and 3 for our own GTC observations (see text).

Table C.3. NIR–MIR photometry in the NEP-Wide catalogue of the SPICY PAH galaxies.

ID	N2 (mJy)	N3 (mJy)	N4 (mJy)	S7 (mJy)	S9W (mJy)	S11 (mJy)	L15 (mJy)	L18W (mJy)
F00-1	0.375 ± 0.005	0.257 ± 0.004	0.225 ± 0.004	0.560 ± 0.016	1.200 ± 0.019	1.630 ± 0.028	1.360 ± 0.037	1.260 ± 0.031
F01-7	3.010 ± 0.011	1.890 ± 0.009	1.310 ± 0.007	1.850 ± 0.025	2.300 ± 0.023	2.480 ± 0.034
F01-13	0.397 ± 0.005	0.270 ± 0.004	0.198 ± 0.003	0.408 ± 0.015	0.677 ± 0.015	0.766 ± 0.022	0.634 ± 0.029	0.674 ± 0.030
F01-15	0.284 ± 0.005	0.198 ± 0.003	0.146 ± 0.003	0.486 ± 0.015	0.609 ± 0.015	0.684 ± 0.022
F01-19	0.179 ± 0.004	0.159 ± 0.003	0.115 ± 0.003	...	0.412 ± 0.014	0.756 ± 0.023	0.677 ± 0.035	0.557 ± 0.028
F02-0	0.834 ± 0.008	0.568 ± 0.006	0.401 ± 0.005	1.220 ± 0.021	1.600 ± 0.021	1.710 ± 0.030	1.500 ± 0.042	1.290 ± 0.035
F02-4	0.445 ± 0.005	0.331 ± 0.004	0.234 ± 0.003	0.355 ± 0.014	0.957 ± 0.017	1.260 ± 0.026	1.070 ± 0.036	1.030 ± 0.030
F02-6	0.638 ± 0.006	0.417 ± 0.005	0.306 ± 0.004	0.502 ± 0.016	0.927 ± 0.018	1.090 ± 0.027	1.080 ± 0.037	0.674 ± 0.027
F02-8	0.545 ± 0.006	0.413 ± 0.005	0.281 ± 0.004	0.292 ± 0.013	0.603 ± 0.015	0.935 ± 0.025	0.817 ± 0.035	0.650 ± 0.030
F02-9	0.272 ± 0.004	0.204 ± 0.004	0.160 ± 0.003	0.258 ± 0.014	0.637 ± 0.016	0.816 ± 0.022	0.671 ± 0.030	0.664 ± 0.029
F02-15	0.272 ± 0.004	0.179 ± 0.003	0.138 ± 0.003	0.226 ± 0.014	0.441 ± 0.014	0.691 ± 0.026	0.515 ± 0.029	0.356 ± 0.028
F02-20	0.222 ± 0.004	0.208 ± 0.003	0.149 ± 0.003	0.242 ± 0.013	0.462 ± 0.015	0.658 ± 0.023	0.605 ± 0.028	0.719 ± 0.026
F02-24	0.276 ± 0.005	0.186 ± 0.004	0.121 ± 0.003	0.155 ± 0.010	0.369 ± 0.014	0.428 ± 0.020	0.324 ± 0.026	0.262 ± 0.025
F03-4	0.390 ± 0.005	0.320 ± 0.004	0.222 ± 0.003	0.397 ± 0.016	0.922 ± 0.017	1.120 ± 0.025	0.961 ± 0.040	0.986 ± 0.036
F03-15	0.114 ± 0.004	0.072 ± 0.003	0.072 ± 0.003	0.145 ± 0.010	0.302 ± 0.015	0.427 ± 0.020	0.289 ± 0.029	0.251 ± 0.024
F04-0	2.340 ± 0.011	1.530 ± 0.007	1.160 ± 0.006	4.450 ± 0.033	6.040 ± 0.028	6.690 ± 0.043	6.280 ± 0.063	5.610 ± 0.052
F04-3	0.737 ± 0.006	0.487 ± 0.004	0.387 ± 0.004	0.836 ± 0.018	1.770 ± 0.019	2.210 ± 0.030	2.070 ± 0.043	1.850 ± 0.037
F04-5	0.623 ± 0.006	0.437 ± 0.005	0.298 ± 0.004	1.220 ± 0.020	1.210 ± 0.019	1.160 ± 0.025
F04-6	0.128 ± 0.003	0.138 ± 0.003	0.100 ± 0.003	0.140 ± 0.009	0.882 ± 0.017	1.280 ± 0.026	0.740 ± 0.039	0.908 ± 0.031
F04-7	0.487 ± 0.006	0.306 ± 0.004	0.206 ± 0.004	0.718 ± 0.018	0.846 ± 0.021	0.940 ± 0.032	0.844 ± 0.040	0.862 ± 0.043
F04-8	0.141 ± 0.003	0.108 ± 0.003	0.135 ± 0.004	0.238 ± 0.012	0.629 ± 0.015	0.850 ± 0.024	0.817 ± 0.030	0.906 ± 0.031
F04-13	0.565 ± 0.006	0.348 ± 0.004	0.277 ± 0.004	0.253 ± 0.013	0.801 ± 0.023	0.505 ± 0.020	0.527 ± 0.027	0.530 ± 0.034
F04-18	0.134 ± 0.004	0.106 ± 0.003	0.093 ± 0.003	0.164 ± 0.013	0.407 ± 0.014	0.568 ± 0.021	0.867 ± 0.038	0.909 ± 0.034
F04-23	0.117 ± 0.004	0.111 ± 0.003	0.081 ± 0.003	...	0.419 ± 0.014	0.773 ± 0.027	0.426 ± 0.031	0.425 ± 0.030
F04-24	0.246 ± 0.005	0.206 ± 0.004	0.165 ± 0.003	0.240 ± 0.016	0.424 ± 0.015	0.547 ± 0.021	0.773 ± 0.037	0.663 ± 0.027
F05-10	0.557 ± 0.006	0.373 ± 0.004	0.242 ± 0.004	0.681 ± 0.017	0.822 ± 0.018	0.892 ± 0.025	0.570 ± 0.028	0.477 ± 0.024
F05-23	0.132 ± 0.003	0.116 ± 0.003	0.073 ± 0.003	0.087 ± 0.011	0.325 ± 0.013	0.619 ± 0.023	0.365 ± 0.031	0.585 ± 0.041
F07-11	0.218 ± 0.004	0.171 ± 0.003	0.121 ± 0.003	0.146 ± 0.014	0.520 ± 0.015	0.944 ± 0.025	1.040 ± 0.048	0.918 ± 0.036
F07-12	0.279 ± 0.005	0.204 ± 0.003	0.145 ± 0.003	0.202 ± 0.013	0.564 ± 0.015	0.680 ± 0.022	0.784 ± 0.039	0.840 ± 0.033
F08-1	2.080 ± 0.010	1.330 ± 0.007	...	4.390 ± 0.032	5.100 ± 0.028	5.200 ± 0.038	5.110 ± 0.056	4.630 ± 0.047
F08-5	0.878 ± 0.007	0.649 ± 0.005	0.503 ± 0.005	1.590 ± 0.022	3.080 ± 0.023	3.800 ± 0.035	3.590 ± 0.049	3.170 ± 0.043
F08-11	0.342 ± 0.005	0.240 ± 0.004	0.180 ± 0.003	0.319 ± 0.014	0.852 ± 0.017	0.967 ± 0.025	1.140 ± 0.042	1.390 ± 0.034
F08-14	0.479 ± 0.006	0.413 ± 0.005	0.272 ± 0.004	0.198 ± 0.012	0.761 ± 0.016	1.320 ± 0.026	1.060 ± 0.035	1.010 ± 0.028
F08-17	0.200 ± 0.004	0.144 ± 0.003	0.129 ± 0.003	0.263 ± 0.013	0.563 ± 0.015	0.701 ± 0.022	0.735 ± 0.036	0.667 ± 0.039
F08-23	1.190 ± 0.008	0.728 ± 0.005	0.468 ± 0.004	0.540 ± 0.018	0.616 ± 0.017	0.682 ± 0.025	0.475 ± 0.039	0.389 ± 0.032
F09-2	1.540 ± 0.009	1.050 ± 0.007	0.832 ± 0.005	2.710 ± 0.025	4.500 ± 0.025	5.250 ± 0.039	5.180 ± 0.057	4.760 ± 0.048
F10-8	0.215 ± 0.004	0.191 ± 0.003	0.129 ± 0.003	0.158 ± 0.013	0.664 ± 0.018	1.230 ± 0.028	1.090 ± 0.037	0.915 ± 0.030
F10-10	0.161 ± 0.004	0.130 ± 0.003	0.097 ± 0.003	0.143 ± 0.010	0.459 ± 0.015	0.598 ± 0.022	0.519 ± 0.026	0.486 ± 0.023
F10-13	0.154 ± 0.004	0.142 ± 0.003	0.105 ± 0.003	0.121 ± 0.011	0.472 ± 0.015	0.888 ± 0.027	0.694 ± 0.042	0.990 ± 0.043
F10-19	0.095 ± 0.003	0.085 ± 0.003	0.064 ± 0.002	0.070 ± 0.008	0.366 ± 0.015	0.585 ± 0.021	0.330 ± 0.030	0.498 ± 0.032
F11-7	0.513 ± 0.006	0.331 ± 0.004	0.268 ± 0.004	0.740 ± 0.016	1.660 ± 0.020	2.100 ± 0.029	2.040 ± 0.043	1.760 ± 0.035
F11-11	0.232 ± 0.004	0.159 ± 0.003	0.139 ± 0.003	0.484 ± 0.017	0.926 ± 0.017	1.180 ± 0.025	1.030 ± 0.038	1.170 ± 0.035
F11-19	0.800 ± 0.007	0.521 ± 0.005	0.336 ± 0.004	0.635 ± 0.017	0.799 ± 0.018	0.798 ± 0.024	0.745 ± 0.036	0.541 ± 0.025
F11-23	0.376 ± 0.005	0.255 ± 0.004	0.176 ± 0.003	0.469 ± 0.015	0.525 ± 0.015	0.536 ± 0.021	0.504 ± 0.027	0.509 ± 0.027
F20-3	1.010 ± 0.007	0.823 ± 0.006	0.640 ± 0.005	3.730 ± 0.031	4.670 ± 0.026	4.690 ± 0.039
F20-10	0.179 ± 0.004	0.154 ± 0.003	0.110 ± 0.003	0.080 ± 0.008	0.569 ± 0.015	0.963 ± 0.024	0.609 ± 0.032	1.030 ± 0.030
F21-1	0.660 ± 0.006	0.463 ± 0.005	0.324 ± 0.004	2.120 ± 0.023	2.110 ± 0.021	2.100 ± 0.029	2.750 ± 0.048	2.780 ± 0.043
F21-20	0.125 ± 0.003	0.113 ± 0.003	0.077 ± 0.002	...	0.266 ± 0.012	0.466 ± 0.020	0.388 ± 0.033	0.257 ± 0.024

Table C.4. Optical photometry and source extraction flag in the CFHT optical NEP catalogue of the SPICY PAH galaxies.

ID	u^* (mJy)	g' (mJy)	r' (mJy)	i' (mJy)	z' (mJy)	Flag
F00-1	...	0.0541 ± 0.0001	0.1138 ± 0.0001	0.1629 ± 0.0003	0.1986 ± 0.0007	0
F01-7	...	0.5749 ± 0.0000	1.2348 ± 0.0000	1.6520 ± 0.0000	1.9898 ± 0.0018	2
F01-13	...	0.0908 ± 0.0001	0.1716 ± 0.0002	0.2359 ± 0.0004	0.2965 ± 0.0008	0
F01-15	...	0.1310 ± 0.0001	0.1932 ± 0.0002	0.2417 ± 0.0002	0.2729 ± 0.0008	0
F01-19	...	0.0119 ± 0.0001	0.0365 ± 0.0001	0.0541 ± 0.0002	0.0751 ± 0.0006	0
F02-0	0.1306 ± 0.0002	0.3128 ± 0.0003	0.4948 ± 0.0005	0.6020 ± 0.0006	0.7171 ± 0.0013	2
F02-4	0.0068 ± 0.0001	0.0221 ± 0.0001	0.0677 ± 0.0001	0.1022 ± 0.0003	0.1444 ± 0.0005	0
F02-6	0.0645 ± 0.0002	0.1796 ± 0.0002	0.3148 ± 0.0003	0.3945 ± 0.0004	0.5119 ± 0.0009	0
F02-8	0.0147 ± 0.0001	0.0412 ± 0.0001	0.1002 ± 0.0002	0.1437 ± 0.0004	0.2040 ± 0.0006	0
F02-9	0.0116 ± 0.0001	0.0260 ± 0.0001	0.0660 ± 0.0002	0.0944 ± 0.0003	0.1378 ± 0.0006	2
F02-15	0.0196 ± 0.0001	0.0478 ± 0.0001	0.1045 ± 0.0002	0.1474 ± 0.0003	0.1772 ± 0.0007	0
F02-20	0.0031 ± 0.0001	0.0049 ± 0.0001	0.0164 ± 0.0001	0.0236 ± 0.0002	0.0705 ± 0.0004	3
F02-24	0.0076 ± 0.0001	0.0270 ± 0.0001	0.0694 ± 0.0001	0.0988 ± 0.0003	0.1008 ± 0.0005	0
F03-4	...	0.0735 ± 0.0001	0.1164 ± 0.0001	0.1455 ± 0.0003	0.1560 ± 0.0007	2
F03-15	...	0.0102 ± 0.0001	0.0254 ± 0.0001	0.0395 ± 0.0002	0.0440 ± 0.0004	0
F04-0	...	0.5618 ± 0.0000	1.0224 ± 0.0000	1.3957 ± 0.0000	1.5981 ± 0.0015	0
F04-3	...	0.0697 ± 0.0001	0.1646 ± 0.0002	0.2468 ± 0.0002	0.3045 ± 0.0008	2
F04-5	0.4626 ± 0.0004	0.5577 ± 0.0005	...	0
F04-6	0.0147 ± 0.0001	0.0234 ± 0.0002	...	0
F04-7	...	0.2694 ± 0.0002	0.3908 ± 0.0004	0.5077 ± 0.0005	0.5526 ± 0.0015	0
F04-8	0.0264 ± 0.0001	0.0425 ± 0.0002	...	0
F04-13	0.1768 ± 0.0002	0.2521 ± 0.0002	...	0
F04-18	0.0387 ± 0.0001	0.0521 ± 0.0001	...	0
F04-23	...	0.0095 ± 0.0001	0.0196 ± 0.0001	0.0256 ± 0.0002	0.0306 ± 0.0005	0
F04-24 ^a
F05-10	0.0990 ± 0.0003	0.2359 ± 0.0002	0.3898 ± 0.0004	0.4699 ± 0.0004	0.5649 ± 0.0010	0
F05-23	0.0042 ± 0.0001	0.0086 ± 0.0001	0.0232 ± 0.0002	0.0396 ± 0.0003	0.0435 ± 0.0005	0
F07-11	...	0.0183 ± 0.0001	0.0520 ± 0.0001	0.0707 ± 0.0002	0.0898 ± 0.0005	0
F07-12	...	0.0309 ± 0.0001	0.0771 ± 0.0001	0.1097 ± 0.0002	0.1338 ± 0.0006	0
F08-1 ^b
F08-5	...	0.1572 ± 0.0001	0.3045 ± 0.0003	0.4321 ± 0.0004	0.5143 ± 0.0009	2
F08-11	...	0.0217 ± 0.0001	0.0656 ± 0.0001	0.1070 ± 0.0003	0.1392 ± 0.0006	0
F08-14	...	0.0283 ± 0.0001	0.0792 ± 0.0001	0.1161 ± 0.0003	0.1444 ± 0.0008	2
F08-17	...	0.1020 ± 0.0001	0.1008 ± 0.0002	0.1435 ± 0.0003	0.1274 ± 0.0007	0
F08-23	...	0.2399 ± 0.0002	0.5181 ± 0.0005	0.7053 ± 0.0006	0.8904 ± 0.0008	0
F09-2	...	0.3688 ± 0.0000	0.5932 ± 0.0000	1.1663 ± 0.0000	1.0028 ± 0.0009	0
F10-8	...	0.0083 ± 0.0001	0.0274 ± 0.0001	0.0400 ± 0.0002	0.0583 ± 0.0006	0
F10-10	...	0.0075 ± 0.0001	0.0227 ± 0.0001	0.0337 ± 0.0002	0.0468 ± 0.0005	0
F10-13	...	0.0043 ± 0.0001	0.0101 ± 0.0001	0.0142 ± 0.0002	0.0143 ± 0.0005	3
F10-19	...	0.0041 ± 0.0001	0.0127 ± 0.0001	0.0218 ± 0.0002	0.0210 ± 0.0006	0
F11-7	...	0.0707 ± 0.0001	0.1521 ± 0.0001	0.2180 ± 0.0002	0.2635 ± 0.0007	0
F11-11	...	0.0633 ± 0.0001	0.1073 ± 0.0001	0.1426 ± 0.0003	0.1586 ± 0.0006	0
F11-19	...	0.1337 ± 0.0001	0.3020 ± 0.0003	0.4274 ± 0.0004	0.5521 ± 0.0010	0
F11-23	...	0.0682 ± 0.0001	0.1460 ± 0.0001	0.2055 ± 0.0002	0.2604 ± 0.0007	0
F20-3	...	0.1723 ± 0.0002	0.3287 ± 0.0003	0.4639 ± 0.0004	0.5749 ± 0.0011	0
F20-10	...	0.0130 ± 0.0001	0.0347 ± 0.0001	0.0492 ± 0.0002	0.0760 ± 0.0006	0
F21-1	...	0.1057 ± 0.0001	0.2423 ± 0.0002	0.3330 ± 0.0003	0.4305 ± 0.0004	0
F21-20	...	0.0049 ± 0.0001	0.0168 ± 0.0001	0.0272 ± 0.0002	0.0354 ± 0.0006	0

Notes. The flags are 0 for clear detection, 1 for having neighbours, 2 for being blended, and 3 for both 1 and 2 (see [Hwang et al. 2007](#) for more).

^(a)This source is damaged due to a nearby bright and saturated star on the CFHT image, and is not catalogued. ^(b)This source falls on one of CCD gaps on the CFHT image, and is not catalogued.

Table C.5. Similar table as Table C.1, but for the bright AGN candidates.

SPICY ID	NEP-Wide catalogue			SPICY <i>S9W</i> flux (mJy)	CFHT NEP catalogue		Class
	ID	RA J2000 (hms)	Dec J2000 (dms)		ID	FIELD	
F00-3	65028336	17 54 54.05	+66 34 18.0	1.23 ± 0.04	37688	2	TYPE1
F04-20	65041740	17 57 32.54	+66 40 28.5	0.43 ± 0.02	46530	2	...
F05-1	65055361	18 00 11.66	+66 52 15.0	4.25 ± 0.13	55298	1	TYPE1
F05-13	65055061	18 00 08.16	+66 55 01.1	0.62 ± 0.02	58237	1	...
F10-20	65040243	17 57 14.66	+66 31 13.2	0.34 ± 0.02	32913	2	TYPE1
F11-14	65037307	17 56 41.06	+66 05 25.7	0.83 ± 0.03	1859	2	TYPE1

Notes. Optical spectroscopic classification results by Shim et al. (2013), if available, are shown in the “class” column. TYPE1 indicates type-1 AGN.

Table C.6. Similar table as Table C.3, but for the bright AGN candidates.

ID	<i>N2</i> (mJy)	<i>N3</i> (mJy)	<i>N4</i> (mJy)	<i>S7</i> (mJy)	<i>S9W</i> (mJy)	<i>S11</i> (mJy)	<i>L15</i> (mJy)	<i>L18W</i> (mJy)
F00-3	0.125 ± 0.004	0.185 ± 0.003	0.282 ± 0.004	0.931 ± 0.017	1.210 ± 0.018	1.630 ± 0.027	2.480 ± 0.045	2.760 ± 0.040
F04-20	0.074 ± 0.003	0.138 ± 0.003	0.149 ± 0.003	0.385 ± 0.014	0.520 ± 0.015	0.590 ± 0.021	0.707 ± 0.030	0.825 ± 0.029
F05-1	0.425 ± 0.005	0.561 ± 0.005	0.944 ± 0.005	3.030 ± 0.028	4.390 ± 0.024	5.960 ± 0.038	11.500 ± 0.074	14.400 ± 0.066
F05-13	0.065 ± 0.004	0.116 ± 0.003	0.177 ± 0.003	0.461 ± 0.015	0.612 ± 0.016	0.766 ± 0.026	0.865 ± 0.032	0.850 ± 0.029
F10-20	0.149 ± 0.004	0.226 ± 0.004	0.254 ± 0.004	0.301 ± 0.013	0.346 ± 0.013	0.390 ± 0.021	0.606 ± 0.039	0.701 ± 0.033
F11-14	0.150 ± 0.004	0.210 ± 0.003	0.334 ± 0.004	0.712 ± 0.017	0.983 ± 0.017	1.170 ± 0.025	1.830 ± 0.042	2.070 ± 0.040

Table C.7. Similar table as Table C.4, but for the bright AGN candidates.

ID	<i>u</i> [*] (mJy)	<i>g</i> ['] (mJy)	<i>r</i> ['] (mJy)	<i>i</i> ['] (mJy)	<i>z</i> ['] (mJy)	Flag
F00-3	...	0.0595 ± 0.0001	0.1303 ± 0.0001	0.0650 ± 0.0001	0.1361 ± 0.0004	0
F04-20	0.0054 ± 0.0001	0.0128 ± 0.0001	...	0
F05-1	0.0105 ± 0.0001	0.0274 ± 0.0001	0.1075 ± 0.0001	0.1694 ± 0.0002	0.1982 ± 0.0004	0
F05-13	0.0002 ± 0.0001	0.0005 ± 0.0000	0.0010 ± 0.0001	0.0020 ± 0.0001	0.0057 ± 0.0002	0
F10-20	...	0.0056 ± 0.0001	0.0198 ± 0.0001	0.0302 ± 0.0002	0.0391 ± 0.0005	0
F11-14	...	0.0493 ± 0.0000	0.0712 ± 0.0001	0.0935 ± 0.0002	0.1079 ± 0.0004	0

Table C.8. Monochromatic photometric luminosities and rest-frame flux ratios of the SPICY PAH galaxies.

ID	$\log \nu L_{\nu \text{phot}} (3.5 \mu\text{m})$	$\log \nu L_{\nu \text{phot}} (7.7 \mu\text{m})$	Rest-frame flux ratios		
	(L_{\odot})	(L_{\odot})	$F_{\text{rest } 3.5 \mu\text{m}}/F_{\text{rest } 2.0 \mu\text{m}}$	$F_{\text{rest } 7.7 \mu\text{m}}/F_{\text{rest } 3.5 \mu\text{m}}$	$F_{\text{rest } 11.3 \mu\text{m}}/F_{\text{rest } 7.7 \mu\text{m}}$
F00-1	$9.770^{+0.010}_{-0.010}$	$10.234^{+0.009}_{-0.009}$	0.611 ± 0.018	6.398 ± 0.203	1.035 ± 0.041
F01-7	$9.571^{+0.003}_{-0.003}$	$9.373^{+0.008}_{-0.008}$	0.454 ± 0.004	1.394 ± 0.027	...
F01-13	$9.188^{+0.010}_{-0.010}$	$9.334^{+0.016}_{-0.017}$	0.521 ± 0.015	3.082 ± 0.139	1.038 ± 0.063
F01-15	$8.808^{+0.012}_{-0.012}$	$9.015^{+0.018}_{-0.019}$	0.537 ± 0.018	3.545 ± 0.178	...
F01-19	$10.112^{+0.019}_{-0.020}$	$10.662^{+0.017}_{-0.018}$	0.578 ± 0.032	7.810 ± 0.475	0.838 ± 0.072
F02-0	$9.253^{+0.007}_{-0.007}$	$9.430^{+0.010}_{-0.010}$	0.509 ± 0.010	3.307 ± 0.091	1.055 ± 0.036
F02-4	$10.031^{+0.010}_{-0.011}$	$10.406^{+0.011}_{-0.012}$	0.559 ± 0.016	5.220 ± 0.188	0.931 ± 0.048
F02-6	$9.555^{+0.009}_{-0.009}$	$9.672^{+0.009}_{-0.010}$	0.499 ± 0.012	2.882 ± 0.085	1.147 ± 0.051
F02-8	$10.004^{+0.009}_{-0.009}$	$10.103^{+0.014}_{-0.015}$	0.555 ± 0.014	2.766 ± 0.110	1.074 ± 0.067
F02-9	$9.856^{+0.014}_{-0.015}$	$10.216^{+0.016}_{-0.016}$	0.616 ± 0.025	5.031 ± 0.248	0.902 ± 0.062
F02-15	$9.590^{+0.015}_{-0.015}$	$9.862^{+0.019}_{-0.020}$	0.529 ± 0.022	4.122 ± 0.233	1.012 ± 0.088
F02-20	$10.199^{+0.016}_{-0.016}$	$10.578^{+0.018}_{-0.019}$	0.581 ± 0.026	5.263 ± 0.295	1.005 ± 0.071
F02-24	$9.373^{+0.017}_{-0.017}$	$9.505^{+0.021}_{-0.022}$	0.477 ± 0.022	2.984 ± 0.189	0.933 ± 0.095
F03-4	$9.628^{+0.010}_{-0.010}$	$9.896^{+0.010}_{-0.010}$	0.618 ± 0.018	4.077 ± 0.136	1.044 ± 0.051
F03-15	$9.265^{+0.027}_{-0.028}$	$9.649^{+0.026}_{-0.028}$	0.630 ± 0.048	5.319 ± 0.474	0.909 ± 0.112
F04-0	$9.703^{+0.003}_{-0.003}$	$10.007^{+0.004}_{-0.004}$	0.504 ± 0.004	4.426 ± 0.051	1.129 ± 0.015
F04-3	$9.772^{+0.006}_{-0.007}$	$10.101^{+0.006}_{-0.006}$	0.537 ± 0.010	4.694 ± 0.095	1.142 ± 0.031
F04-5	$8.749^{+0.008}_{-0.008}$	$8.930^{+0.011}_{-0.011}$	0.518 ± 0.011	3.339 ± 0.103	...
F04-6	$9.940^{+0.020}_{-0.021}$	$10.741^{+0.011}_{-0.011}$	0.642 ± 0.038	13.897 ± 0.747	0.643 ± 0.041
F04-7	$8.966^{+0.010}_{-0.010}$	$9.153^{+0.016}_{-0.017}$	0.448 ± 0.012	3.384 ± 0.151	1.091 ± 0.068
F04-8	$9.714^{+0.016}_{-0.017}$	$10.170^{+0.015}_{-0.016}$	0.942 ± 0.048	6.287 ± 0.326	1.063 ± 0.066
F04-13	$9.730^{+0.009}_{-0.009}$	$9.789^{+0.018}_{-0.019}$	0.497 ± 0.012	2.522 ± 0.119	0.756 ± 0.057
F04-18	$9.654^{+0.019}_{-0.020}$	$10.092^{+0.021}_{-0.022}$	0.715 ± 0.042	6.030 ± 0.406	1.540 ± 0.114
F04-23	$9.901^{+0.025}_{-0.026}$	$10.564^{+0.019}_{-0.020}$	0.612 ± 0.044	10.119 ± 0.741	0.609 ± 0.062
F04-24	$9.800^{+0.014}_{-0.014}$	$9.941^{+0.022}_{-0.023}$	0.698 ± 0.029	3.044 ± 0.184	1.438 ± 0.113
F05-10	$8.931^{+0.009}_{-0.009}$	$9.017^{+0.013}_{-0.016}$	0.475 ± 0.011	2.681 ± 0.109	0.952 ± 0.054
F05-23	$9.724^{+0.027}_{-0.028}$	$10.371^{+0.018}_{-0.018}$	0.500 ± 0.037	9.751 ± 0.738	0.629 ± 0.062
F07-11	$9.961^{+0.017}_{-0.018}$	$10.572^{+0.013}_{-0.013}$	0.556 ± 0.028	8.984 ± 0.454	1.086 ± 0.062
F07-12	$9.782^{+0.013}_{-0.014}$	$10.099^{+0.018}_{-0.019}$	0.553 ± 0.021	4.568 ± 0.240	1.187 ± 0.087
F08-1	...	$9.956^{+0.004}_{-0.004}$	1.034 ± 0.015
F08-5	$9.754^{+0.006}_{-0.006}$	$10.182^{+0.004}_{-0.004}$	0.597 ± 0.010	5.884 ± 0.092	1.169 ± 0.020
F08-11	$9.766^{+0.012}_{-0.012}$	$10.140^{+0.013}_{-0.013}$	0.554 ± 0.019	5.199 ± 0.214	1.195 ± 0.064
F08-14	$10.349^{+0.011}_{-0.012}$	$10.764^{+0.010}_{-0.010}$	0.516 ± 0.016	5.717 ± 0.203	0.816 ± 0.036
F08-17	$9.430^{+0.016}_{-0.016}$	$9.770^{+0.015}_{-0.016}$	0.651 ± 0.030	4.809 ± 0.245	1.186 ± 0.078
F08-23	$9.350^{+0.005}_{-0.005}$	$9.039^{+0.020}_{-0.021}$	0.422 ± 0.006	1.074 ± 0.052	0.973 ± 0.076
F09-2	$9.738^{+0.004}_{-0.004}$	$10.081^{+0.004}_{-0.004}$	0.550 ± 0.006	4.852 ± 0.065	1.187 ± 0.017
F10-8	$10.103^{+0.019}_{-0.019}$	$10.825^{+0.012}_{-0.012}$	0.526 ± 0.027	11.577 ± 0.602	0.851 ± 0.045
F10-10	$9.648^{+0.019}_{-0.020}$	$10.075^{+0.020}_{-0.021}$	0.633 ± 0.036	5.881 ± 0.387	0.949 ± 0.081
F10-13	$10.049^{+0.021}_{-0.022}$	$10.678^{+0.017}_{-0.018}$	0.609 ± 0.037	9.554 ± 0.599	0.948 ± 0.076
F10-19	$9.726^{+0.025}_{-0.027}$	$10.372^{+0.018}_{-0.019}$	0.640 ± 0.049	9.742 ± 0.718	0.628 ± 0.066
F11-7	$9.640^{+0.009}_{-0.009}$	$10.113^{+0.006}_{-0.006}$	0.530 ± 0.013	6.531 ± 0.162	1.170 ± 0.032
F11-11	$9.375^{+0.014}_{-0.014}$	$9.889^{+0.010}_{-0.010}$	0.601 ± 0.024	7.180 ± 0.283	1.096 ± 0.050
F11-19	$9.160^{+0.007}_{-0.007}$	$9.095^{+0.015}_{-0.016}$	0.457 ± 0.008	1.893 ± 0.074	1.009 ± 0.058
F11-23	$8.834^{+0.010}_{-0.011}$	$8.887^{+0.020}_{-0.021}$	0.499 ± 0.014	2.481 ± 0.132	1.017 ± 0.074
F20-3	$9.462^{+0.005}_{-0.005}$	$9.925^{+0.005}_{-0.005}$	0.670 ± 0.009	6.387 ± 0.097	...
F20-10	$10.004^{+0.019}_{-0.020}$	$10.647^{+0.013}_{-0.013}$	0.575 ± 0.031	9.668 ± 0.525	0.774 ± 0.049
F21-1	$8.578^{+0.007}_{-0.007}$	$8.964^{+0.007}_{-0.007}$	0.525 ± 0.010	5.352 ± 0.119	1.078 ± 0.026
F21-20	$9.782^{+0.024}_{-0.025}$	$10.281^{+0.021}_{-0.022}$	0.561 ± 0.038	6.948 ± 0.522	0.808 ± 0.088